**DOT/FAA/AR-11/17**

Air Traffic Organization
NextGen & Operations Planning
Office of Research and
Technology Development
Washington, DC 20591

# Propeller Damage Tolerance and Nondestructive Inspection Study

December 2011

Final Report

This document is available to the U.S. public through the National Technical Information Services (NTIS), Springfield, Virginia 22161.

This document is also available from the Federal Aviation Administration William J. Hughes Technical Center at actlibrary.tc.faa.gov.

U.S. Department of Transportation
**Federal Aviation Administration**

## NOTICE

This document is disseminated under the sponsorship of the U.S. Department of Transportation in the interest of information exchange. The United States Government assumes no liability for the contents or use thereof. The United States Government does not endorse products or manufacturers. Trade or manufacturer's names appear herein solely because they are considered essential to the objective of this report. The findings and conclusions in this report are those of the author(s) and do not necessarily represent the views of the funding agency. This document does not constitute FAA policy. Consult the FAA sponsoring organization listed on the Technical Documentation page as to its use.

This report is available at the Federal Aviation Administration William J. Hughes Technical Center's Full-Text Technical Reports page: actlibrary.tc.faa.gov in Adobe Acrobat portable document format (PDF).

**Technical Report Documentation Page**

| 1. Report No. | 2. Government Accession No. | 3. Recipient's Catalog No. |
|---|---|---|
| DOT/FAA/AR-11/17 | | |

| 4. Title and Subtitle | 5. Report Date |
|---|---|
| PROPELLER DAMAGE TOLERANCE AND NONDESTRUCTIVE INSPECTION STUDY | December 2011 |
| | 6. Performing Organization Code |
| 7. Author(s) | 8. Performing Organization Report No. |
| Stephen L. Smith[1], Dave P. Nagle[1], Matthew C. Soule[1], Nadia Slivka[1], and Dennis P. Roach[2] | |
| 9. Performing Organization Name and Address | 10. Work Unit No. (TRAIS) |
| Hamilton Sundstrand[1]<br>1 Hamilton Road<br>Windsor Locks, CT 06096<br><br>Sandia National Laboratories[2]<br>Box 5800 MS-0615<br>Albuquerque, NM 87175 | |
| | 11. Contract or Grant No. |
| 12. Sponsoring Agency Name and Address | 13. Type of Report and Period Covered |
| U.S. Department of Transportation<br>Federal Aviation Administration<br>Air Traffic Organization NextGen & Operations Planning<br>Office of Research and Technology Development<br>Washington, DC 20591 | Final Report |
| | 14. Sponsoring Agency Code<br>ANE-110 |

15. Supplementary Notes

The Federal Aviation Administration Airport and Aircraft Safety R&D Group COTR was Cu Nguyen.

16. Abstract

This report describes the results of the propeller damage tolerance study in which Hamilton Sundstrand assessed the impact on propeller weight by using a threshold damage tolerance approach, in addition to meeting current safe-life criteria, as the basis for propeller structural design. Damage threshold behavior was developed by surface crack tension fatigue testing of D6AC steel specimens with laser-generated, crack-like features. The knowledge acquired from this testing was used to develop modified Goodman diagrams of peened and unpeened D6AC steel with a 0.015-inch-radius surface flaw. The geometry of the Hamilton Sundstrand Standard Model 568F propeller hub and blade was modified as required to maintain the stress levels below the newly established Goodman curves for precluding high-cycle fatigue crack propagation from a 0.015-inch surface crack. The weight increase resulting from these modifications was calculated. Complementary studies in nondestructive inspection (NDI) developed NDI techniques to reliably detect cracks and corrosion that could occur based on the propeller load spectrum and operating environment.

| 17. Key Words | 18. Distribution Statement |
|---|---|
| Damage tolerance, Crack growth damage tolerance, Fatigue, Fatigue crack growth, Finite element analysis, Laser-generated crack-like features | This document is available to the U.S. public through the National Technical Information Service (NTIS), Springfield, Virginia 22161. This document is also available from the Federal Aviation Administration William J. Hughes Technical Center at actlibrary.tc.faa.gov. |

| 19. Security Classif. (of this report) | 20. Security Classif. (of this page) | 21. No. of Pages | 22. Price |
|---|---|---|---|
| Unclassified | Unclassified | 74 | |

**Form DOT F 1700.7** (8-72) Reproduction of completed page authorized

ACKNOWLEDGEMENTS

The authors would like to acknowledge Royce Forman of the National Aeronautics and Space Administration Johnson Space Center and John Bakuckas of the Federal Aviation Administration William J. Hughes Technical Center for their assistance in fatigue testing.

TABLE OF CONTENTS


| | | | Page |
|---|---|---|---|
| EXECUTIVE SUMMARY | | | xv |
| 1. | INTRODUCTION | | 1 |
| 2. | APPROACH | | 1 |
| 3. | DISCUSSION | | 3 |
| | 3.1 | D6AC Fatigue Testing and DT Allowables | 3 |
| | | 3.1.1 Specimen Preparation and Testing | 3 |
| | | 3.1.2 Test Results and Discussion | 6 |
| | 3.2 | The HS Model 568F Blade Modification Based on CGDT Allowables | 14 |
| | 3.3 | The HS Model 568F Hub Modification Based on CGDT Allowables | 22 |
| | 3.4 | Fracture Mechanics Analysis of HS Model 568F Tulip Spectrum Loading | 27 |
| 4. | INSPECTION OF MICROSURFACE DEFECTS | | 31 |
| | 4.1 | Nondestructive Inspection Overview | 31 |
| | 4.2 | Propeller DT Analysis and NDI Evaluation | 32 |
| | | 4.2.1 Program Goals and Tasks | 32 |
| | | 4.2.2 Overall FAA Propeller DT Road Map | 33 |
| | | 4.2.3 Survey of Causes and Damage Leading to Cracks in Propeller Blades and Hubs | 34 |
| | 4.3 | Description of NDI Activity and Methods | 35 |
| | | 4.3.1 Ultrasonic NDI Method | 40 |
| | | 4.3.2 Ultrasonic Pitch-Catch Pulse-Echo Inspections | 40 |
| | | 4.3.3 A-Scan Mode | 41 |
| | | 4.3.4 C-Scan Mode | 41 |
| | | 4.3.5 Eddy-Current NDI Method | 42 |
| | 4.4 | Results of NDI for Crack and Corrosion Detection | 43 |
| | | 4.4.1 Phased Array UT Inspection Method | 44 |
| | | 4.4.2 Dogbone Semicircular Laser Notch/Crack Specimens for Fatigue Property Assessment and NDI Evaluation | 45 |

4.4.3 Detection of Corrosion Pits Using Phased Array UT 52

4.4.4 Small Crack Detection Using EC 54

4.5 Conclusions From NDI Study 56

5. SUMMARY 56

6. CONCLUSIONS AND RECOMMENDATIONS 57

7. REFERENCES 58

APPENDIX A—MATERIAL PROPERTIES USED FOR FRACTURE MECHANICS ANALYSIS

LIST OF FIGURES


| Figure | | Page |
|---|---|---|
| 1 | Cross-Section of the HS Model 568F Tulip Modifications (Modification 1) | 2 |
| 2 | Cross-Section of the HS Model 568F Hub Geometry Modifications | 2 |
| 3 | Surface Crack Tension Specimen Before Laser Notching (12X-1956) | 3 |
| 4 | Shot-Peening Residual Stress Measurements for 12X-1956 Specimens | 4 |
| 5 | Microphotograph of Semicircular D6AC LGCLF, Etched With Nital | 5 |
| 6 | Crack Initiation Data D6AC 0.015″ by 0.030″ LGCLF, $R$ = 0.1 | 6 |
| 7 | Crack Initiation Data D6AC 0.015″ by 0.030″ LGCLF, $R$ = 0.7 | 7 |
| 8 | Effect of LGCLF on Unpeened D6AC 35 HRC Kitigawa-El Haddad Diagram | 7 |
| 9 | Effect of LGCLF on Peened D6AC 35 HRC Kitigawa-El Haddad Diagram | 8 |
| 10 | Modified Goodman Diagram for 0.015-Inch-Radius LGCLF for Peened D6AC | 9 |
| 11 | Modified Goodman Diagram for 0.015-Inch-Radius LGCLF for Unpeened D6AC | 9 |
| 12 | D6AC Unpeened $R$ = 0.1, LGCLF and Pits Generated in HS Laboratory | 10 |
| 13 | D6AC Peened $R$ = 0.1, LGCLF and Pits Generated in HS Laboratory | 11 |
| 14 | The *da/dN* Plot for D6AC-2 Using the SCT Specimen | 12 |
| 15 | Threshold Plot of D6AC | 13 |
| 16 | Near Threshold Data Curve for D6AC Steel | 14 |
| 17 | Original HS Model 568F Blade FEM—Full Blade | 14 |
| 18 | Original HS Model 568F Blade FEM—Tulip Area | 15 |
| 19 | New HS Model 568F Blade FEM—Body of Revolution | 15 |
| 20 | New HS Model 568F Blade FEM—Section A-A | 15 |
| 21 | New HS Model 568F Blade FEM—Section A-A Enlarged | 16 |
| 22 | The HS Model 568F Blade FEM | 16 |
| 23 | Spanwise Cut Through the FEM | 17 |

| | | |
|---|---|---|
| 24 | Finite Element Model—Tulip Elements | 17 |
| 25 | Spanwise Cut Through the Tulip | 17 |
| 26 | Normalized Steady Principal Stresses in Baseline HS Model 568F Tulip | 18 |
| 27 | Normalized Cyclic Principal Stresses in Baseline HS Model 568F Tulip | 18 |
| 28 | Goodman Diagram for HS Model 568F Tulip—Peened | 19 |
| 29 | Principal Stress Margins in Baseline HS Model 568F Tulip—Peened | 19 |
| 30 | Principal Stress Margins in Baseline HS Model 568F Tulip—Unpeened | 20 |
| 31 | The HS Model 568F Tulip Modification 2 | 20 |
| 32 | The HS Model 568F Tulip Modification 3 | 21 |
| 33 | The HS Model 568F Tulip Modification 1—Overstress Area | 21 |
| 34 | Goodman Diagram for the HS Model 568F Tulip Modification 1 | 22 |
| 35 | Cut-Away View of the HS Model 568F Hub Geometry | 23 |
| 36 | The FEM Construction of the HS Model 568F Hub | 23 |
| 37 | Cut-Away View of the HS Model 568F Hub FEM Construction | 24 |
| 38 | The HS Model 568F Hub FEM Results—Goodman Diagram for Nominal Case | 25 |
| 39 | Baseline HS Model 568F Hub FEM Results—Dome Bolt Hole | 25 |
| 40 | Baseline HS Model 568F Hub FEM Results—Between Arms | 26 |
| 41 | Baseline HS Model 568F Hub FEM Results—Ball-Loading Hole | 26 |
| 42 | Baseline HS Model 568F Hub FEM Results—Moment Axis Aft Fillet | 26 |
| 43 | Goodman Diagram for HS Model 568F Modified Hub FEM Results | 27 |
| 44 | Modified Goodman Diagram for 0.015-Inch-Radius LGCLF for Peened D6AC | 28 |
| 45 | Normalized Stress Distribution Through the Thickness for Applied Loads | 29 |
| 46 | Stress Distribution Through the Thickness for Residual Stress From Peening | 29 |
| 47 | Screen Shot of the Fracture Mechanics Model | 30 |
| 48 | Verification of Fracture Model With the Constant-Amplitude Load Tests | 30 |

| | | |
|---|---|---|
| 49 | Crack Size vs Years for HS Model 568F Tulip Spectrum Loading | 31 |
| 50 | The HS Model 568F Propeller With Six Composite Blades | 33 |
| 51 | Leading Proximate Causes of Crack Formation in Propellers | 35 |
| 52 | The HS Model 568F Propeller Redesign Process Using Fatigue Specimens to Produce Fracture Properties of D6AC Propeller Material | 36 |
| 53 | Photographs of the Laser Notch Used to Simulate Crack Notches in Metals and Subsequent Crack Growth Emanating From Initial Laser Notch | 37 |
| 54 | Elliptical Crack Growth in Fatigue Specimen With Laser Notch | 37 |
| 55 | Generation of NDI Test Specimens Using a Laser Notch Process Followed by Carefully Controlled Surface Machining | 38 |
| 56 | Aluminum Test Specimens (3.5″ wide by 6″ high by 0.125″ thick) Produced Using Machining Process That Removes Surface Indications of Burrowing Crack | 38 |
| 57 | Generation of NDI Test Specimens Using a Laser Notch to Help Initiate a Fatigue Crack Followed by Carefully Controlled Surface Machining | 39 |
| 58 | Pulse-Echo UT Inspection and Reflection of UT Waves at Various Interfaces | 41 |
| 59 | Induction of ECs in Conductive Materials | 42 |
| 60 | Impedance Plane Display Showing Signal Traces for Surface Cracks of Different Depths | 43 |
| 61 | Wave Travel Through the Inspected Part | 43 |
| 62 | OmniScan UT Inspection Unit and Propeller Crack Test Specimens | 44 |
| 63 | Sample Signal From Phased Array UT Inspection | 44 |
| 64 | Sample UT Detection of a 0.033″ Length Crack | 45 |
| 65 | Dogbone Specimen With Center Crack, PD Leads and UT Array Probe, and Sectoral Scan From UT Phased Array Inspection Showing Crack Detection | 45 |
| 66 | Comparison of Flawed and Unflawed Signals From Phase Array UT Inspection Method | 46 |
| 67 | Sample Phase Array UT Indications Demonstrating Crack Length Estimation Using Sectoral Views | 46 |
| 68 | Crack Detection Summary for Sample Panel | 47 |

| | | |
|---|---|---|
| 69 | Crack Locations Identified With Phased Array UT Were Correct in Specimen 24Z2 | 48 |
| 70 | Crack Detection Summary for Blind Flaw Detection Study Using Phased Array UT Method Specimen 55Z2 | 48 |
| 71 | Crack Detection Summary for Blind Flaw Detection Study Using Phased Array UT Method Speciment 58K9 | 49 |
| 72 | The POD Curve Showing Performance of Phased Array UT for Detection of Small Subsurface Cracks | 50 |
| 73 | Spherical Geometry of Corrosion Pit in D6AC Material | 52 |
| 74 | Test Specimen With Center Corrosion Pit | 52 |
| 75 | Set of Different Corrosion Pits Produced in the Test Specimens | 53 |
| 76 | Phased Array UT Sectoral Scan Data Showing Accurate Imaging of Small Corrosion Pits | 53 |
| 77 | Phased Array UT Sectoral Scans Showing Typical Signals Used to Detect and Estimate the Size of Corrosion Pits | 54 |
| 78 | The EC Device and Sample EC Signals Produced by Cracked Sites | 54 |
| 79 | The EC Signals From Four Cracks in Specimen 286E | 55 |
| 80 | The EC Signals From Four Cracks in Specimen 24Z2 | 55 |

LIST OF TABLES


| Table | | Page |
|---|---|---|
| 1 | Precracking History of D6AC-2 Unpeened Specimen | 11 |
| 2 | Load-Shedding Parameters for D6AC-2 Specimen | 12 |
| 3 | Results for Test Panel 286E Summarizing Crack Detection and Length Estimation | 46 |
| 4 | Results for Test Panel 24Z2 Summarizing Crack Detection and Length Estimation | 47 |
| 5 | Sample Phased Array UT Inspection Results Showing Ability to Accurately Locate Cracks | 50 |
| 6 | The POD Inspection Results Summary for Crack Detection and Length Estimation | 51 |
| 7 | The EC Results From Panel 286E | 55 |
| 8 | The EC Results From Panel 24Z2 | 56 |

LIST OF ACRONYMS

| | |
|---|---|
| AANC | FAA Airworthiness Assurance NDI Validation Center |
| CGDT | Crack growth damage tolerance |
| CPTD | Committee on Propeller Damage Tolerance |
| C(T) | Compact tension |
| *Da*/*dN* | Crack growth rate |
| DCPD | Direct current potential drop |
| DT | Damage tolerance |
| DTA | Damage tolerance analysis |
| EC | Eddy current |
| EIFS | Equivalent initial flaw size |
| FAA | Federal Aviation Administration |
| FEA | Finite element analysis |
| FEM | Finite element model |
| HCF | High-cycle fatigue |
| HRC | Rockwell C Hardness |
| HS | Hamilton Sundstrand |
| LGCLF | Laser-generated crack-like features |
| NASA JSC | National Aeronautics and Space Administration Johnson Space Center |
| NDI | Nondestructive inspection |
| PD | Potential drop |
| POD | Probability of detection |
| RF | Radio frequency |
| SCT | Surface crack tension |
| UT | Ultrasonic |

# EXECUTIVE SUMMARY

The National Aeronautics and Space Administration Johnson Space Center, in conjunction with Hamilton Sundstrand (HS) and the Federal Aviation Administration Airworthiness Nondestructive Inspection (NDI) Validation Center at Sandia National Laboratories, completed a comprehensive crack growth and fatigue property assessment of the materials used in propeller designs. The test series acquired fracture mechanics data, such as fatigue crack growth rates and threshold values for shot-peened specimens, and surface crack condition specimens made from 7075-T73 and D6AC propeller alloys. Crack growth rates were characterized from threshold to fracture for a range of stress ratio R-values. This work included the development of analyses methods for predicting fatigue crack initiation and growth rates for cracks initiating from different size corrosion pits. The spectrum load test results were then compared with NASGRO® analysis results for both interaction and crack retardation model options. This work allowed the team to understand the crack growth behavior of the most frequent types of damage, such as small cracks, scratches, tool marks, and corrosion pitting under conditions relevant to propeller systems.

HS used this data to conduct the case study, reported here, to determine the viability of applying crack growth damage tolerance to new propeller designs. This portion of the project studied crack growth behavior for frequent types of propeller damage, such as small cracks, scratches, tool marks, and corrosion pitting. Specific tasks assessed the effect of using classic crack growth damage tolerance as the basis for propeller structural design, especially with respect to the weight of the propeller and associated components.

This report describes the results of the propeller damage tolerance study in which Hamilton Sundstrand assessed the impact on propeller weight by using a threshold damage tolerance approach, in addition to meeting current safe-life criteria, as the basis for propeller structural design. Damage threshold behavior was developed by surface crack tension fatigue tests of D6AC steel fatigue specimens with laser-generated crack-like features (LGCLF). The knowledge acquired from these tests was used to develop modified Goodman diagrams of peened and unpeened D6AC steel with 0.015-inch-deep semicircular LGCLF flaws. The resulting curves are lower than existing safe-life allowables used to design the propeller components. Using the modified Goodman diagrams for 0.015-inch-deep LGCLF flaws is considered conservative, based on the known corrosion threats to propeller hardware.

The geometry of the HS Model 568F propeller hub and blade was modified as required to maintain the stress levels below the Goodman curves established for precluding high-cycle fatigue crack propagation from a 0.015-inch surface crack. The weight increase resulting from these modifications was calculated. The redesigned HS Model 568F propeller blade had an increased tulip wall thickness in the fillet region, achieved through an increase in the outside diameter, while the original fillet radius was maintained. The weight increase due to this modification was 0.52 lb per blade or 3.12 lb for all six blades. Due to the nature of the modification of the blade geometry, the increase in the blade weight had no effect on the actuator loads. As the result, the weights of the propeller actuator, oil transfer tube, propeller control module, main pump, and auxiliary pump and motor subassemblies remained unchanged. The hub geometry was modified in four regions: the dome hole, between the arms, the ball loading

hole, and the moment axis fillet. The weight increase due to the hub redesign amounted to 1.3 lb. Associated studies in NDI determined that phased array ultrasonic has sufficient sensitivity to detect small cracks and corrosion pits that may occur in the propeller blades (90% probability of detection level at a crack length of 0.025″).

## 1. INTRODUCTION.

The Federal Aviation Administration (FAA) is considering the creation of damage tolerance guidelines for propellers. Damage tolerance (DT) has been used extensively in the design of fixed-wing aircraft structures, but propellers still exclusively use the safe-life approach, which limits the rotor life to the minimum number of flight cycles required to initiate a crack. The FAA has funded a research and development program to improve damage tolerance technology and its availability to rotorcraft and propeller designers.

Hamilton Sundstrand (HS) was selected to participate in this effort by (1) supporting materials testing and characterization of cracked specimens, and (2) performing a structural design and analysis of a propeller blade and hub using DT as a criterion. The HS Model 568F propeller was used in this study because it represents the current technology at HS, and the finite element models (FEM) generated during the safe-life design of the various components were available. The knowledge obtained from the tests and characterization of cracked specimens was used to establish new materials strengths, which resulted in modifications to the propeller component geometries. Then, the weight increase of a propeller designed using crack growth damage tolerance (CGDT), which was one of the main objectives of the HS study, was calculated.

HS performed several tasks to assess the impact on propeller weight by using CGDT as one criterion for propeller structural design. The first task was to create a test plan to generate material properties [1]. Because of the difficulties testing standard ASTM E 647 compact tension specimens (C(T)) with D6AC steel [2-4] and because of the need to address small cracks in peened material, a surface crack tension (SCT) specimen was selected for determining threshold behavior. To create a sharp notch that mimics a surface crack, a laser was used to generate 0.015-inch-deep semicircular crack-like features [5]. Two materials were tested, 7075-T73 steel and lower hardness D6AC steel (36 Rockwell C Hardness (HRC)). The 7075-T73 was tested first to gain experience with SCT testing with laser-generated crack-like features (LGCLF) in peened material [6]. These LGCLF cracks were assumed to represent a worst-case scenario for initial manufacturing flaws, in-service mechanical damage, and in-service corrosion damage. Once the D6AC tests were complete, the data were analyzed to generate modified Goodman curves for analysis. Next, a structural design and analysis of the propeller components considered for DT, namely, the blade and hub, was performed. The geometry of these components was modified as required to maintain stress levels below the newly established Goodman allowables for CGDT. Finally, the weight increase of the modified propeller components was calculated.

## 2. APPROACH.

The redesigned HS Model 568F propeller blade featured an increased tulip wall thickness, achieved through an increase in the outside diameter, while the original fillet radius was retained. The resulting increase in weight due to the HS Model 568F blade modification was 0.52 lb per blade or 3.12 lb for six blades. Figure 1 shows the cross-section of the tulip modification. The baseline tulip configuration is represented by the broken line, while the modified tulip geometry is represented by the solid line.

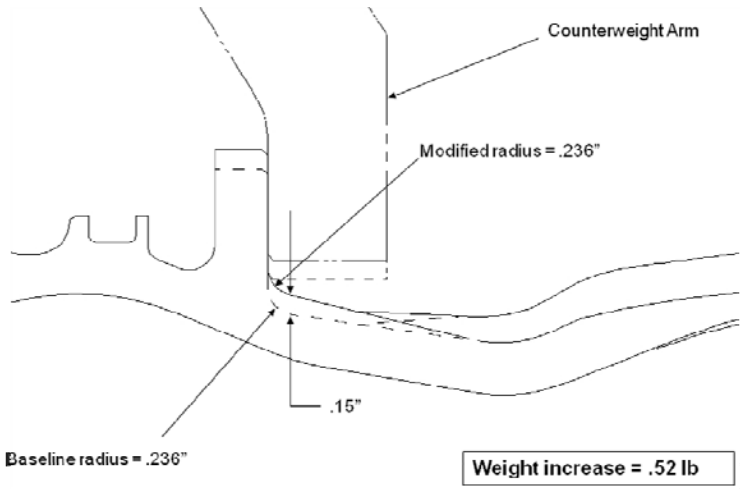


Figure 1. Cross-Section of the HS Model 568F Tulip Modifications (Modification 1)

Since the change in blade weight was due to the increase of tulip wall thickness in the circular section of the blade, there was no change in the twisting moment because the additional weight was evenly distributed along the blade circumference. Therefore, there was no change in actuator loads resulting from the modified blade design. Consequently, the weights of the propeller actuator, oil transfer tube, propeller control module, main pump, and auxiliary pump and motor subassemblies were unchanged.

The hub geometry modifications were confined to four regions: the dome hole, between the arms, the ball loading hole, and the moment axis fillet. The total weight increase of the HS Model 568F hub geometry was 1.3 lb. Figure 2 shows the cross-section of the hub modifications. The original hub geometry is shown in magenta and the modified hub is in blue.

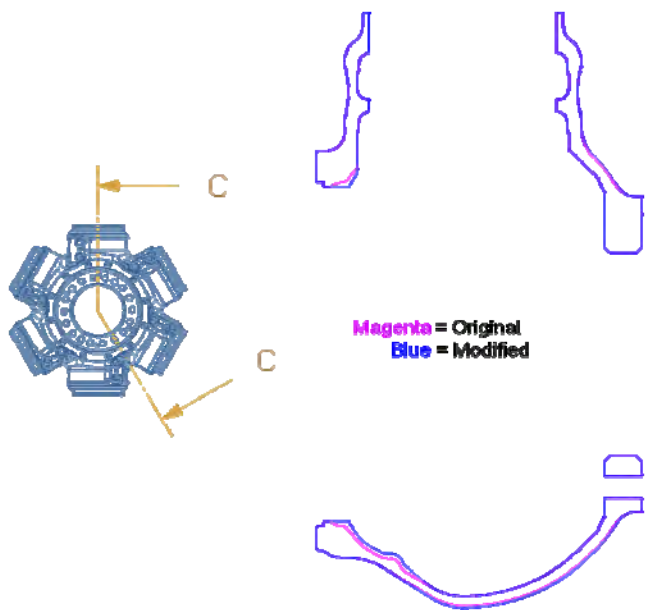


Figure 2. Cross-Section of the HS Model 568F Hub Geometry Modifications

## 3. DISCUSSION.

The following sections describe the steps that were taken to establish the DT allowables for the peened and unpeened D6AC steel with LGCLF as well as the modifications made to propeller components, specifically, the blade tulip and hub geometry, to maintain the stress levels below the newly established allowables for CGDT.

### 3.1 D6AC FATIGUE TESTING AND DT ALLOWABLES.

#### 3.1.1 Specimen Preparation and Testing.

The National Aeronautics and Space Administration Johnson Space Center (NASA JSC) obtained a forged block (8 by 8 by 25 inches) of D6AC steel (per AMS 6431) for machining test specimens. The specimen dimensions are shown in figure 3. The specimens were roughly machined into long, rectangular bars before it was realized that the material was not heat treated to the correct hardness of 36 HRC. The bars were subsequently heat treated at NASA JSC and became bowed. The specimens were further milled and ground finished to a ~0.45-inch thickness and then water-jet cut to a dogbone shape and finished machined on a CNC mill. To reduce any residual stresses from the machining of the bowed specimens, the specimens were sent to HS for reheat treating. The specimens were checked before and after reheat treating and no bowing occurred, i.e., the specimens remained flat. The same heat treatment was performed on both specimens and HS Model 568F tulips. Next, shot peening was performed.

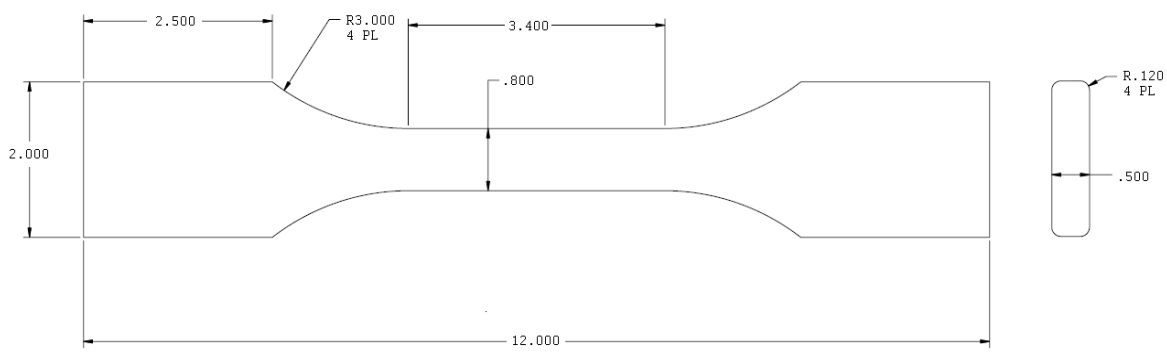


Figure 3. Surface Crack Tension Specimen Before Laser Notching (12X-1956)

Thirty-one specimens were shot peened and thirteen were not. The peening was performed by Peening Technologies of Georgia. For full saturation, the specimens were shot peened six times with S230 shot type I per MIL-S-851, 0.008-0.012A intensity, and 100% coverage. HS hole drilled several specimens in the grip areas and one specimen was sent to Lambda-Technologies, LLC for x-ray diffraction to determine the residual stress profile through the thickness. Figure 4 shows the residual stress measurements on the specimens. The HS hole-drilling method to determine the depth of cold work was comparable to the x-ray diffraction crossover from compression to tensile stresses, as shown in figure 4. Also shown is the residual stress measurement from a blade tulip returned from service (manufactured by ACES Columbia). The surface residual stress measurements were also comparable.

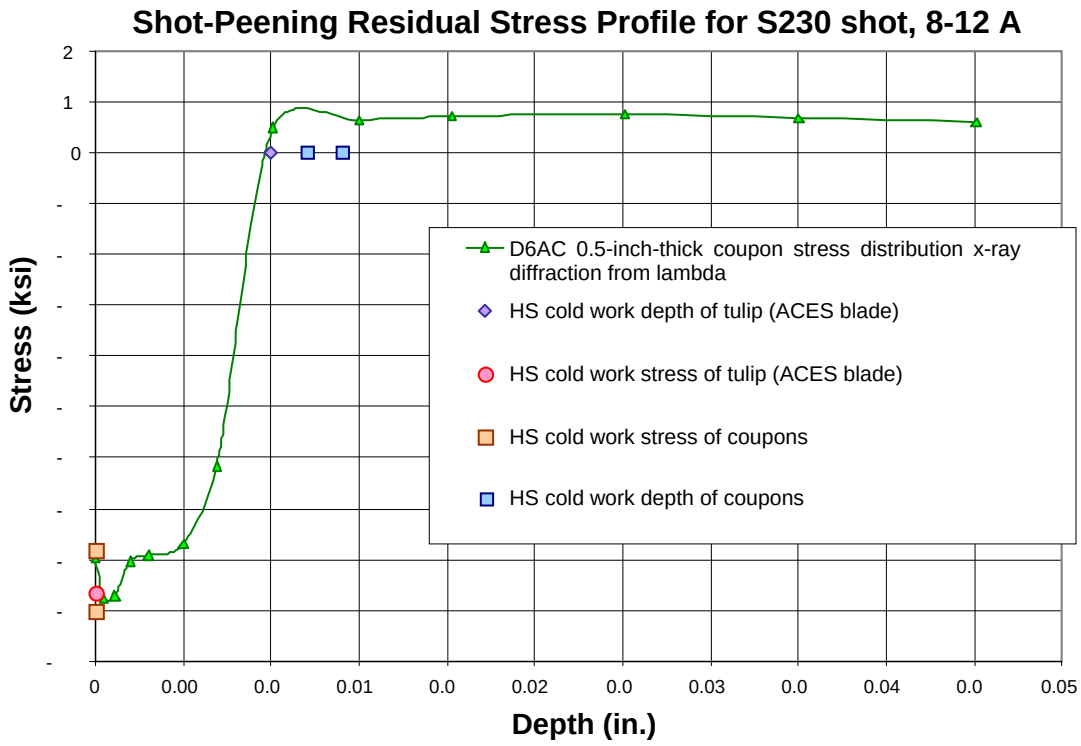


Figure 4. Shot-Peening Residual Stress Measurements for 12X-1956 Specimens

Satisfied that the peening was performed properly, the peened and unpeened specimens were then submitted to the Connecticut Center for Advanced Technology (CCAT) for laser notching. The 0.015-inch-radius LGCLF flaws were created with 27 individual laser passes, using a 20-watt Ytterbium fiber laser. The laser passes were done in groups of three, with the first pass at a 20-kHz pulse frequency aimed at material removal and the next two passes at 80 kHz aimed at cleaning out some of the recast created by the first pass. The first group of passes was made at the highest power level with the shortest travel length. Each consecutive group was made at successively lower power settings and successively larger travel lengths, with the last group at the lowest power and 0.030 inch in length. Figure 5 shows a cross-section of a laser notch in D6AC. In this photograph, the sample has been etched with nital etch to highlight the recast and the heat-affected zone. The recast structure is shown in yellow. The recast area was minimal for this process and considered acceptable. The notches were very narrow and sharp at the bottom and were considered a more close simulation of an actual fatigue crack than an electric discharge machining notch. All samples were notched at the middle of the test sections on one side only prior to test and then shipped to Sandia National Laboratories for nondestructive evaluation, using a phase-array pulse echo technique.

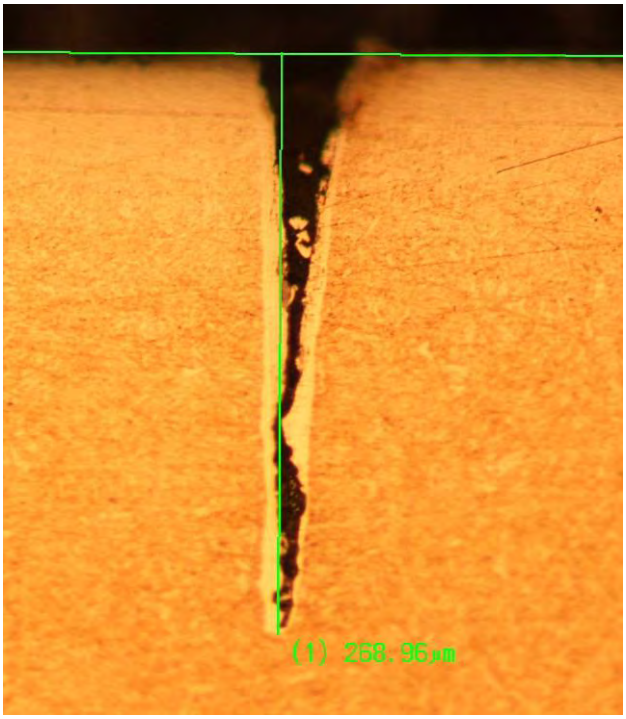


Figure 5. Microphotograph of Semicircular D6AC LGCLF, Etched With Nital

The fatigue tests were performed at two places: NASA JSC, Houston, TX, and the FAA William J. Hughes Technical Center, Atlantic City International Airport, NJ. The fatigue tests consisted of three phases: (1) determination of initial thresholds by precracking to obtain small growth (0.002-0.010 inch) in less than 2 million cycles, (2) determination of fatigue crack arrest thresholds by a fracture mechanics load-shedding test to obtain $da/dN<9\text{x}10^{-10}$, plus *da/dN* (crack growth rate) data in threshold region, and (3) determination of fatigue crack growth rate data by constant loading for approximately 0.15-inch growth at or above the threshold *da/dN* region data. The data from the Phase 1 tests were used to determine the modified Goodman diagrams. The fatigue tests were performed using the direct current potential drop (DCPD) technique for determining crack initiation and growth. This DCPD technique uses four very fine platinum wires welded to the specimens at four locations to act as measuring probes. Two active probes were welded very close to the laser-machined flaws and two reference probes were welded at locations away from the crack to act as reference signals. An automated fatigue crack growth system, developed by Fracture Technology Associates, was used to monitor the DCPD signals to correlate to crack growth length. The method measures voltage, or electric potential drop (PD), due to the change in electric field as a result of crack extension. In addition to this measurement, optical measurements were taken of the crack length on the surface or after the specimen was broken open at the end of the test. Hence, cycles to initiate a small crack can be obtained, as well as conventional *da/dN* data, assuming semicircular crack growth. The semicircular crack growth is a valid assumption for unpeened data only, given that peened data are susceptible to tunneling effects from the residual stresses being highly compressive on the surface and slightly tensile at the bottom of the laser-machined flaws.

3.1.2 Test Results and Discussion.

3.1.2.1 Phase 1.

Figures 6 and 7 show the fatigue crack initiation (growth) and runout (no growth) data for $R = 0.1$ and $R = 0.7$. $R$ is the stress ratio (minimum/maximum). For steel, a runout at 2 million cycles is sufficient for endurance limit ($10^8$ cycles), due to the flatness of curves in the high-cycle regime. High-cycle fatigue (HCF) $R = 0.1$ runouts for peened and unpeened D6AC were 43 and 33 ksi, respectively. HCF $R = 0.7$ runouts for peened and unpeened D6AC were 66 and 58 ksi, respectively. This information was then used to generate the modified Goodman diagrams for peened and unpeened D6AC. This was accomplished by using $R = 0.1$ unflawed data [7] to first create the $R = 0.1$ Kitigawa-El Haddad diagrams (figures 8 and 9). These diagrams account for the small-crack effect on threshold, since most threshold data are from long-crack C(T) specimens.

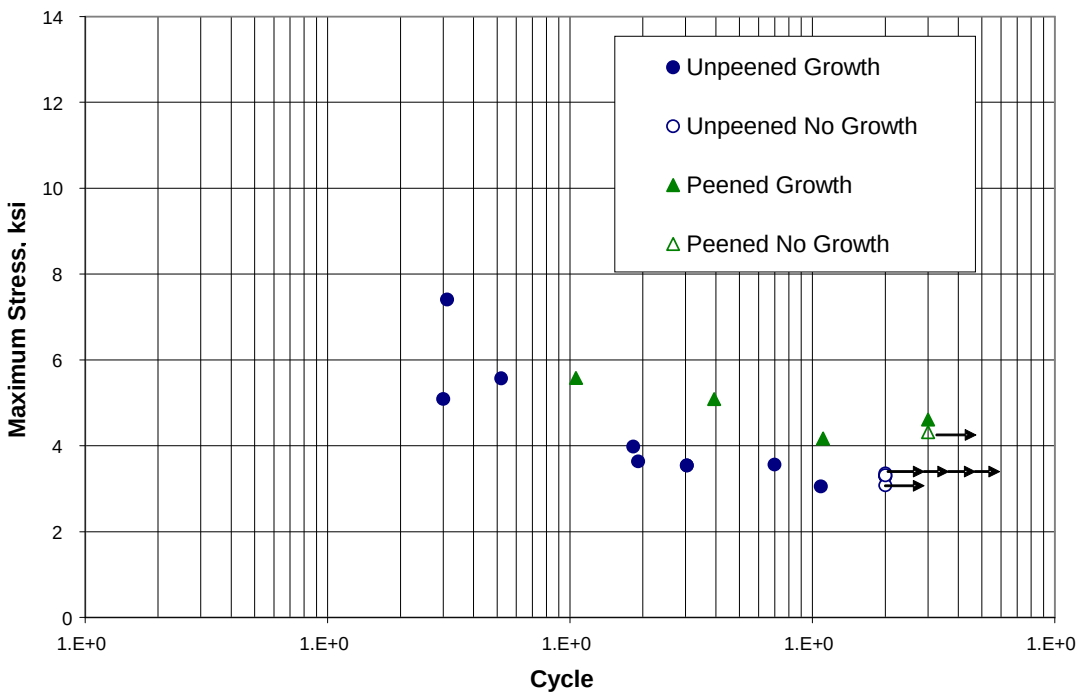


Figure 6. Crack Initiation Data D6AC 0.015″ x 0.030″ LGCLF, $R = 0.1$

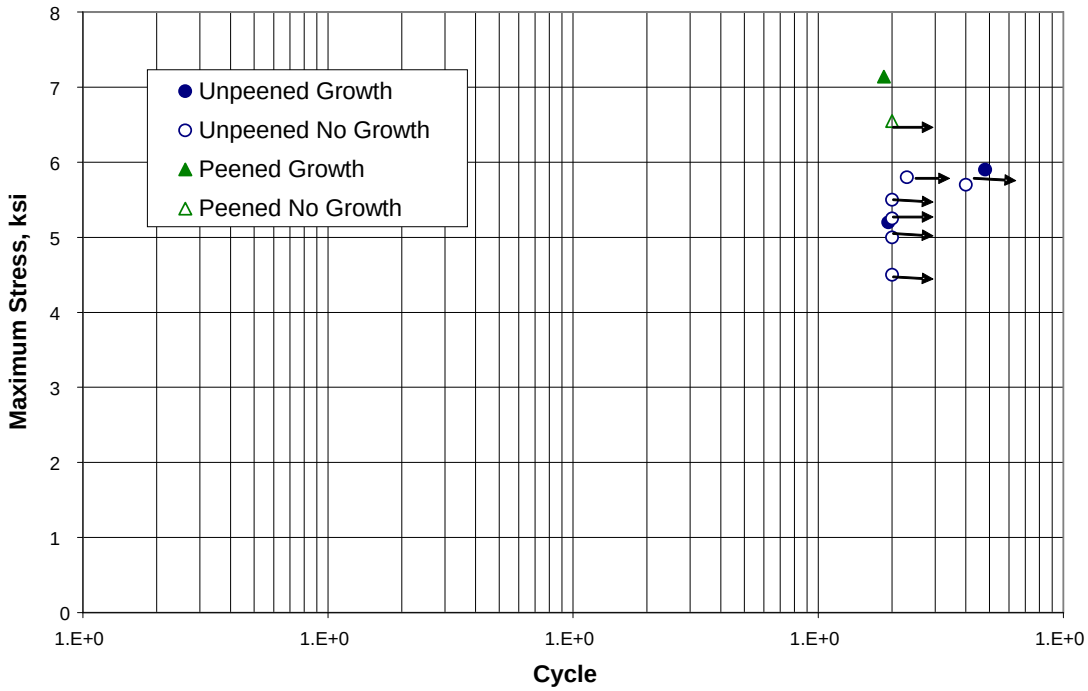


Figure 7. Crack Initiation Data D6AC 0.015″ x 0.030″ LGCLF, $R$ = 0.7

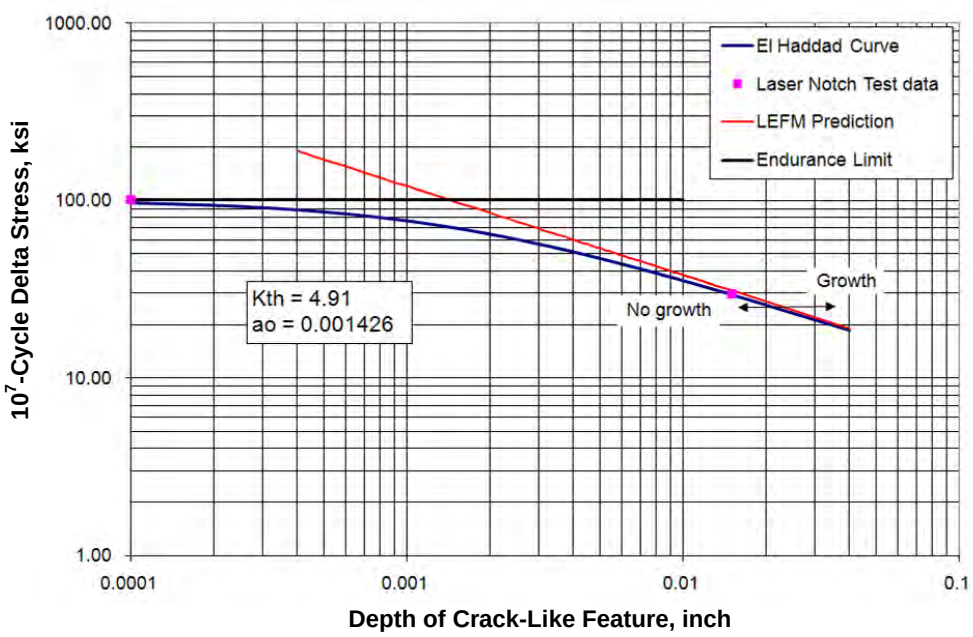


LEFM = Linear Elastic Fracture Mechanic

Figure 8. Effect of LGCLF on Unpeened D6AC 35 HRC Kitigawa-El Haddad Diagram

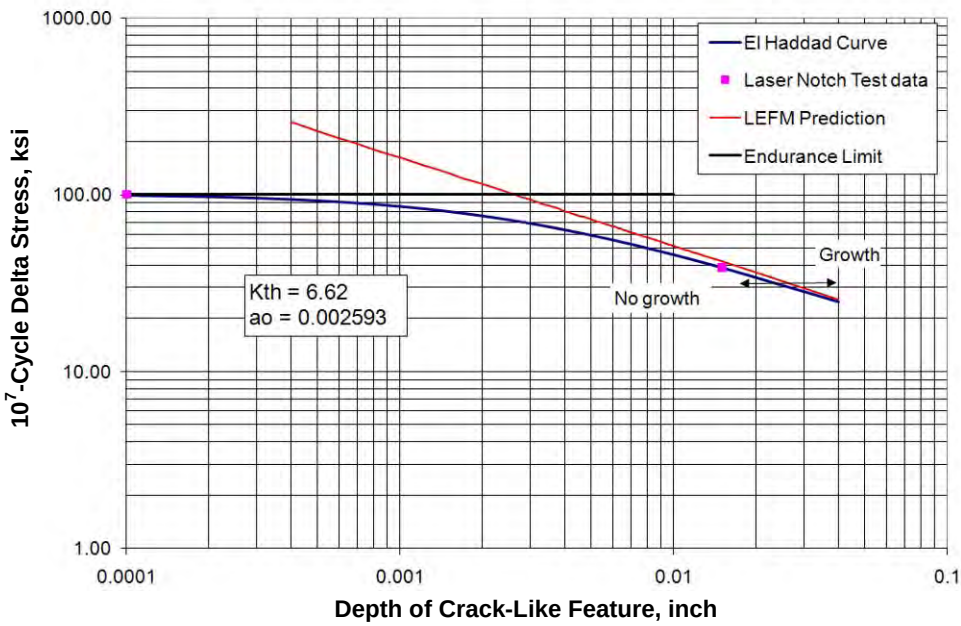


LEFM = Linear Elastic Fracture Mechanic

Figure 9. Effect of LGCLF on Peened D6AC 35 HRC Kitigawa-El Haddad Diagram

The outputs from the Kitigawa-El Haddad diagrams are $\Delta K_{th}$ at $R$ = 0.1 and $a_0$ (intrinsic crack length), using equations 2 and 3:

$$a_0 = \frac{1}{\pi}\left(\frac{K_{th}}{F \cdot S_e}\right)^2 \tag{2}$$

$$\Delta K_{th} = \frac{K_{th}}{F\sqrt{\pi(a + a_0)}} \tag{3}$$

$\Delta K_{th}$ is the stress range (maximum-minimum); $K_{th} = \Delta K_{th}$ at $R$ = 0.1, the long-crack threshold; $F$ = 0.728, shape factor for semicircular surface crack; and $S_e$ = 100.8 ksi, $\Delta K_{th}$ endurance limit at $R$ = 0.1. These values are then used with the NASGRO® equations 4 and 5 to generate the fracture screening curves by adjusting the $\Delta K_1$ and $C_{th+}$ value to match the $K_{th}$ at $R$ = 0.1 and 0.7.

$$\Delta K_1 = K_{th}\sqrt{\frac{a}{a + a_0}} \tag{4}$$

where $\Delta K_1$ is the threshold as $R$ approaches 1.

$$\Delta K_{th} = \Delta K_1\left(\frac{1 - R}{1 - f \cdot R}\right)^{(1+RC_{th+})} / (1 - a_0)^{(1-R)C_{th+}} \text{ for } R \geq 0 \tag{5}$$

where $f$ is the Newman closure function and $a_0$ is a closure constant, based on $\alpha$ = 2.5, $S_{max}/\sigma_0$ = 0.3. For $R$ <0, another equation is used similar to equation 5, with a $C_{th-}$ = 0.1. The normalized fracture screening curves are shown in green in figures 10 and 11 for peened and unpeened D6AC, respectively.

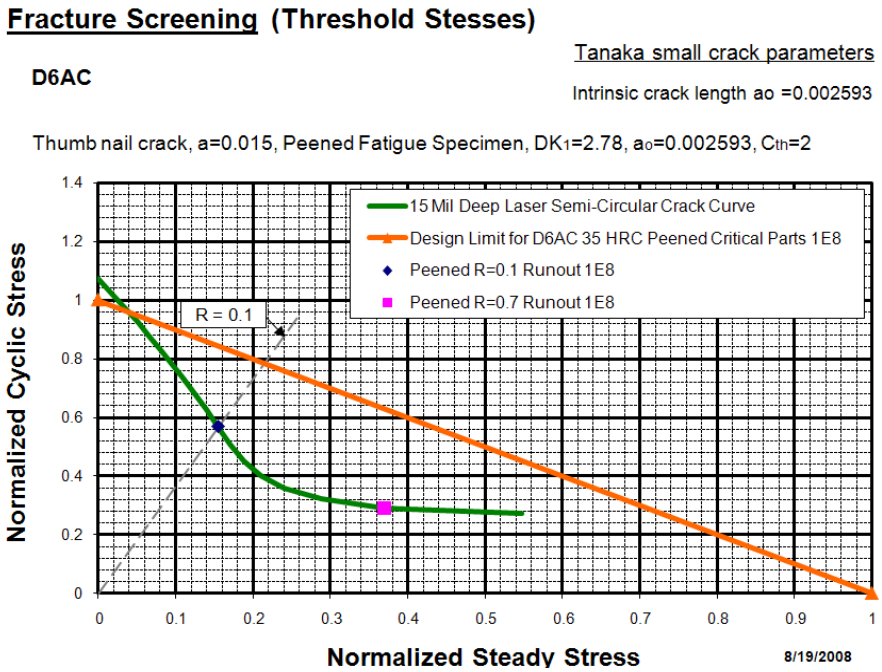


Figure 10. Modified Goodman Diagram for 0.015-Inch-Radius LGCLF for Peened D6AC

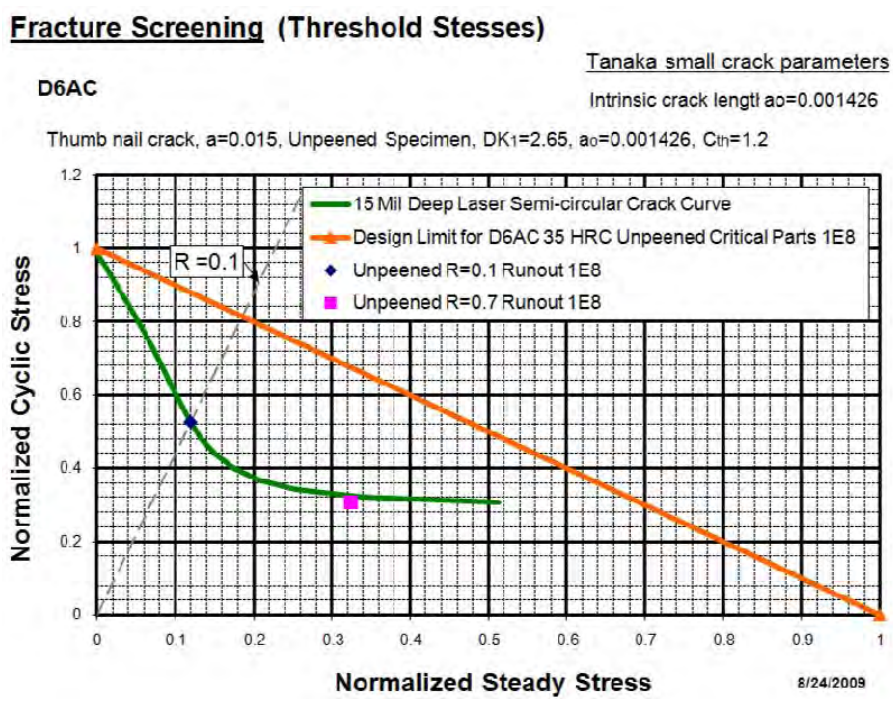


Figure 11. Modified Goodman Diagram for 0.015-Inch-Radius LGCLF for Unpeened D6AC

The $K_{th}$ or $\Delta K_{th}$ at $R$ = 0.1 value determined was 4.91. Note that shot peening increases the $\Delta K_{th}$ at $R$ = 0.1 value from 4.91 to 6.62 ksi·in.$^{1/2}$ for the flaw size in question. Therefore, shot peening has been demonstrated to be effective in raising the DT threshold for these 0.015-inch-deep LGCLF flaws. The shot-peening benefit was also noted in previous studies [7 and 8], when pitted specimens were tested. Figures 12 and 13 show the pitted specimens versus the LGCLF specimens tested at $R$ = 0.1. The pitted specimens were tested to complete fracture, while the LGCLF specimens were tested until cracks grew 0.004-0.010 inch. Hence, pits or corrosion trenches do not act like cracks or like LGCLF flaws, and therefore, using LGCLF could be construed as conservative for known threats of corrosion. The LGCLF flaws may be appropriate for other flaws, such as untempered martensite from a lightning strike.

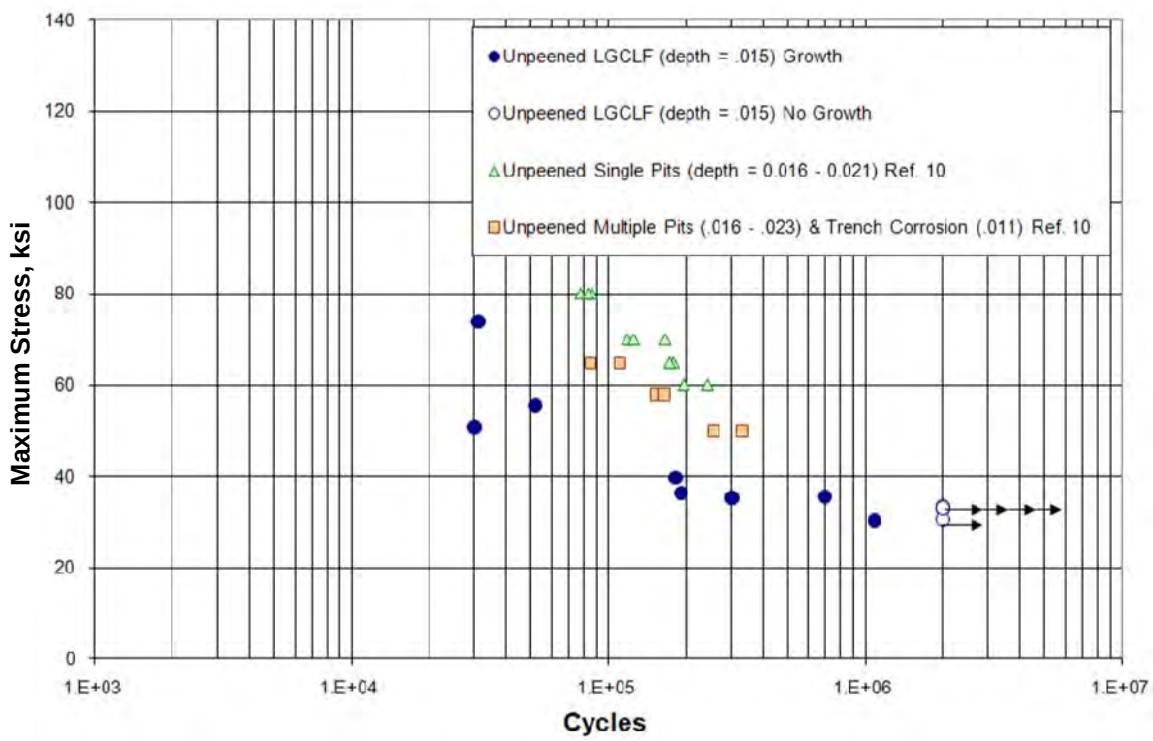


Figure 12. D6AC Unpeened $R$ = 0.1, LGCLF and Pits Generated in HS Laboratory

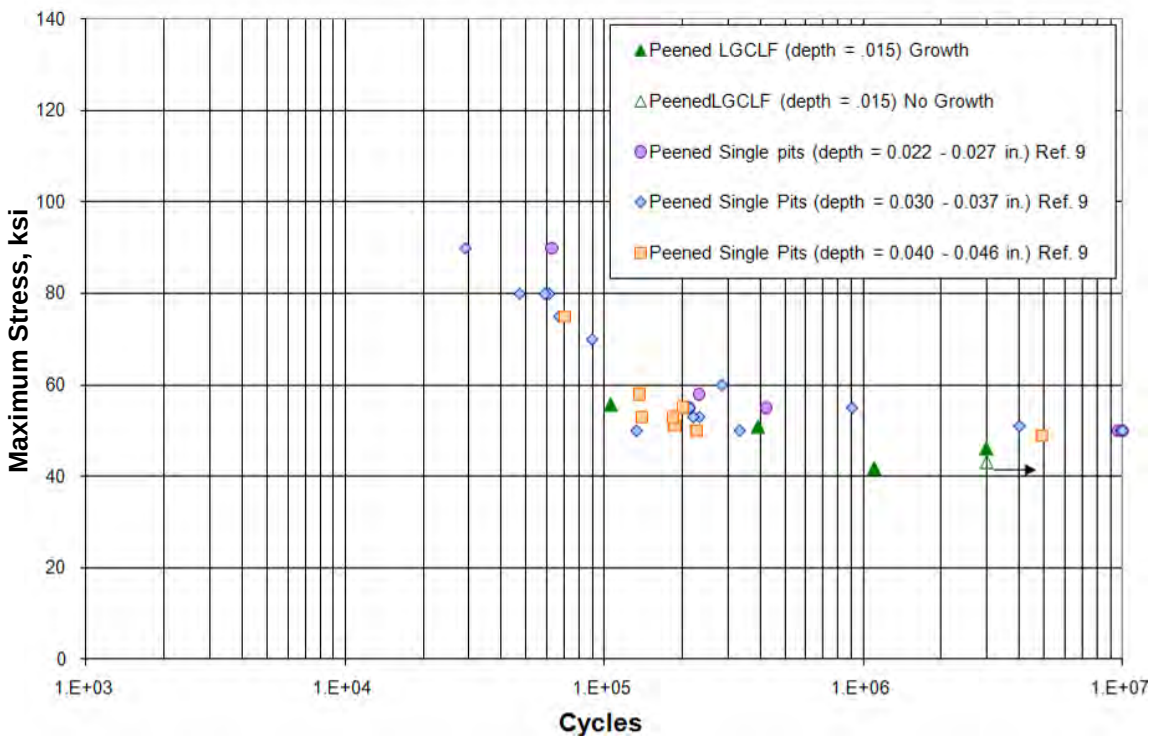


Figure 13. D6AC Peened $R$ = 0.1, LGCLF and Pits Generated in HS Laboratory

3.1.2.2 Phases 2 and 3.

Determination of fatigue arrest thresholds from *da/dN* testing yielded some interesting results for surface crack testing. Table 1 shows the precracking history for specimen D6AC-2. Four levels were run without growth and the last level showed growth of 0.003 inch. The stress-intensity factor ($\Delta K$) was 4.96 after crack initiation to 0.003 inch and 4.43 after growth of another 0.0183 inch (table 2). Hence, the previous calculation for initiation threshold of 4.91 appears reasonable compared to these conventional fracture mechanics fatigue crack growth results. The *da/dN* plot for D6AC-2 is shown in figure 14.

Table 1. Precracking History of D6AC-2 Unpeened Specimen

| Level | Stress (ksi) | No. of Cycles | Initial PD Crack Length (inch) | Final PD Crack Length (inch) | |
|---|---|---|---|---|---|
| 1 | 25.3 | 2,000,000 | 0.0145 | 0.0145 | No growth |
| 2 | 27.8 | 2,000,000 | 0.0145 | 0.0145 | |
| 3 | 30.4 | 2,000,000 | 0.0145 | 0.0145 | |
| 4 | 32.9 | 2,000,000 | 0.0145 | 0.0145 | |
| 5 | 35.4 | 303,753 | 0.0145 | 0.0175 | |

Table 2. Load-Shedding Parameters for D6AC-2 Specimen

| Load Shedding | D6AC-2 ($R$ = 0.1) |
|---|---|
| Maximum loading (kip) | 14 |
| Initial crack length (in.) | 0.0175 |
| Final crack length (in.) | 0.0358 |
| Crack length increment | 0.001 |
| Initial count | 0 |
| Final count | 16,600,000 |
| Initial $K_{max}$ (ksi·in.$^{1/2}$) | 5.51 |
| Initial $\Delta K$ (ksi·in.$^{1/2}$) | 4.96 |
| Final $K_{max}$ (ksi·in.$^{1/2}$) | 4.92 |
| Final $\Delta K$ (ksi·in.$^{1/2}$) | 4.43 |
| $K$ gradient (in.$^{-1}$) | -7 |
| Frequency (Hz) | 15 |

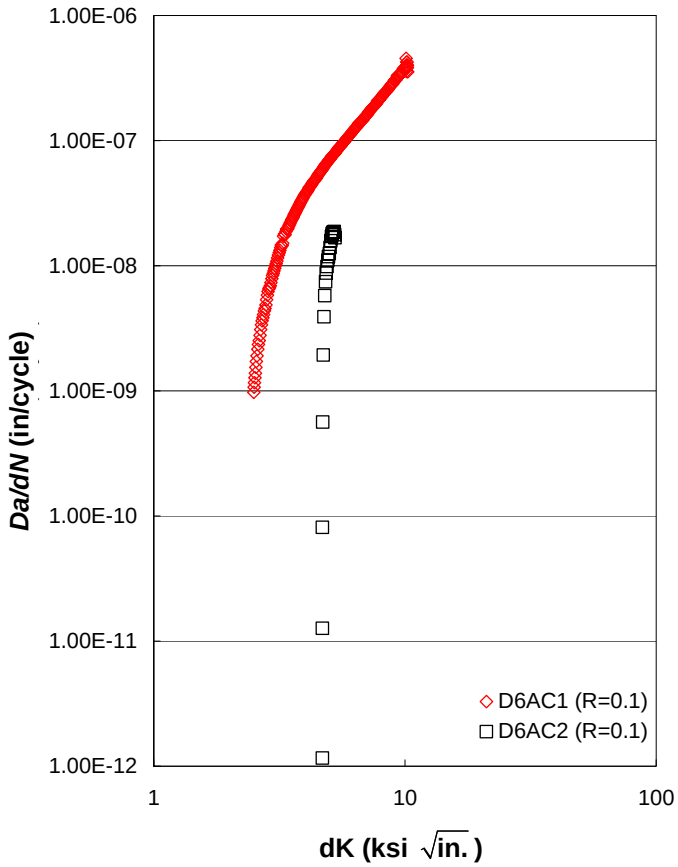


Figure 14. The *da/dN* Plot for D6AC-2 Using the SCT Specimen

Figure 14 also shows the *da/dN* surface crack behavior of D6AC-1, which was markedly different from D6AC-2 because the initial precracking was done at a much higher stress level, and the crack grew to 0.030 inch before starting the load-shedding test. At the end of the load-shedding test, near threshold, the crack had grown to 0.2435 inch, and the arrest threshold was much lower, 2.52. This emphasizes the problems with determining thresholds based on arrest threshold.

Similar problems have been experienced by others when determining an arrest threshold for D6AC using C(T) and other through-crack geometry specimens. Forth, et al. [2-4], produced a variety of results at $R$ = 0.1 for arrest threshold for D6AC (figure 15). They claim that the difference is related to different crack closure effects that result in a lack of similitude between test methods. This lack of similitude was also found in reference 9, where Newman had difficulty correlating C(T) test data at $R$ = 0.1 for D6AC (figure 16). Hence, determining thresholds for D6AC needs to be done with specimens that represent actual surface cracks. The LGCLF is the closest flaw geometry to actual surface cracks.

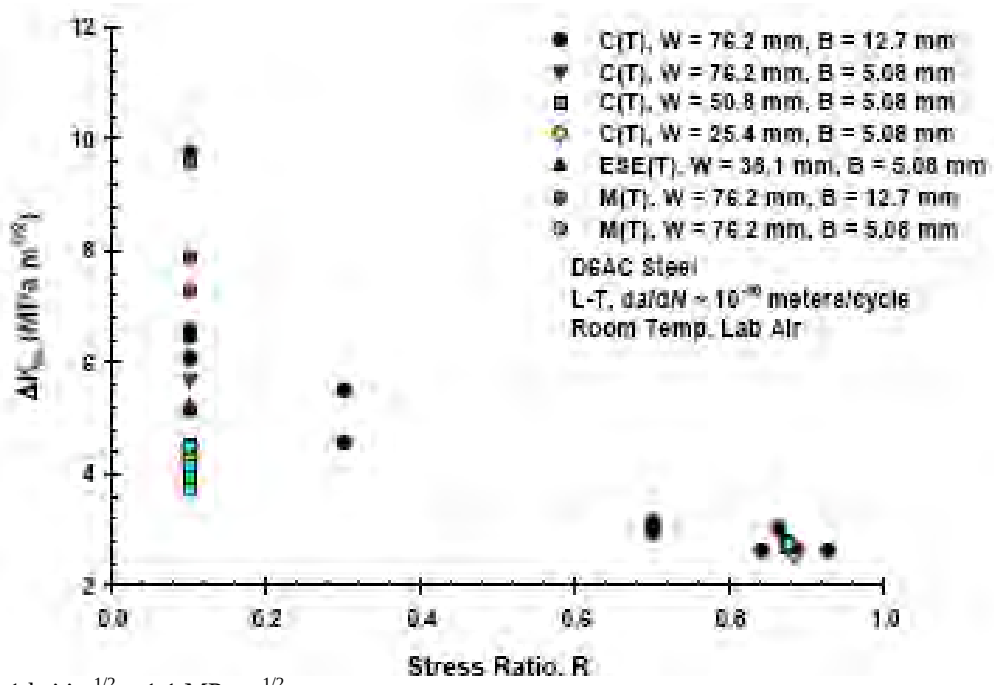


1 ksi·in.$^{1/2}$ = 1.1 MPa·m$^{1/2}$

Figure 15. Threshold Plot of D6AC [2]

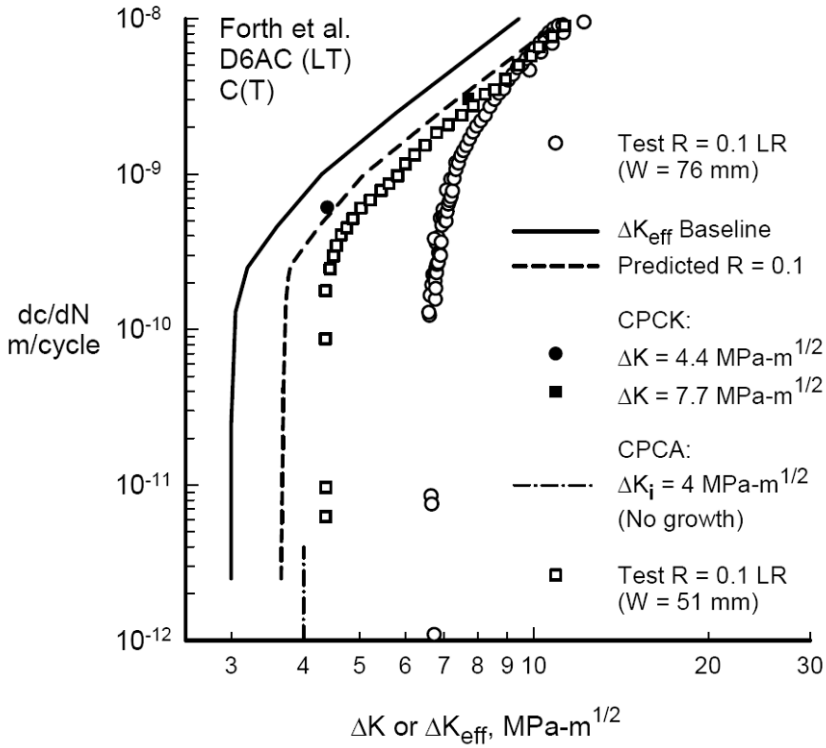


1 ksi·in.$^{1/2}$ = 1.1 MPa·m$^{1/2}$

Figure 16. Near Threshold Data Curve for D6AC Steel [9]

## 3.2 THE HS MODEL 568F BLADE MODIFICATION BASED ON CGDT ALLOWABLES.

The HS Model 568F blade was one of the propeller components whose geometry was modified based on the newly established Goodman allowables for CGDT. The FEM generated during the safe-life design was already available. The original HS Model 568F FEM modeled the entire blade with fine mesh focused on the fillet peak stress area but the remaining portion of the tulip had a coarse mesh. The finite element analysis (FEA) for this model was performed with boundary conditions applied to the tulip. Figure 17 shows the original FEM of the HS Model 568F blade. Figure 18 shows the tulip area of the original HS Model 568F blade FEM.

Figure 17. Original HS Model 568F Blade FEM—Full Blade

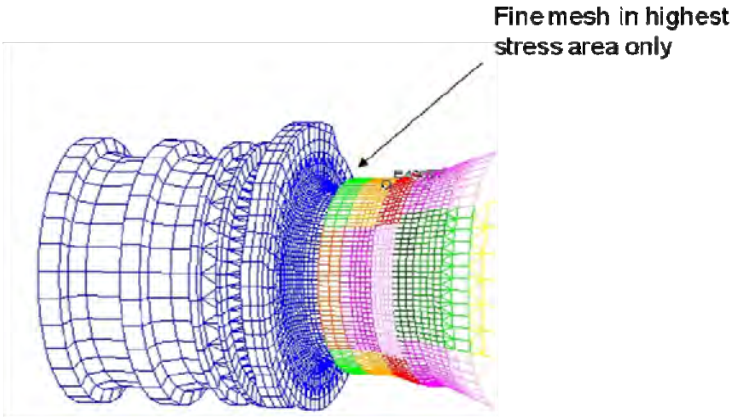


Figure 18. Original HS Model 568F Blade FEM—Tulip Area

The new body of revolution FEM for the HS Model 568F blade included the steel tulip, the graphite spar, and inner composite doubler, as shown in figure 19. The length of the blade portion of the model was extended to eliminate any issues with the boundary conditions. The mesh in the tulip region was refined.

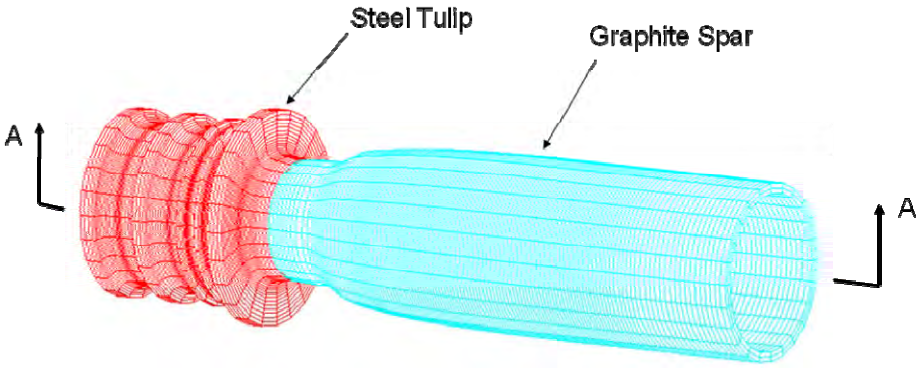


Figure 19. New HS Model 568F Blade FEM—Body of Revolution

Section A-A from the FEM shown in figure 19 with the labeled steel tulip, graphite spar, and composite doubler is shown in figure 20. Figure 21 shows the enlarged view of section A-A.

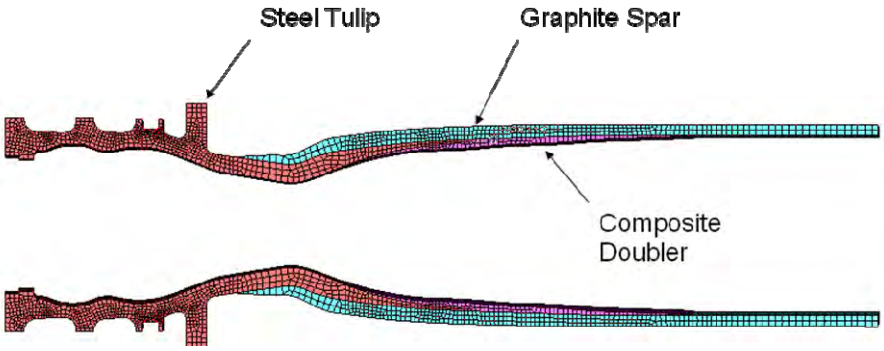


Figure 20. New HS Model 568F Blade FEM—Section A-A

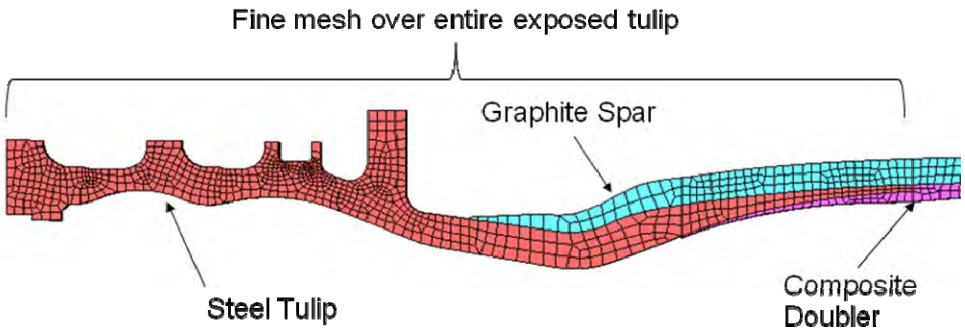


Figure 21. New HS Model 568F Blade FEM—Section A-A Enlarged

The counterweight arm was added to the new FEM, as shown in figure 22, to better represent the distribution of the applied loads. Bearing loads were calculated from a separate model, which included the hub, bearings, and the blade. The ball bearing loads were calculated using a NASTRAN model with the proper moment, shear, and axial loads. The bearing loads were then applied to the HS Model 568F blade with the blade clamped at the end—the inverse of applying operational loads while monitoring the resulting bearing loads. Figure 22 shows the location of the applied ball bearing loads and blade constraints.

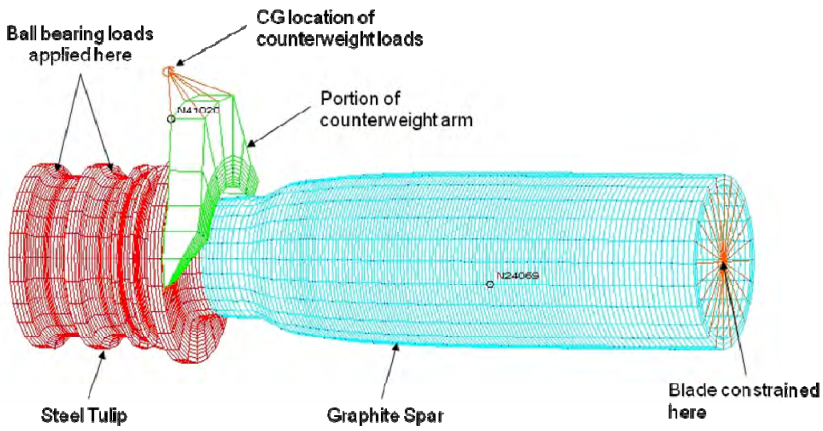


Figure 22. The HS Model 568F Blade FEM

The composite blade connection to the tulip is considered integral and the bond line was not included in the model. Figure 23 shows the spanwise cut through the FEM of the HS Model 568F blade with the added counterweight arm.

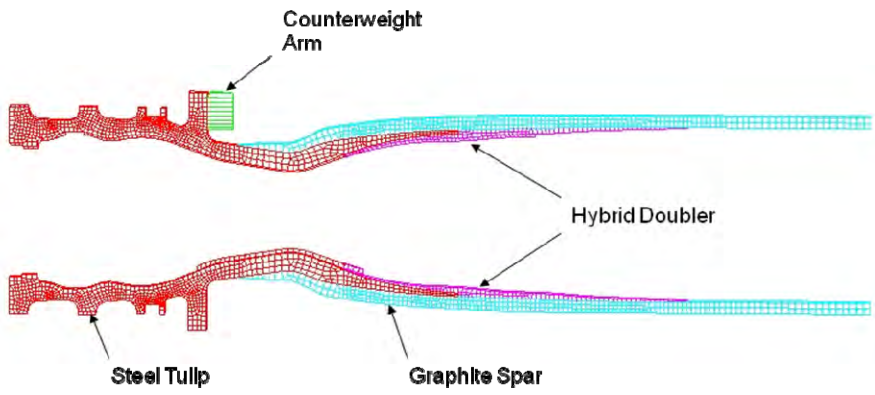


Figure 23. Spanwise Cut Through the FEM

Figure 24 shows the tulip elements of the FEM, while the induction-hardened and shot-peened regions of tulip are shown in the spanwise cut in figure 25.

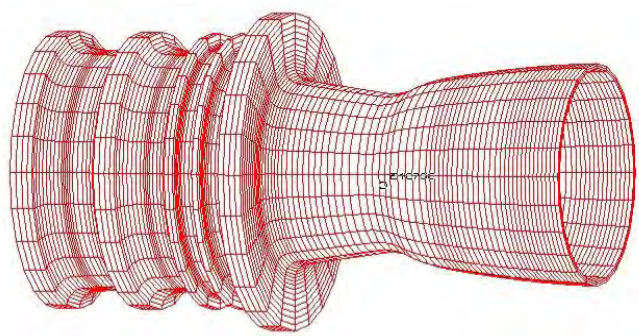

Figure 24. Finite Element Model—Tulip Elements

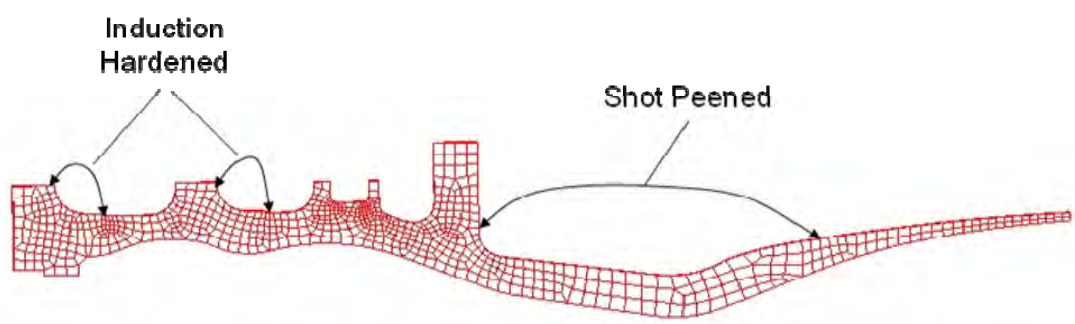


Figure 25. Spanwise Cut Through the Tulip

The HS Model 568F body of revolution FEM was calibrated to the analysis performed with the entire blade (see section 3.2), which was validated with stress survey and fatigue test strain gage data. The peak stress regions in the critical fillet areas of the tulip were studied to assess the blade design. Figure 26 shows the normalized steady principal stress distribution in the tulip at

the key operating condition, and the normalized cyclic principal stresses are shown in figure 27. Both figures indicate that the maximum stresses are located in the tulip fillet radius.

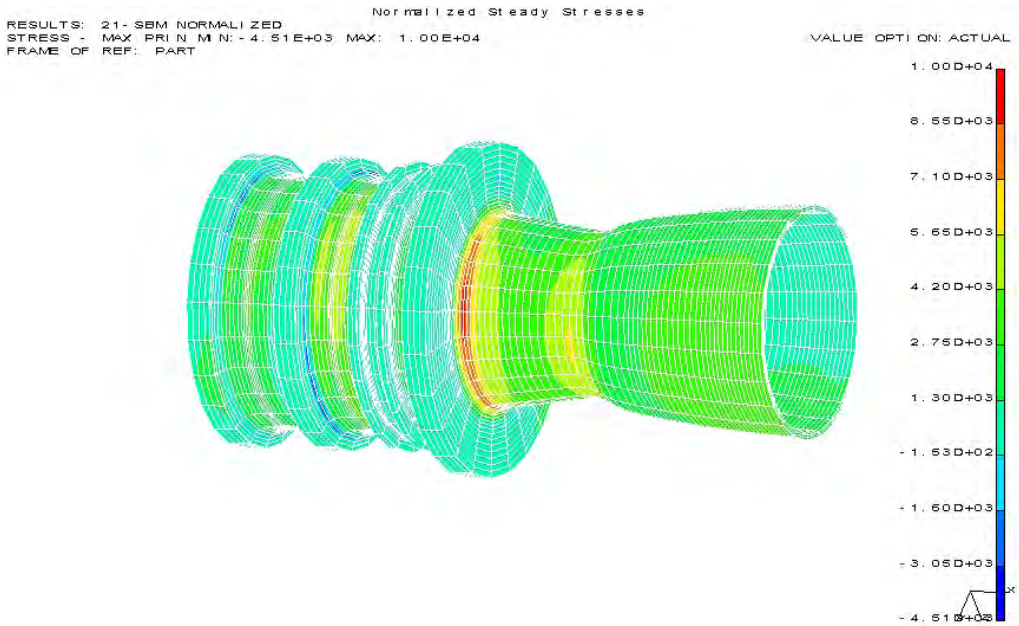


Figure 26. Normalized Steady Principal Stresses in Baseline HS Model 568F Tulip

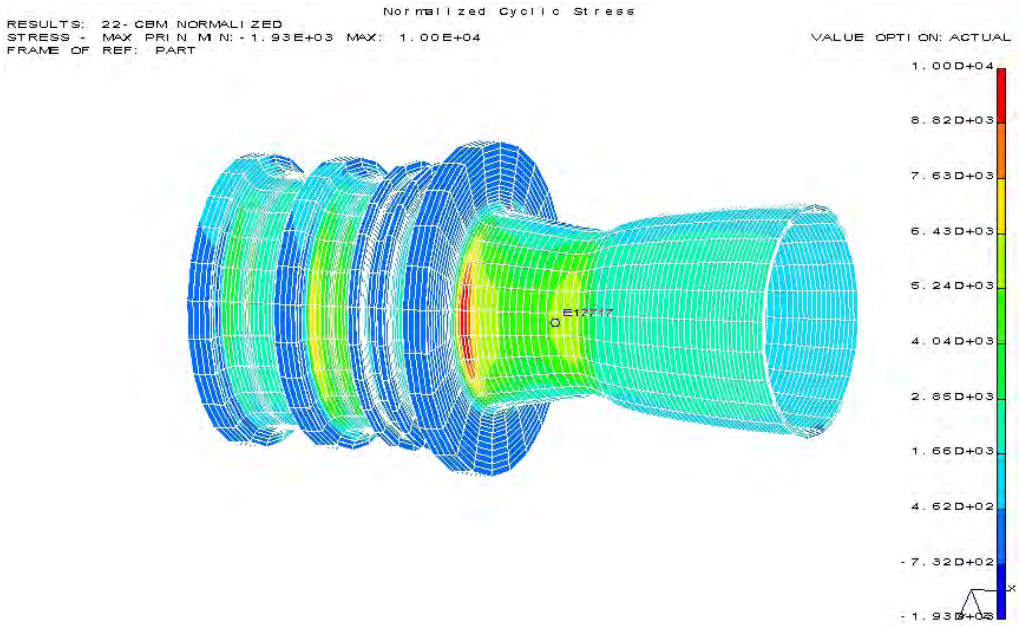


Figure 27. Normalized Cyclic Principal Stresses in Baseline HS Model 568F Tulip

The maximum stress in the tulip fillet radius was plotted on the modified Goodman diagram and was above the established Goodman allowables for CGDT, as indicated in figure 28.

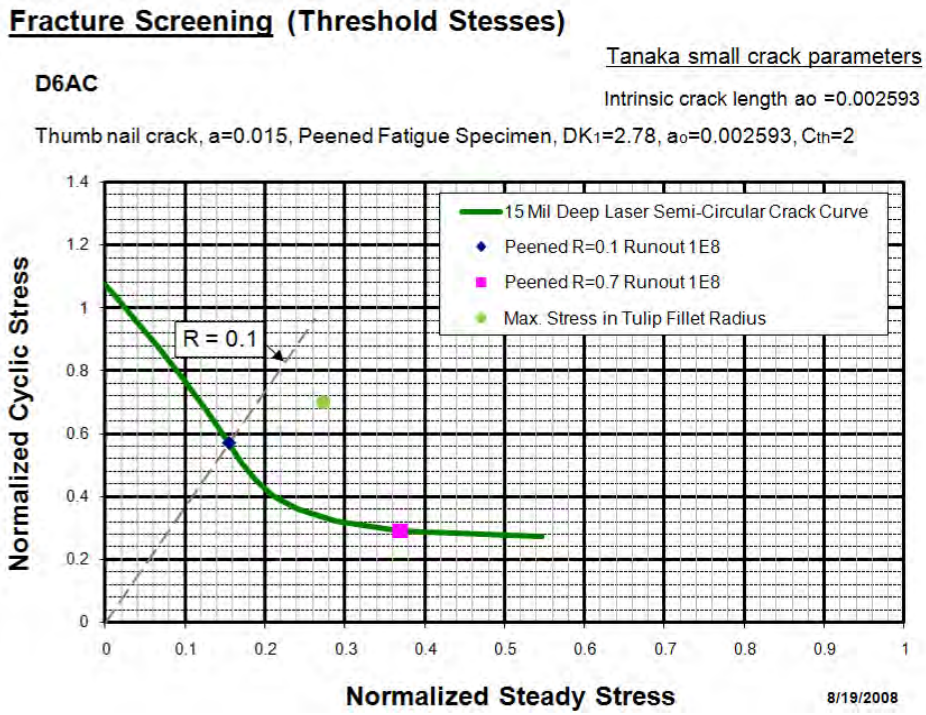


Figure 28. Goodman Diagram for HS Model 568F Tulip—Peened

Stress margins were calculated to determine the overstressed regions in the peened tulip fillet area (figure 29) and unpeened adjacent areas (figure 30). The overstressed areas are shown in blue and green. The figures indicate that the HS Model 568F tulip is overstressed only in the peened area with no overstress extending to the unpeened regions.

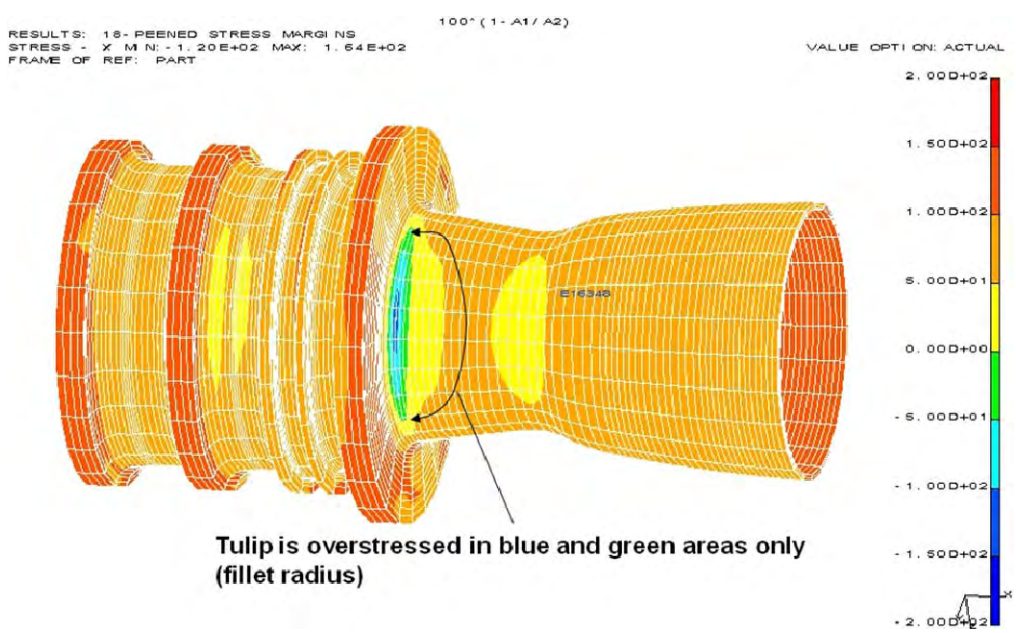


Figure 29. Principal Stress Margins in Baseline HS Model 568F Tulip—Peened

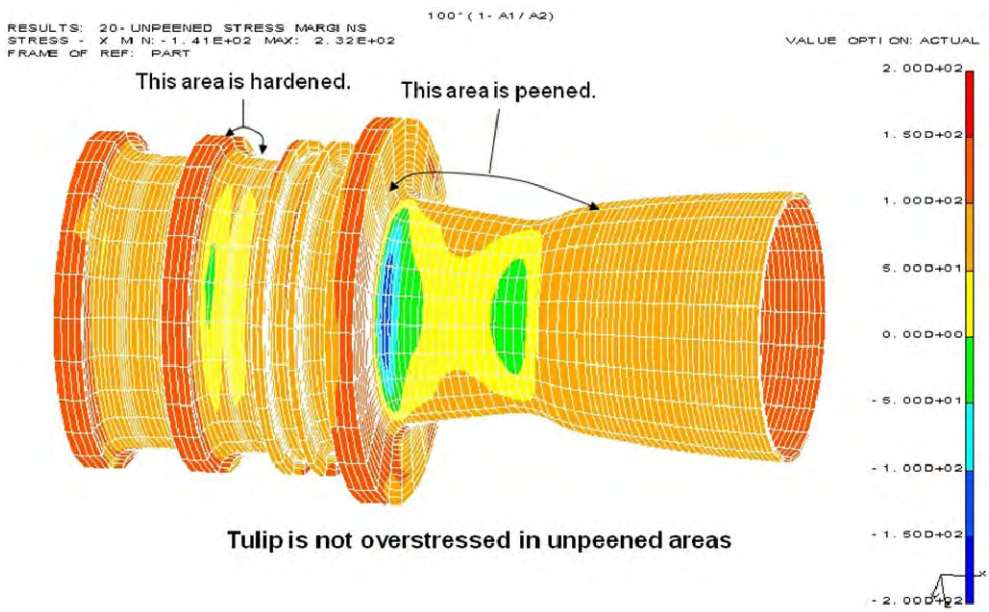


Figure 30. Principal Stress Margins in Baseline HS Model 568F Tulip—Unpeened

Several tulip redesigns were analyzed to quantify the effects of changing the wall thickness and fillet radius in the high-stress region. Tulip modification 1 featured an increase in the outside diameter in the fillet area of the tulip while maintaining the original fillet radius (figure 1). The weight increase due to tulip modification 1 was 0.52 lb per blade. In tulip modification 2, the outside diameter of the tulip was increased with an increase in the fillet radius (figure 31). The increase in weight due to this redesign was 0.60 lb per blade. In tulip modification 3, the wall thickness was increased by decreasing the inside diameter in the high-stress areas, as shown in figure 32. The weight increase due to the third redesign was also 0.60 lb per blade.

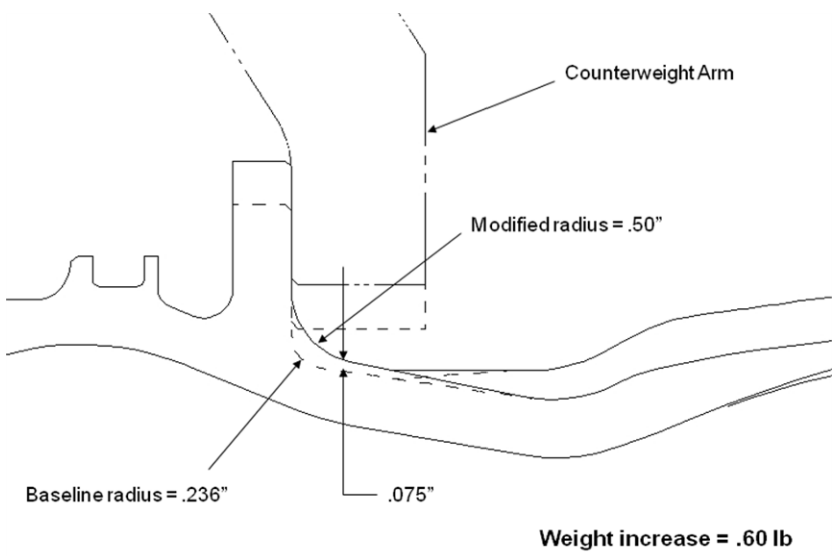


Figure 31. The HS Model 568F Tulip Modification 2

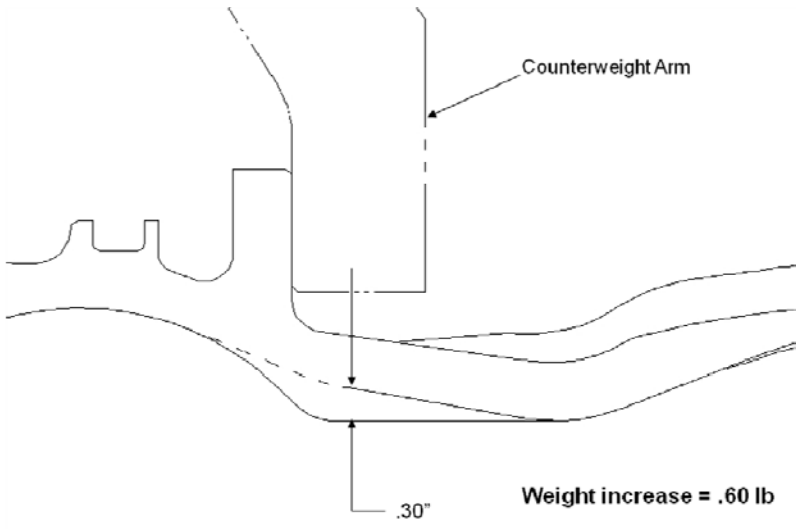


Figure 32. The HS Model 568F Tulip Modification 3

Since tulip modification 1 resulted in the smallest weight increase, it was selected as the best configuration for the tulip redesign. Figure 33 shows the overstress area for tulip modification 1 with point A labeled as the maximum stress location and point B labeled as the edge of the overstress area.

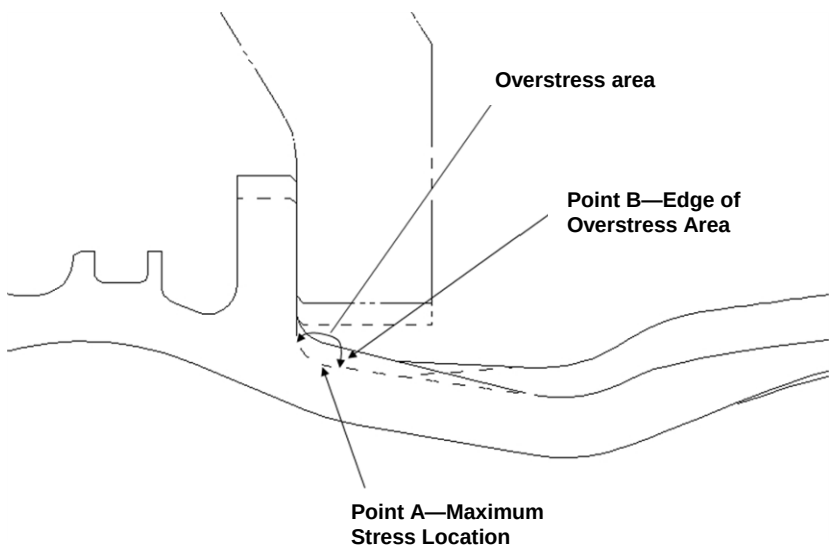


Figure 33. The HS Model 568F Tulip Modification 1—Overstress Area

The stresses at points A and B, obtained using NASTRAN calculations for the baseline configuration, were compared to hand calculations (see equation 6).

$$Stress = K_t \left[ \left( \frac{P}{A} + \frac{Mc}{I} \right)_{steady} \pm \left( \frac{Mc}{I} \right)_{cyclic} \right] \tag{6}$$

where $K_t$ is the stress concentration factor, $P$ is the axial load, $A$ is the cross-sectional area, $M$ is the bending moment, $c$ is the distance from the neutral axis to the point of interest (in this case, the outside radius), and $I$ is the moment of inertia. There was good agreement between the NASTRAN and hand calculation results in the highly stressed fillet radius. Hand calculations were also performed to determine the stress levels in the fillet radius for tulip modification 1. As the normalized Goodman diagram in figure 34 indicates, the hand calculations show that the stresses will be below the newly established limits if tulip modification 1 is applied. The arrows indicate the reduction in stress due to the tulip geometry modifications.

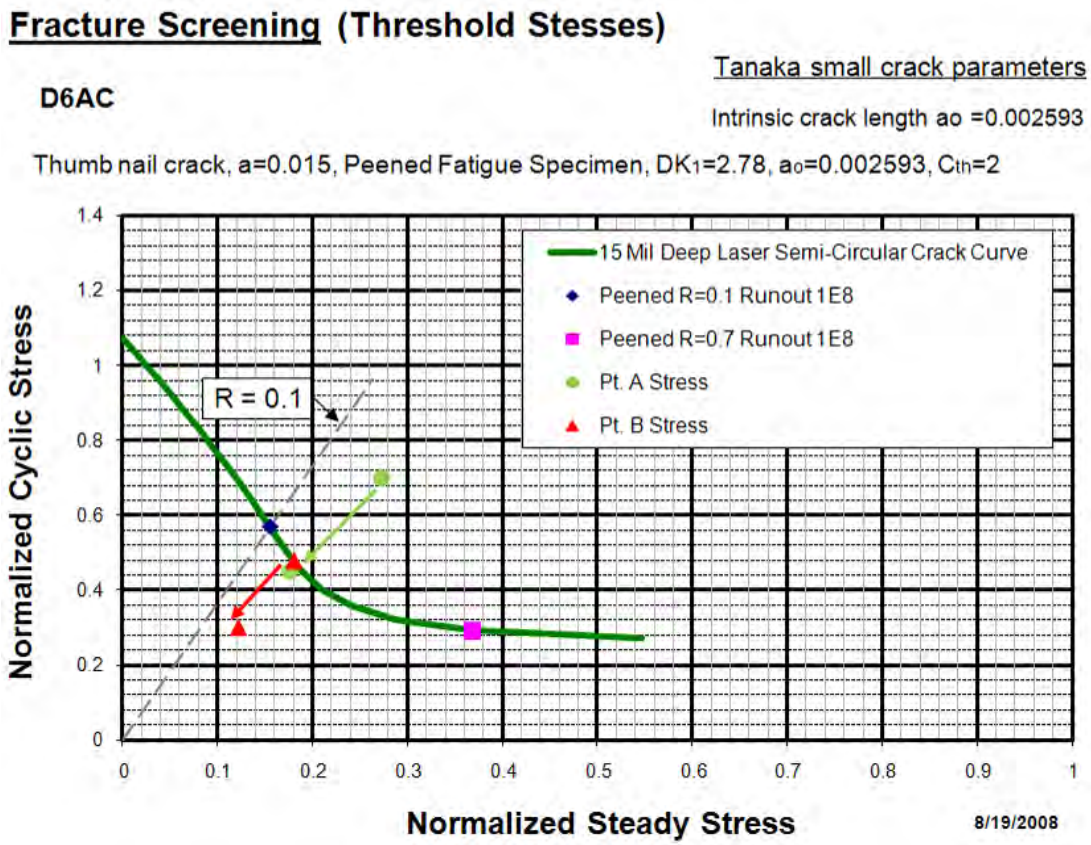


Figure 34. Goodman Diagram for the HS Model 568F Tulip Modification 1

## 3.3 THE HS MODEL 568F HUB MODIFICATION BASED ON CGDT ALLOWABLES.

The FEMs and solid models generated for the safe-life structural design and analysis of the original HS Model 568F hub were available. The models included the hub, dome, shaft, tulip, and two rows of angular contact bearings per arm. The cross-section of the solid model showing these components is provided in figure 35.

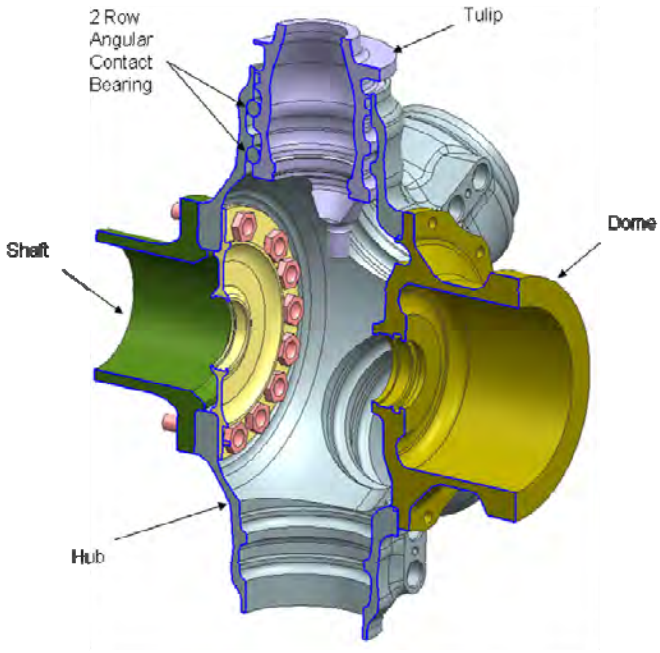


Figure 35. Cut-Away View of the HS Model 568F Hub Geometry

The FEM of the original HS Model 568F hub was created as shown in figure 36. The top half of the hub was modeled fine for stress recovery during postprocessing and the bottom half was modeled coarse to reduce the execution time. The shaft to hub interface was glued together—no bolts or dowels were modeled. The dome-to-hub interface was also glued—no bolts were modeled.

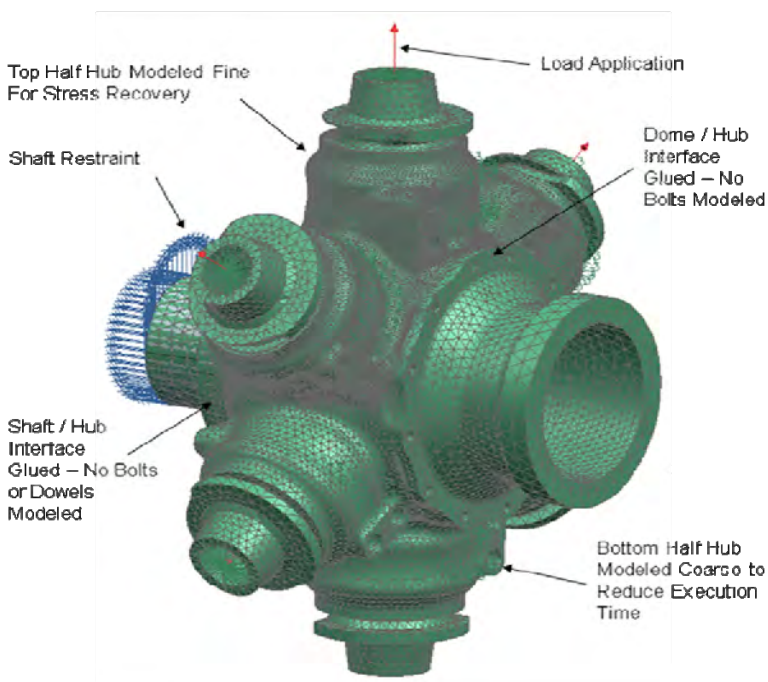


Figure 36. The FEM Construction of the HS Model 568F Hub

The hub model was constrained using a fixed boundary condition at the shaft. The loads were applied at the top of the tulip, and the load transfer at the ball bearing interfaces was simulated. Within the hub, the blade pitch change was restrained by the blade retention pin and dome connection, as shown in figure 37. The bearing load transfer was simulated with nonlinear linkages.

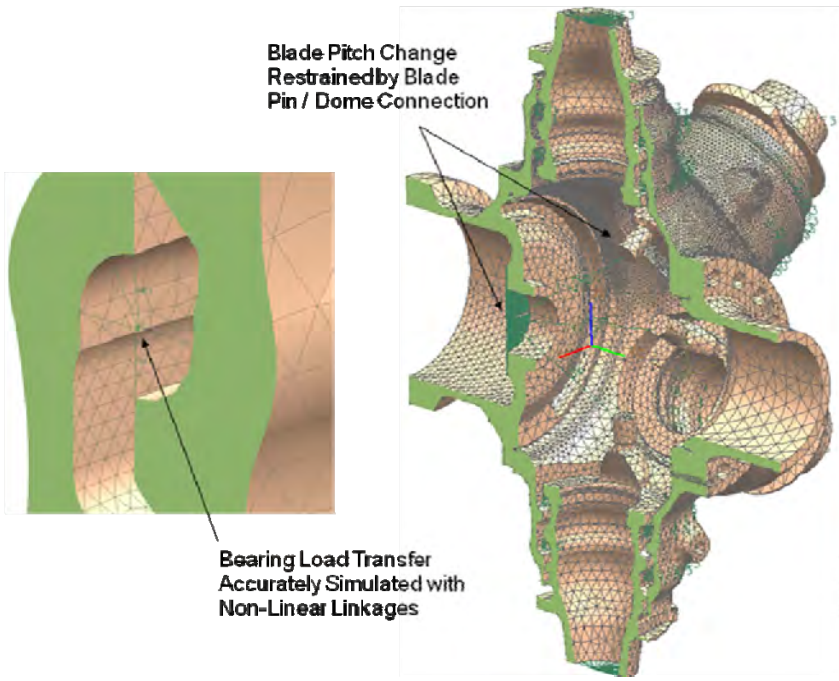


Figure 37. Cut-Away View of the HS Model 568F Hub FEM Construction

The Material Non-Linear Static (NASTRAN SOL 106) model solution was used for the HS Model 568F hub FEA. The load cases representing 1P loads associated with the key operating takeoff climb condition were run. The results from the fine part of the hub model were examined for maximum and minimum stresses, which were converted to the steady and cyclic Von Mises stress reported on the normalized Goodman plot, as shown in figure 38. The tulip allowables curve established for the unpeened D6AC steel with a 0.015-inch-deep crack was used conservatively for the hub as well, even though the hub material hardness is 40-44 HRC compared to the tulip material hardness of 35 HRC. Stresses in four hub regions were above the damage allowables curve: the dome hole, between the arms, the ball-loading hole, and the moment axis fillet.

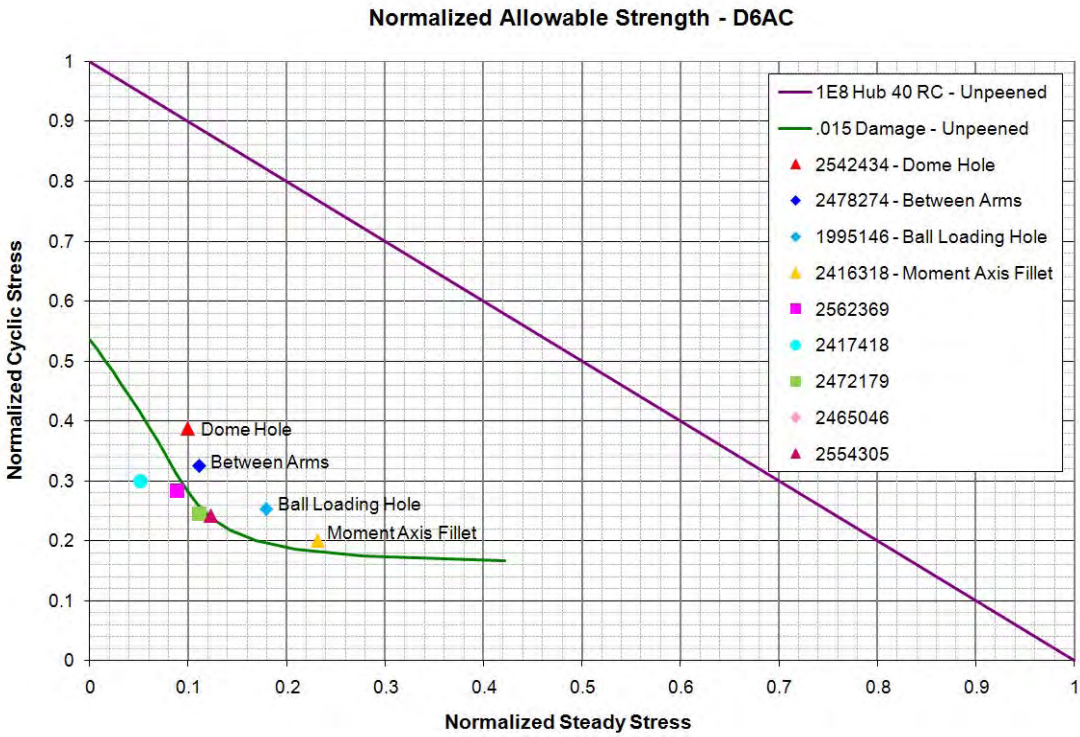


Figure 38. The HS Model 568F Hub FEM Results—Goodman Diagram for Nominal Case

Figures 39-42 show the normalized steady and cyclic stress distributions for the four overstressed hub areas.

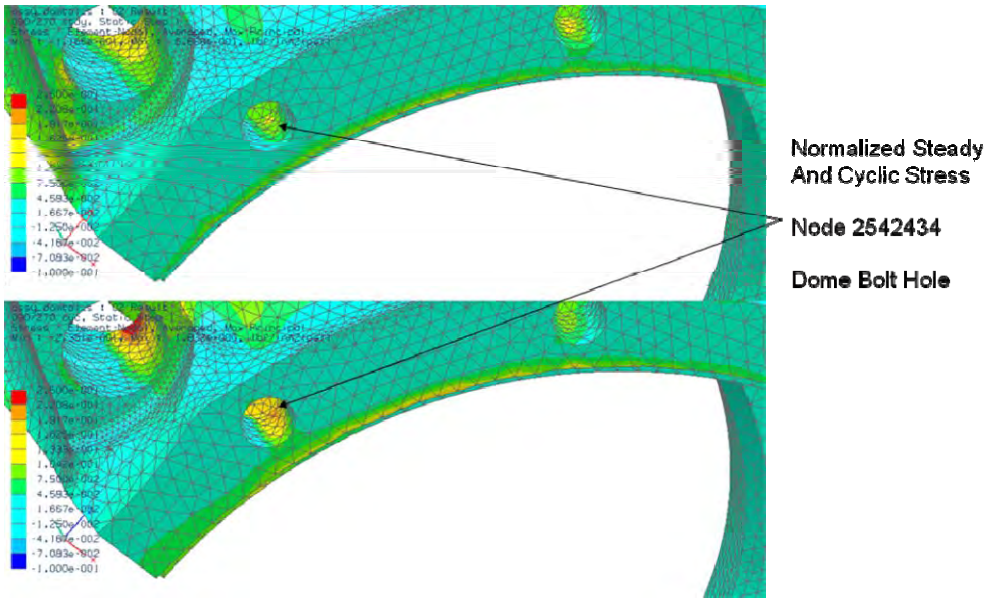


Figure 39. Baseline HS Model 568F Hub FEM Results—Dome Bolt Hole

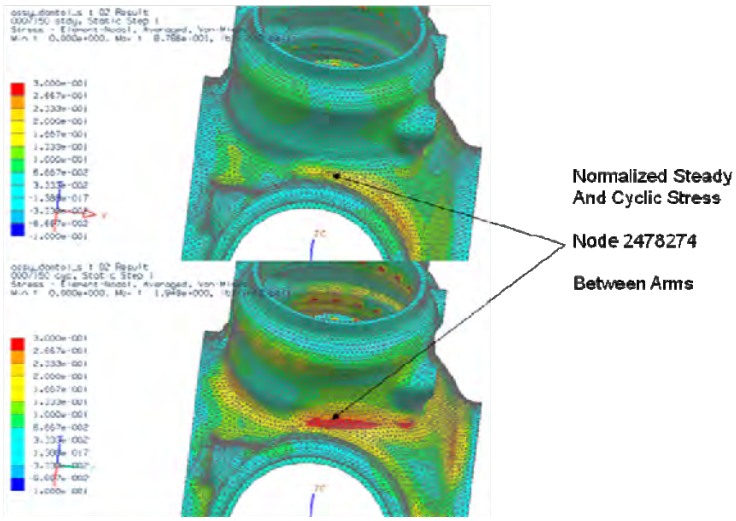


Figure 40. Baseline HS Model 568F Hub FEM Results—Between Arms

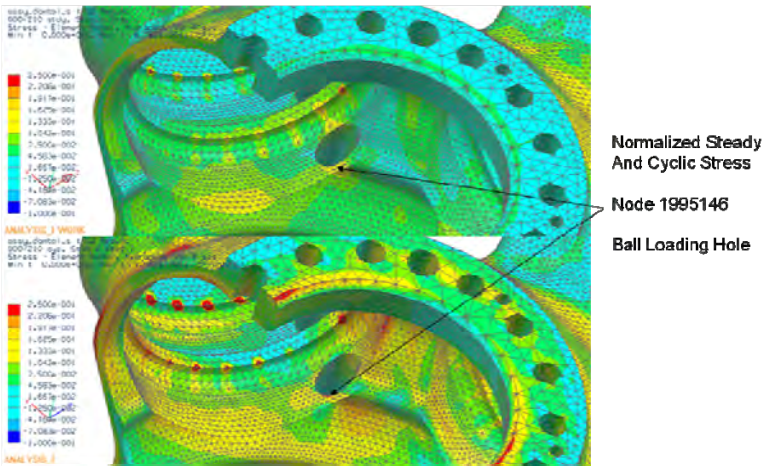


Figure 41. Baseline HS Model 568F Hub FEM Results—Ball-Loading Hole

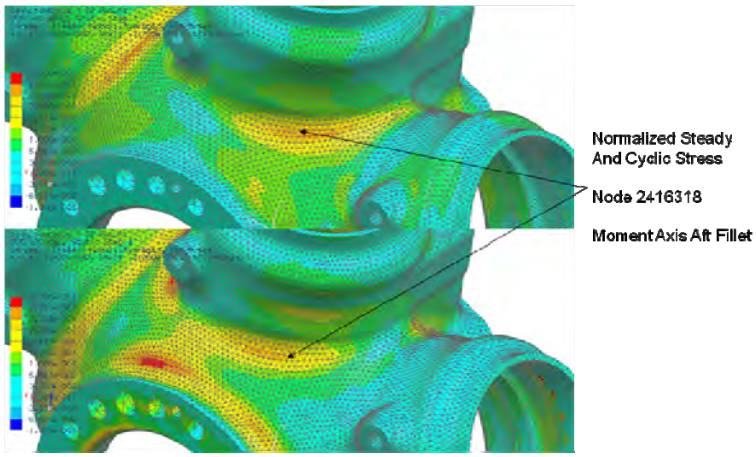


Figure 42. Baseline HS Model 568F Hub FEM Results—Moment Axis Aft Fillet

The HS Model 568F hub geometry was modified in each of the four high-stress areas to produce stresses that were below the new allowable limits on the Goodman diagram. The reduction in stress was analyzed and compared to the geometry changes to develop the final model with all four geometric changes. The increase in weight was calculated. Stresses in the four high-stress areas resulting from the modified hub design were plotted on the Goodman diagram along with the original stresses, as shown in figure 43. The arrows indicate the reduction in stress levels due to the hub geometry modifications.

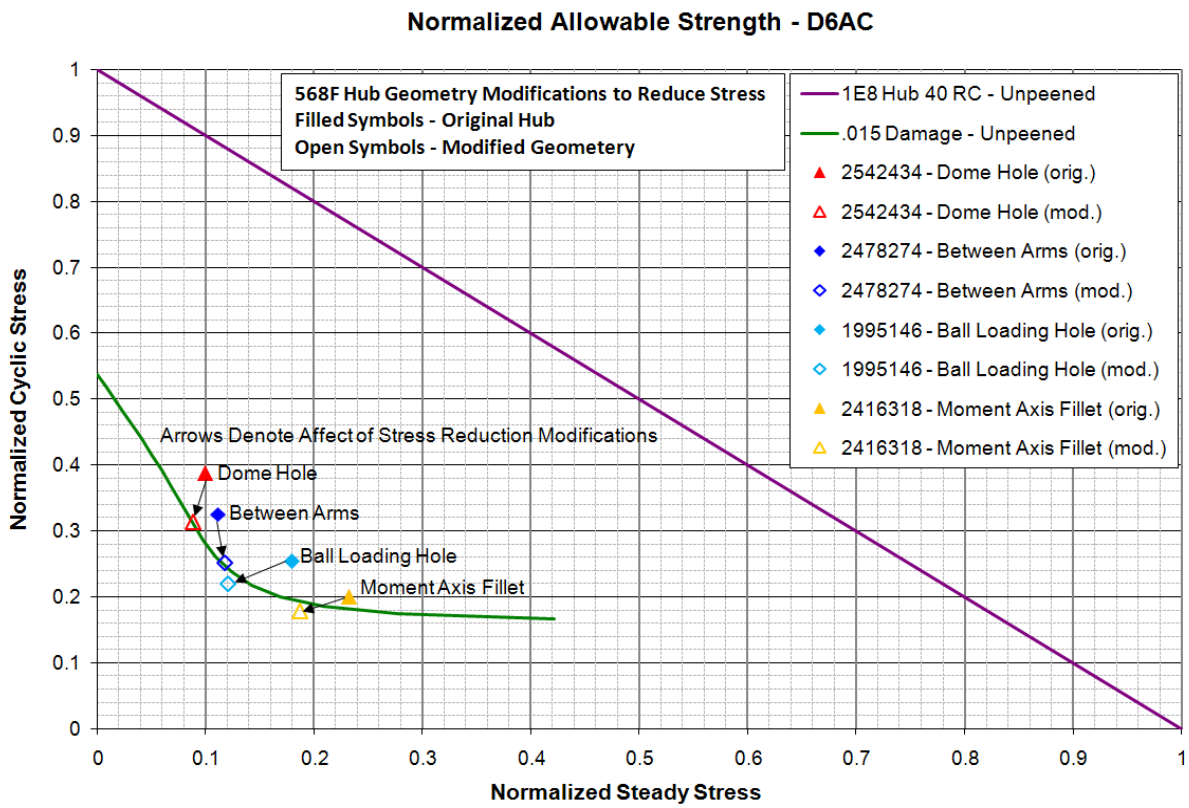


Figure 43. Goodman Diagram for HS Model 568F Modified Hub FEM Results

Figure 2 shows the HS Model 568F hub geometry modifications needed to maintain the stress levels below the newly established Goodman allowables for CGDT.

## 3.4 FRACTURE MECHANICS ANALYSIS OF HS MODEL 568F TULIP SPECTRUM LOADING.

The basis of this portion of the study was to show that the HS Model 568F tulip, which was redesigned to account for a 0.015-inch-radius crack at the high-stress area using only the key operating condition, is also acceptable for the full-spectrum load stress conditions. Figure 44 shows the modified Goodman diagram for peened D6AC with all the spectrum load stresses. The key operating load case is highlighted and is below the DT curve for a 0.015-inch-radius crack.

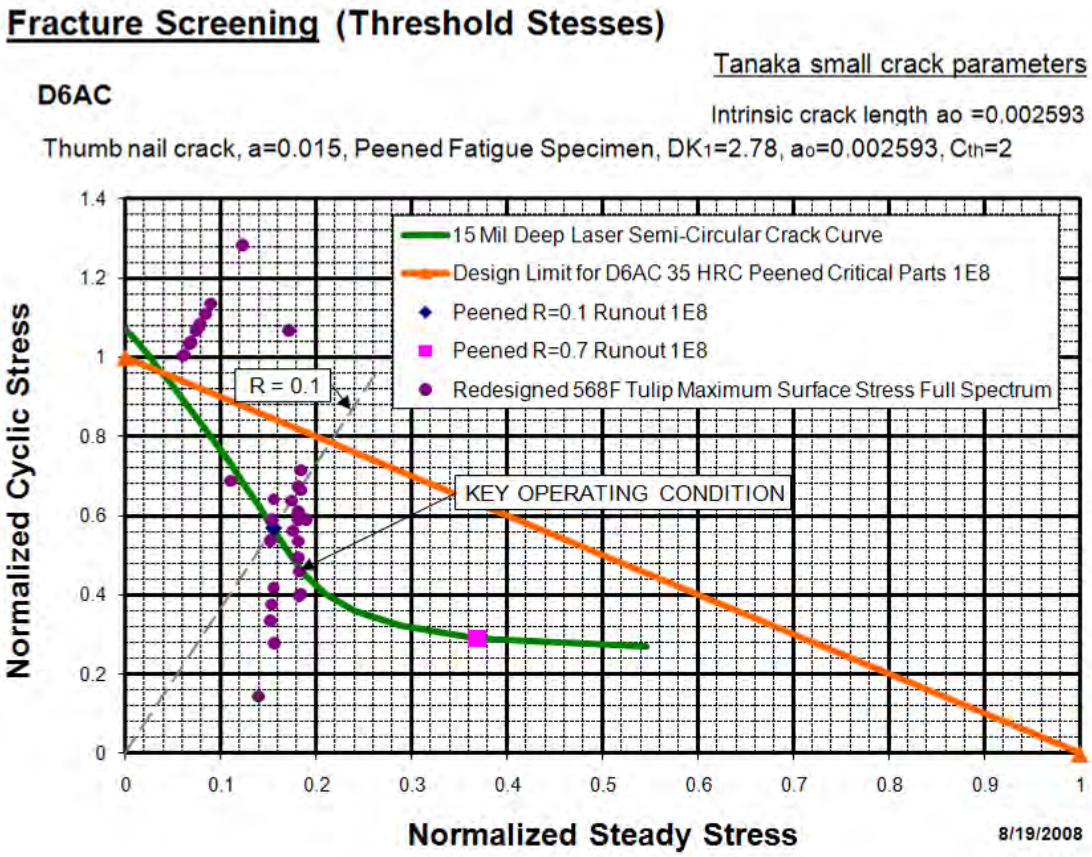


Figure 44. Modified Goodman Diagram for 0.015-Inch-Radius LGCLF for Peened D6AC

The Goodman allowables for CGDT shown in figure 44 were established for $10^8$ cycles. The stress values exceeding this limit correspond to a lower cycle loading with more conservative Goodman allowables.

The normalized stress distribution through the tulip wall thickness for the spectrum loads, normalized to the total wall thickness, is shown in figure 45. The residual stresses from the shot peening were also normalized to the total thickness, as shown in figure 46. These distributions were input to the fracture mechanics model, NASGRO SC17, as shown in figure 47. The material properties for the fracture model are provided in appendix A. The model was run with optimized point spacing, noninteraction, and $C_{th} = 0$ throughout.

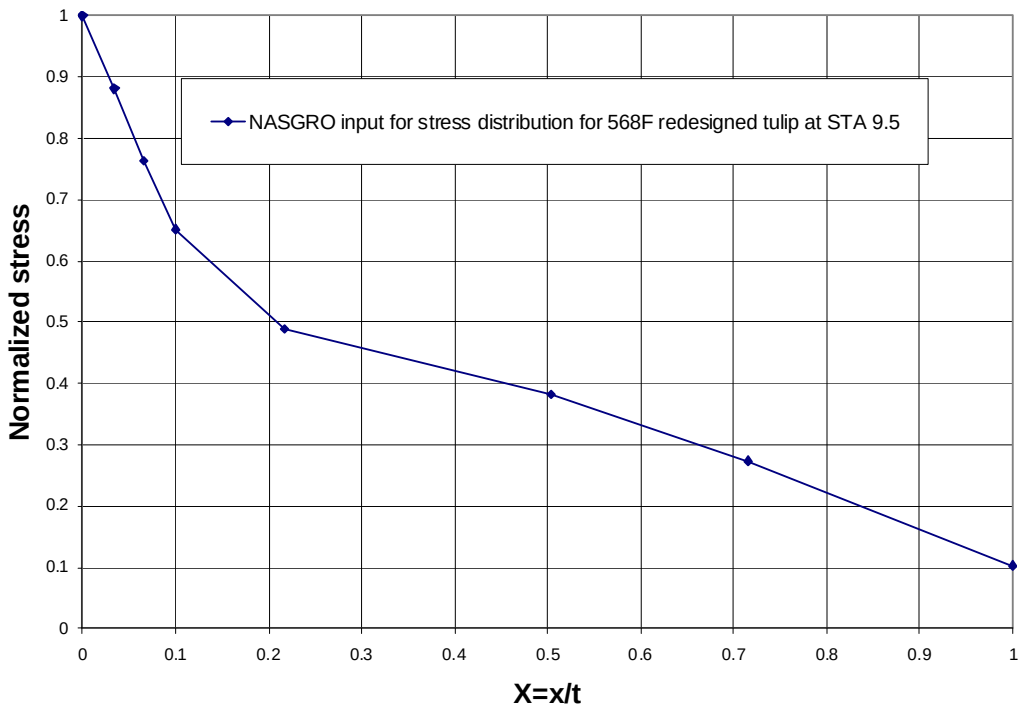


Figure 45. Normalized Stress Distribution Through the Thickness for Applied Loads

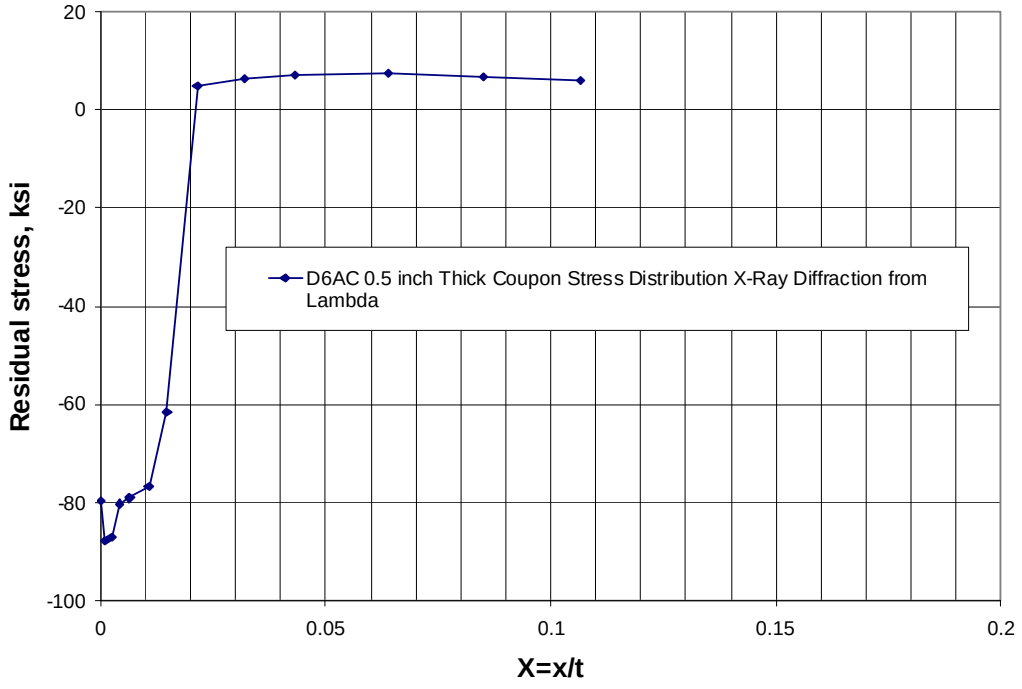


Figure 46. Stress Distribution Through the Thickness for Residual Stress From Peening

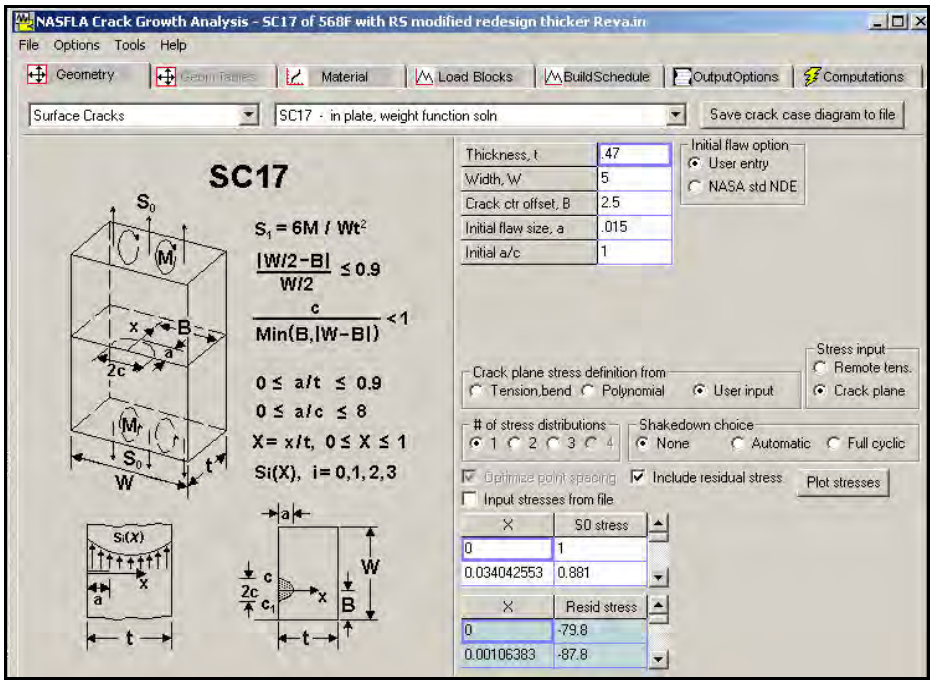


Figure 47. Screen Shot of the Fracture Mechanics Model

Figure 48 shows the results for the model verification under constant-amplitude loading. The results are for crack growth of 0.010 inch ($\Delta a$ = 0.010). These are tunneling cracks because there is no crack propagation at the surface ($\Delta c$ = 0) due to the high compressive residual stresses from the peening.

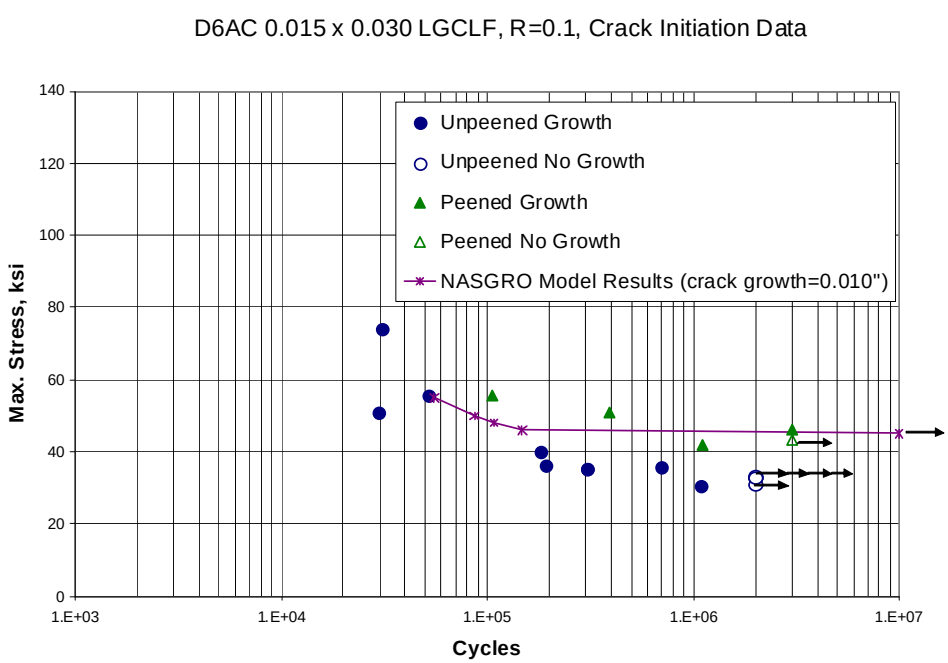


Figure 48. Verification of Fracture Model With the Constant-Amplitude Load Tests

The fracture mechanics model compares well to the actual test data, where the specimens were cycled until crack initiation was found ($\Delta a$ measured ranged from 0.004-0.010 inch). The runout data had no crack initiation and that compared well to the load case of 45 ksi, which was just below the crack initiation threshold. Hence, the model was deemed acceptable to do the flight spectrum analysis.

The results of the HS Model 568F redesigned tulip flight spectrum analysis are shown in figure 49.

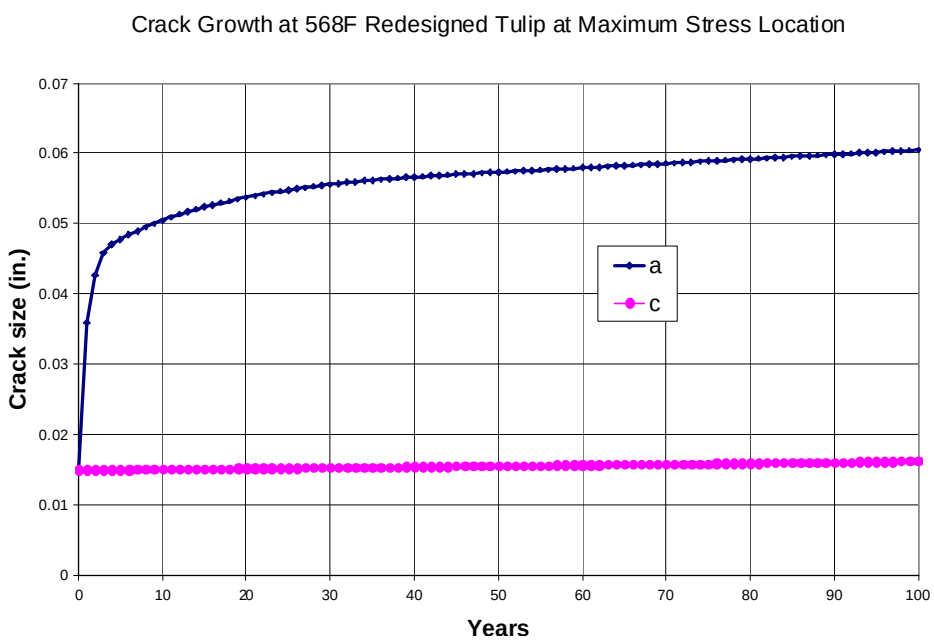


Figure 49. Crack Size vs Years for HS Model 568F Tulip Spectrum Loading

Figure 49 shows how the crack depth (a) and crack half length (c) increases with time. As figure 49 indicates, the crack tunnels very quickly, initially, and then begins a slow rate of propagation out to 100 years. The normal life of the propeller is about 30 years, so the calculation supports the desired results.

## 4. INSPECTION OF MICROSURFACE DEFECTS.

### 4.1 NONDESTRUCTIVE INSPECTION OVERVIEW.

While DT methodology has been extensively and successfully used in fixed-wing aircraft structures and is starting to be used for dynamic components in rotorcraft, propeller systems have been exclusively designed and certified using the safe-life approach. This effort also seeks to generate critical data and improve propeller design methodology to aid the rotorcraft and propeller industries. The program consists of the following elements: (1) generation of a crack growth and fatigue properties database, (2) characterization of mechanical, environmental, and manufacturing threats, (3) propeller design using the DT approach, (4) fracture mechanics and crack growth analysis, and (5) nondestructive inspection (NDI) techniques development. This

section focuses on the NDI initiative conducted by the FAA Airworthiness Assurance NDI Validation Center (AANC), which is operated by Sandia National Laboratories. The DT approach recognizes the impossibility of establishing complete structural redundancy—the fail-safe design premise—and places greater emphasis on inspection to ensure safety and reliability. The regime in which propeller NDI must work is significantly different than for structures on fixed-wing aircraft because a large number of load cycles are generated in a short time. Hence, smaller flaws may need to be detected to allow for the implementation of DT approaches. This NDI effort focused on producing inspection methods to reliably detect uniquely-shaped cracks, or crack nucleation sites, that are as small as 0.015″ deep by 0.025″ wide. The load spectrum and operating environment for propellers can produce these cracks so that they do not pierce the inspection surface (burrowing cracks). Realistic test specimens were produced using laser-notching methods and subsequent NDI tests were performed to calculate probability of detection (POD) and false call levels in the most promising techniques. Customized procedures and hardware were evolved to optimize NDI sensitivity. The overall NDI effort addressed the affect of all inspection impediments on performance including: geometry, coatings, accessibility, depth of penetration, effects of shot-peening, equipment deployment, and other human factors issues.

## 4.2 PROPELLER DT ANALYSIS AND NDI EVALUATION.

### 4.2.1 Program Goals and Tasks.

As previously stated, this program acquired fracture mechanics data that were used to determine the feasibility, validity, and application of DT analysis (DTA) for existing and new propeller designs. Overall, this study was conducted to

- support the feasibility to implement DT into FAA propeller certification requirements.
- determine the effects of changing from safe-life (flight hours or fatigue cycles) to the DTA approach.
- ensure proper monitoring of propeller and hub parts after they are in service.

NASA-JSC, in conjunction with HS and the AANC at Sandia National Laboratories, completed a comprehensive crack growth and fatigue property assessment of the materials used in propeller designs. The test series acquired fracture mechanics data, such as fatigue crack growth rates and threshold values for shot-peened specimens, and surface crack condition specimens made from 7075-T73 and D6AC propeller alloys. Crack growth rates were characterized from threshold to fracture for a range of stress ratio R-values. This work included the development of analysis methods for predicting fatigue crack initiation and growth rates for cracks initiating from different size corrosion pits. The spectrum load test results were then compared with NASGRO analysis results for both interaction and crack retardation model options. This work allowed the team to understand the crack growth behavior of the most frequent types of damage, such as small cracks, scratches, tool marks, and corrosion pitting under conditions relevant to propeller systems.

HS used this data to carry out the case study, reported here, to determine the viability of applying crack growth DT to new propeller designs. This portion of the project studied crack growth behavior for the frequent types of propeller damage such as small cracks, scratches, tool marks, and corrosion pitting. Specific tasks assessed the effect of using classic CGDT as the basis for propeller structural design especially with respect to the weight of the propeller and associated components. The structural design of the HS Model 568F propeller, a six-bladed assembly shown in figure 50, was modified as the basis for this assessment.

Figure 50. The HS Model 568F Propeller With Six Composite Blades

This section discusses the complementary AANC task that developed nondestructive test techniques to reliably detect cracks and corrosion that could occur based on the propeller load spectrum and operating environment. As the aviation industry expands and refines its adoption of the DT philosophy, the appropriate application of NDI methods is essential to ensuring the safe operation of critical components. The DT approach recognizes the impossibility of establishing complete structural redundancy—the fail-safe design premise—and places greater emphasis on inspection to ensure safety and reliability. The regime in which propeller NDI must work is significantly different than for structures on fixed-wing aircraft because a large number of load cycles are generated in a short time. Hence, smaller flaws must be detected to allow for the implementation of DT approaches. The reliability of NDI concepts were examined for their potential to be applied to the components, materials, and flaws that occur in propellers [10 and 11]. Specific consideration was given to evaluating

- current manufacturing technologies and practices.
- field deployment capabilities.
- POD in the equivalent initial flaw size (EIFS) and equivalent initial crack size regimes.
- the ability to detect fretting, corrosion, and other noncrack damage.

4.2.2 Overall FAA Propeller DT Road Map.

The FAA is assessing the feasibility to implement DT requirements for propeller certification. While DT methodology has been extensively and successfully used in fixed-wing aircraft structures and is starting to be used for dynamic components in rotorcraft, propeller systems

have been exclusively designed and certified using the safe-life approach. The FAA is supporting research and development efforts to make DT technology more applicable for use on propeller systems and to make the improved technology and data resulting from this work available to the rotorcraft and propeller industries and to the public at large.

4.2.3 Survey of Causes and Damage Leading to Cracks in Propeller Blades and Hubs.

The Committee on Propeller Damage Tolerance (CPDT) was formed under the auspices of the General Aviation Manufacturers Association, with a mission to develop approaches to enhance propeller DT. Most propeller components are designed using long-established safe-life methods to preclude fatigue cracking. Using common safe-life design methods, major propeller components, which experience high-cycle fatigue loads, have been designed to maintain stresses comfortably below the typical fatigue strength capability of the material. These robust design methods, along with consistent manufacturing methods, diligent maintenance, and field support have led to the overall good safety record of the industry and a high degree of tolerance to the threats encountered by propeller systems. While development of fatigue cracks are relatively rare, they are often discovered during maintenance inspections and do not result in propeller incidents.

To characterize the threats to propeller systems, the CPDT conducted a survey to determine the major causes of cracking in propeller systems. This effort focused on determining the type and frequency of damage that has led to cracking in propeller systems in the past. An additional objective was that the survey may aid development of operational procedures to reduce or eliminate some threats. The survey was limited to incidents of cracking in blades and hubs occurring in the last 20 years. Each manufacturer reported the percentage of cracking events according to the categories. The categories are further grouped into the major categories of Specific Physical Causes (corrosion, fretting, impact, lightning strike) Damage, Maintenance-Related Causes (improper maintenance, lack of maintenance), Operational-Related Causes (improper use), and Manufacturing-Related Causes (raw material defect, special processes, machining processes). The Unknown category captured cracking incidents for which the cause was never determined or was unreported.

Figure 51 shows the leading proximate causes of crack formation in propellers. The survey showed that for general aviation products, improper maintenance was the leading factor in fatigue crack development. In both general aviation and commercial and transport aviation, corrosion is the most frequent physical damage or proximate cause leading to crack formation. Note: Although fretting was most frequent for commercial and transportation aviation, it was excluded when the occurrences were identified as a design issue on a specific installation that was resolved. The CPDT identified several major elements needed to enable the industry to enhance the tolerance to threat from corrosion. The key elements include (1) developing an understanding of the corrosion process and resultant cracking on fatigue life, (2) developing inspection methods for corrosion and cracks, and (3) improving maintenance practices for corrosion sensitive parts. Therefore, from this survey, it can be inferred that the addition of new NDI during propeller maintenance could be effective in reducing the overall incidence of cracking in propeller systems.

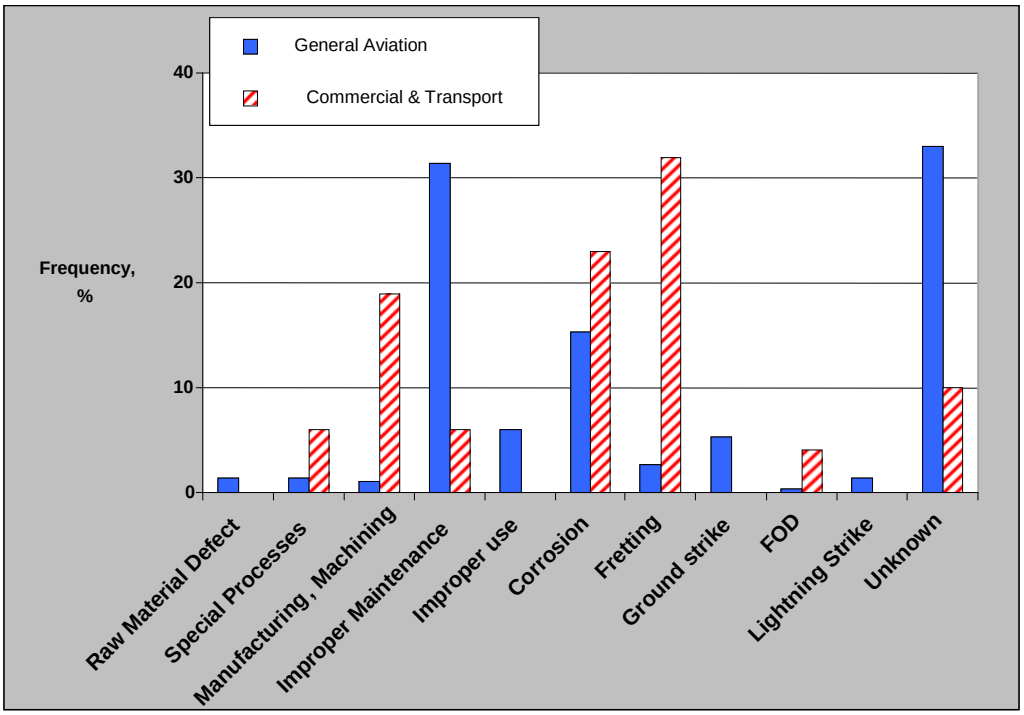


FOD = Foreign object debris

Figure 51. Leading Proximate Causes of Crack Formation in Propellers

## 4.3 DESCRIPTION OF NDI ACTIVITY AND METHODS.

As the aviation industry expands and refines its adoption of the DT philosophy, the appropriate application of NDI methods is essential to ensuring the safe operation of critical components. The DT approach places greater emphasis on inspection to ensure safety and reliability. As per the CPDT, NDI methods are needed to reliably detect small levels of corrosion (pitting) and related cracking in propellers. Methods are needed that will allow detection of hard-to-inspect areas (limited accessibility) and corrosion damage that is hidden by adjacent structures or by paint.

The HS Model 568F propeller was selected for the DT redesign because the data for this propeller model are well documented in terms of its initial manufacturing flaws and in-service records of both mechanical and corrosion damage. The damage-tolerant criteria were based on maintaining ground-air-ground stress levels below typical threshold values. Elements of the material testing used to support the HS Model 568F redesign process are shown in figure 52. Crack onset and growth in peened and unpeened fatigue specimens were quantified for different crack nucleation sites (corresponding to corrosion pits). This information was critical to the NDI effort as it determined the flaw detection goals for the inspection methods. These values were also used to produce a statistical array of specimens with engineered flaws for proper experimental control. An EIFA to a 0.015″ deep, 0.030″ long semicircular crack was assumed to represent initial manufacturing flaws, in-service mechanical damage, and in-service corrosion damage. The NDI effort pursued reliable flaw detection for the size (0.020″ to 0.030″) and type of damage that is expected for the propeller load spectrum and operating environment.

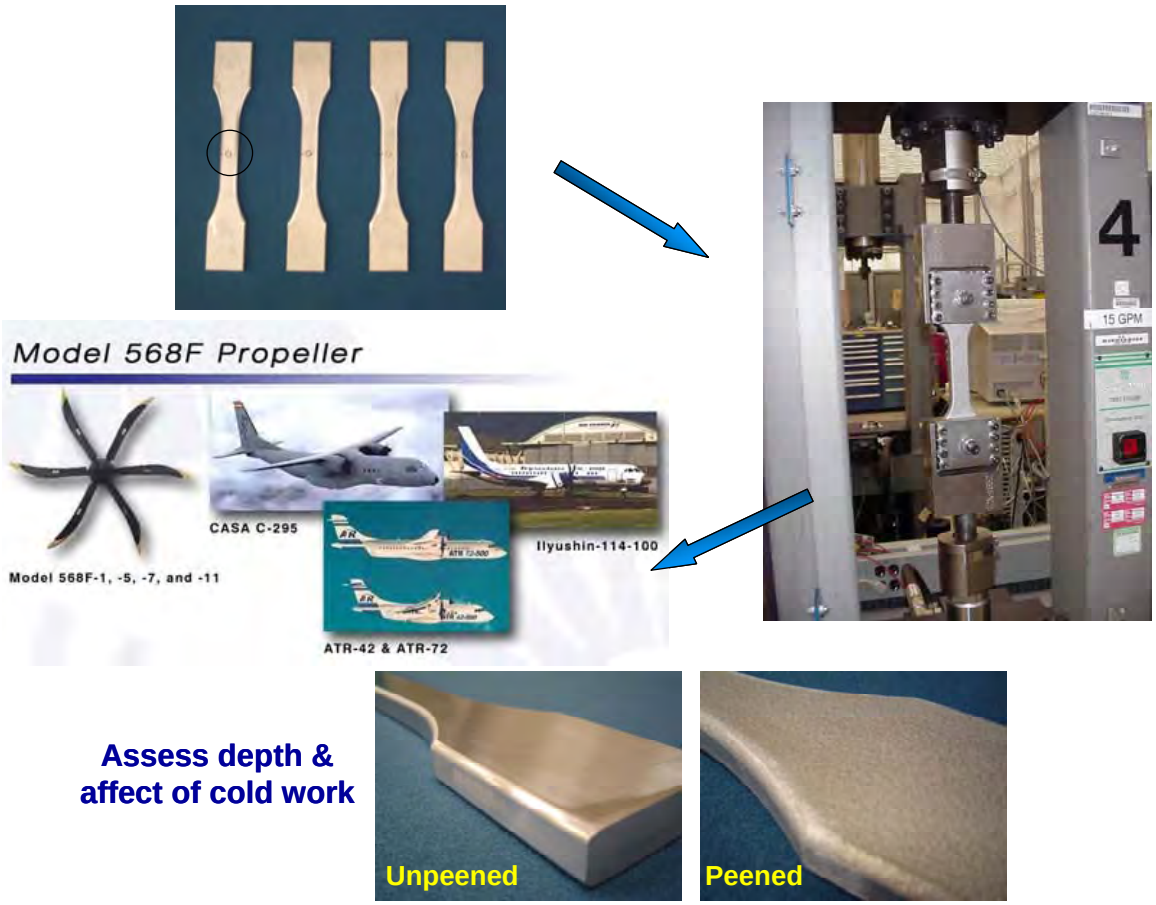





Figure 52. The HS Model 568F Propeller Redesign Process Using Fatigue Specimens to Produce Fracture Properties of D6AC Propeller Material

Extensive tests determined that the best way to produce realistic cracks—or more accurately, small notches that act as crack nucleation sites—is to use a process called LGCLF. This process uses a laser to produce crack-like features in metals that possess the notch geometry and macroscale sharpness of fatigue cracks. Laser application variables, such as traverse rate, pulse frequency, length of travel, and power, can be adjusted with each pass to mill away the desired shape. Parameter sets were established to produce semicircular cracks with dimensions in the range of 0.013″ deep by 0.026″ long, such as those shown in figure 53. Figures 53 and 54 also show the expected elliptical crack growth and the ability to identify crack threshold stemming from the laser notches, which simulate pits in the material (crack nucleation).

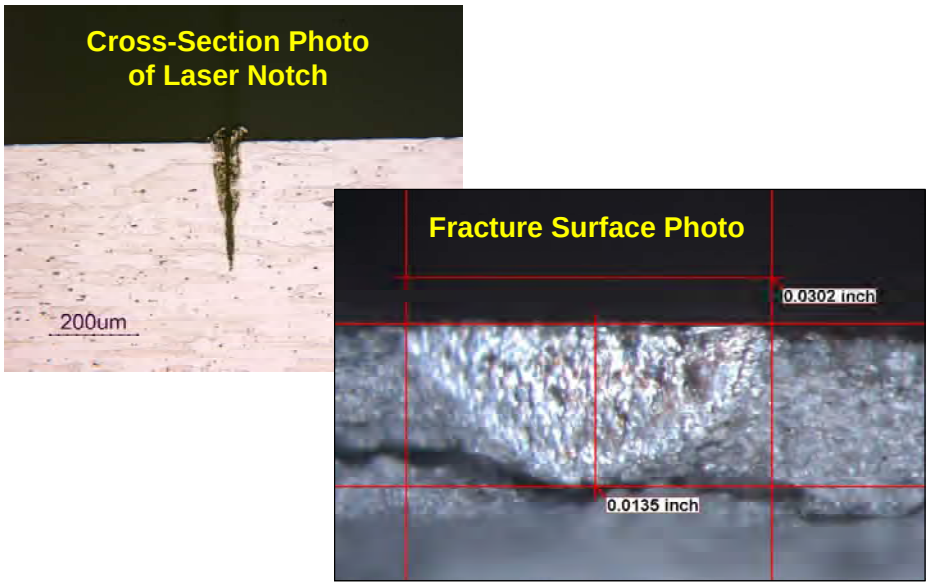


(a)

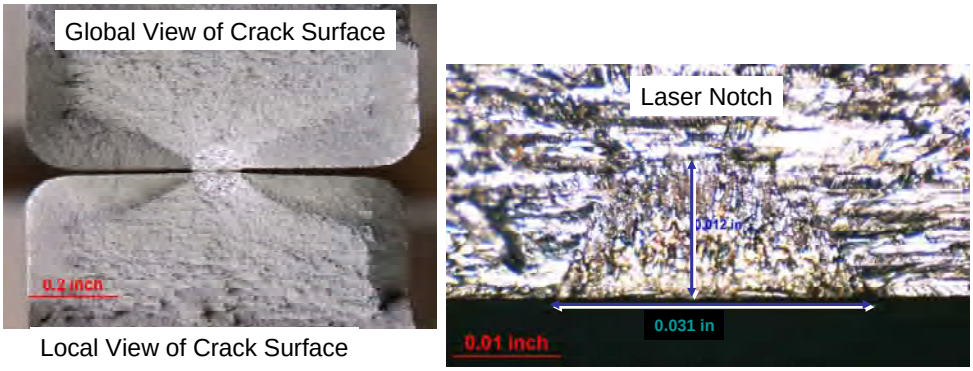


(b)

Figure 53. Photographs of (a) the Laser Notch Used to Simulate Crack Notches in Metals and (b) Subsequent Crack Growth Emanating From Initial Laser Notch

Figure 54. Elliptical Crack Growth in Fatigue Specimen With Laser Notch

When producing the NDI test specimens, the laser notch plates were subjected to an additional machining process, such as the one shown in figure 55. First, a series of laser passes were completed to produce an array of cracks containing various depths and lengths, as shown in figure 55①. Next, a surface milling process, as shown in figure 55②, was performed to remove any surface burrs and a slight amount of surface material. During this latter machining process, the top of the notches were smeared so that these ultrasmall cracks were not visually detectable. Figure 56 shows examples of the completed NDI test specimens.

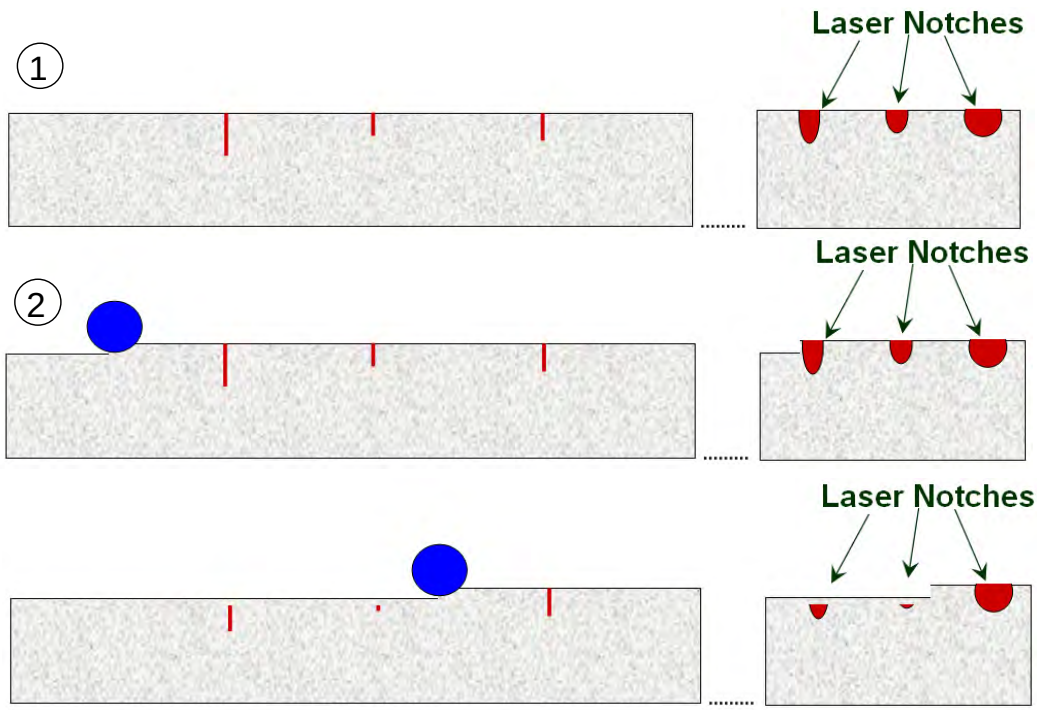


Figure 55. Generation of NDI Test Specimens Using a Laser Notch Process Followed by Carefully Controlled Surface Machining

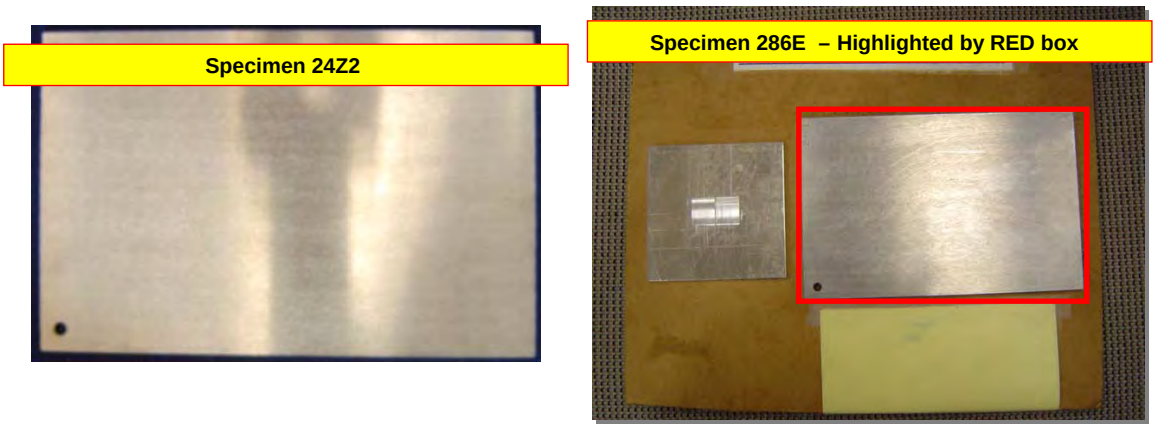


Figure 56. Aluminum Test Specimens (3.5″ wide by 6″ high by 0.125″ thick) Produced Using Machining Process That Removes Surface Indications of Burrowing Crack

A variation on this process was used to produce an additional set of NDI test specimens containing actual fatigue cracks. Figure 57 shows the process that was used to produce these specimens. First, a laser notch was placed in the center of the plate, which contained a thicker raised region (figure 57①). Next, the plate was cyclically loaded to propagate a fatigue crack stemming from the initial notch (figure 57②). Finally, a surface milling process, similar to the one shown in figure 55②, was performed to remove the raised region of the plate along with the crack starter notch (figure 57③). Again, the fatigue cracks that remained in the plate were not visibly detectable. This process was used to create cracks that were on the order of 0.014″ to 0.080″ long by 0.006″ to 0.035″ deep.

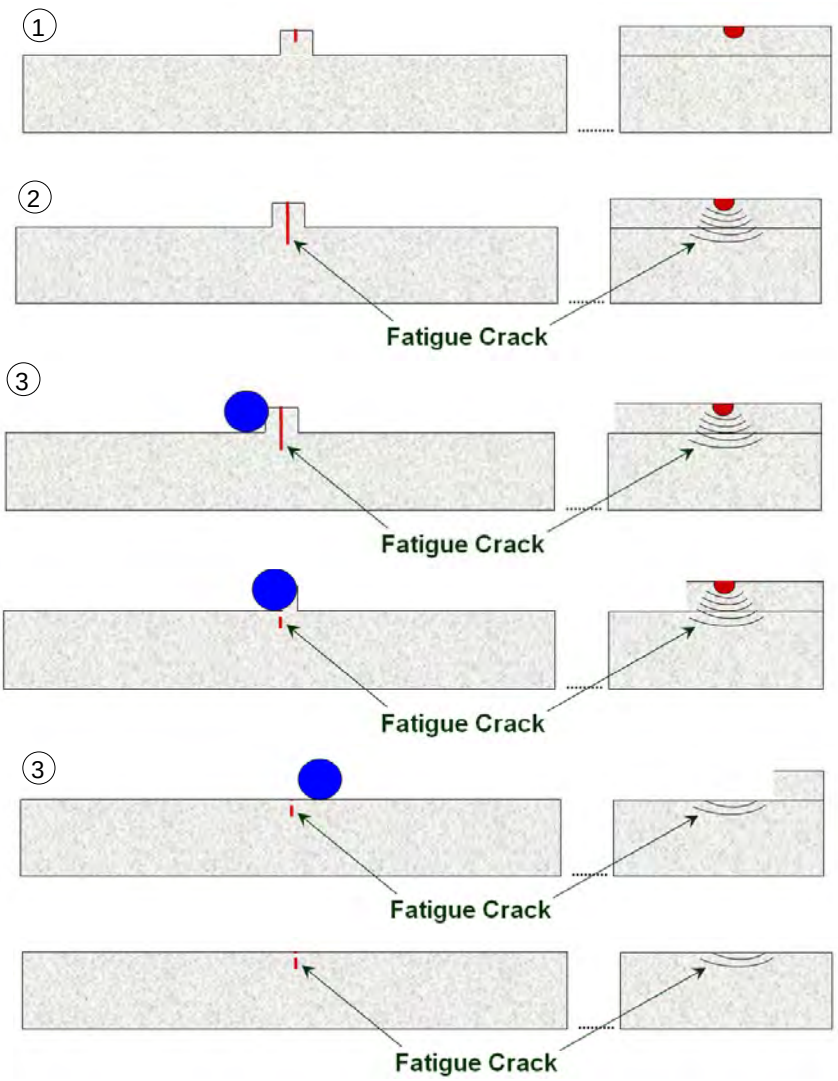


Figure 57. Generation of NDI Test Specimens Using a Laser Notch to Help Initiate a Fatigue Crack Followed by Carefully Controlled Surface Machining

It is clear that the NDI activity used a series of different specimens to evaluate the detection of ultrasmall surface cracks. Dogbone specimens with laser notches were used for the fracture property tests, but were also used for initial NDI assessments that included both eddy current

(EC) and ultrasonic (UT) methods. This set contained specimens of various thicknesses, 7075-T73 and DC6A propeller alloy materials, and peened and unpeened surfaces. All test specimens were used to determine POD and false-call levels, as well as to assess the sensitivity, resolution, and repeatability of each NDI technique. Finally, the array of tests was used to evaluate equipment deployment, inspection processes, and human factors issues affecting flaw detection performance.

4.3.1 Ultrasonic NDI Method.

UT inspection is a nondestructive method in which beams of high-frequency sound waves are introduced into materials for the detection of surface and subsurface flaws in the material. The sound waves, normally at frequencies between 0.1 and 25 MHz, travel through the material with some attendant loss of energy (attenuation) and are reflected at interfaces. The reflected beam is displayed and then analyzed to define the presence and location of flaws. The degree of reflection depends largely on the physical state of the materials forming the interface. Cracks, delaminations, shrinkage cavities, pores, disbonds, and other discontinuities that produce reflective interfaces can be detected. Complete reflection, partial reflection, scattering, or other detectable effect on the UT waves can be used as the basis of flaw detection. In addition to wave reflection, other variations in the wave that can be monitored include time of transit through the test piece, attenuation, and features of the spectral response.

The principal advantages of UT inspection, compared to other NDI techniques, include the following:

- Superior penetrating power for detection of deep flaws
- High sensitivity, permitting the detection of extremely small flaws
- Accuracy in determining size and position of flaws
- Only one surface needs to be accessible
- Portability

4.3.2 Ultrasonic Pitch-Catch Pulse-Echo Inspections.

In UT pitch-catch pulse-echo inspections, short bursts of UT energy are interjected into a test piece at regular intervals. In most pulse-echo systems, a single transducer alternately acts as the sending and receiving transducer. The mechanical vibration (ultrasound) is introduced into a test piece through a couplant and travels by wave motion through the test piece at the velocity of sound, which depends on the material. If the pulses encounter a reflecting surface, some or all energy is reflected and monitored by the transducer. The reflected beam, or echo, can be created by any normal (e.g., in multilayered structures) or abnormal (flaw) interface. Figure 58 shows a schematic of the pulse-echo technique and the interaction of UT waves with various interfaces within a structure. In some cases, it is advantageous to use separate sending and receiving transducers for pulse-echo inspection. The term pitch-catch is often used in connection with separate sending and receiving transducers.

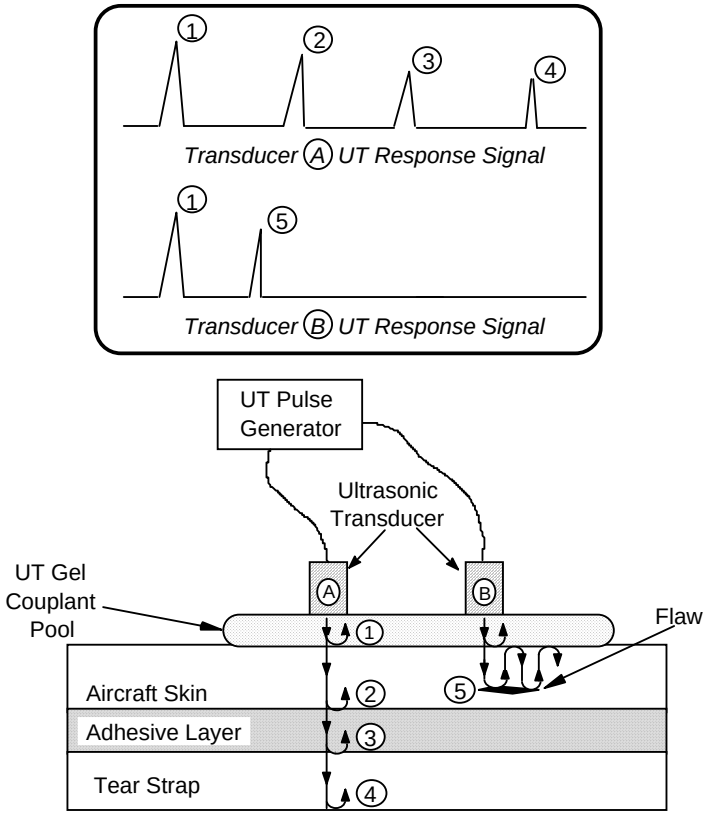


Figure 58. Pulse-Echo UT Inspection and Reflection of UT Waves at Various Interfaces

4.3.3 A-Scan Mode.

A-Scan signals represent the response of the stress waves or other interrogating waves in features, such as amplitude and time, as they travel through a material. As the waves interact with defects or flaw interfaces within the solid and portions of the pulse's energy are reflected back to the transducer, the flaws are detected, amplified, and displayed on an analog screen. The interaction of the UT waves with defects and the resulting data, such as time versus amplitude signal produced on the monitor, depends on the wave mode, its frequency, and the material properties of the structure. Flaw size can be estimated by comparing the amplitude of a discontinuity signal with a signal from a discontinuity of known size and shape. Flaw location (depth) is determined from the position of the flaw echo along a calibrated time base. Most instruments with an A-scan display allow the signal to be displayed in its natural radio frequency (RF) form, as a fully rectified RF signal, or as either the positive or negative half of the RF signal.

4.3.4 C-Scan Mode.

Scanners are used to generate two-dimensional C-scan images from inspection data. A basic C-scan system moves the UT transducer over the surface of the test piece using a search pattern of closely spaced parallel lines. A mechanical linkage connects the scanning unit to X- and Y-axes position indicators, which feed position data to the computer. The echo signal is recorded, correlated to its X-Y position on the test piece, and a color-coded image is produced

from the relative characteristics of the sum total of signals received. Typically, a data collection gate is established on the A-scan signal, and the amplitude or the time-of-flight of the signal is recorded at regular intervals as the transducer is scanned over the test piece. The C-scan presentation provides an image that indicates the reflection and scatter of the sound within and on the surfaces of the test piece and their features relative to the gate settings.

4.3.5 Eddy-Current NDI Method.

EC inspection uses the principles of electromagnetic induction to identify or differentiate structural conditions in conductive metals. The presence of a crack is indicated by changes in the flow of ECs in the structure. EC signals are physically monitored using impedance plane plots, which show the reactive and resistive components of a coil as functions of frequency, conductivity, or permeability. When EC inspections are performed, an electrically conductive material is exposed to an alternating magnetic field that is generated by a coil of wire carrying an alternating current. As a result, ECs are induced on and below the surface of the material, as shown in figure 59. These ECs, in turn, generate their own magnetic field, which opposes the magnetic field of the test coil. Cracks or thickness changes in the structure being inspected influence the flow of ECs and change the impedance of the test coil accordingly. EC instruments record these impedance changes and display them in impedance plane plots to aid the flaw detection process.

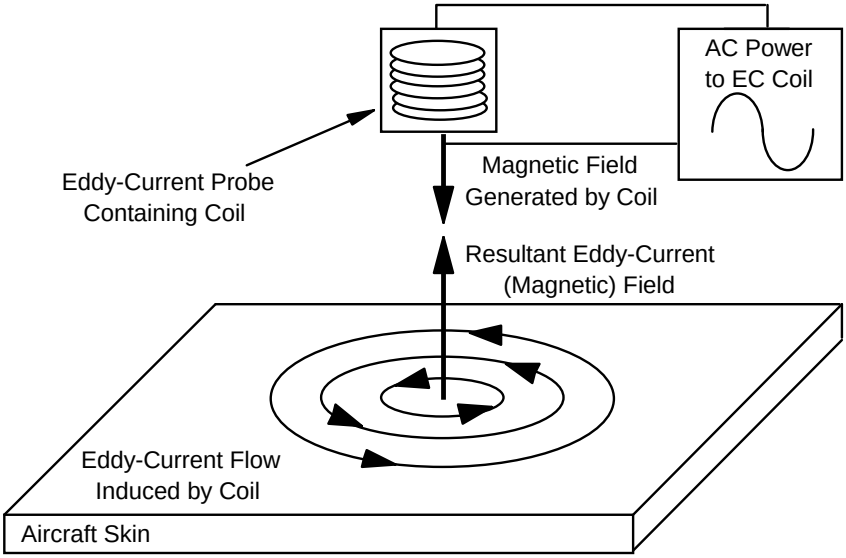


Figure 59. Induction of ECs in Conductive Materials

The depth of penetration of ECs is inversely proportional to the product of magnetic permeability, electrical conductivity, and frequency of the inducing currents. Therefore, EC tests are most sensitive to discontinuities on the surface next to the coil, which makes them very effective for detecting fatigue cracks in the near surface. High-frequency EC is generally considered 100 KHz and above and is used to detect near-surface flaws. Low-frequency EC is in the 100-Hz to 10-kHz range and is used to penetrate deeper to detect flaws in underlying structure. As the structure to be penetrated gets thicker, a lower EC operating frequency is

required to reach the desired depth. However, the detectable flaw size usually becomes larger as the frequency is lowered. Figure 60 shows an example of an impedance plane display showing phase and amplitudes of EC signals generated by cracks of varying depths.

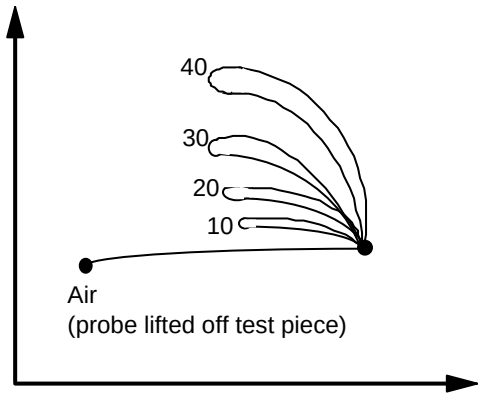


Figure 60. Impedance Plane Display Showing Signal Traces for Surface Cracks of Different Depths (shown in 1/1000″)

4.4 RESULTS OF NDI FOR CRACK AND CORROSION DETECTION.

The pulse-echo UT inspection method used to detect the small cracks in the metallic plates is shown in figure 61. In this UT setup, the sound path travels through the material twice, doubling the sound path and decreasing the sensitivity. The appropriate frequency must be selected to produce enough energy to travel the necessary distance through the part and back to the transducer. To penetrate a 0.25″ thick part (1.0″ of material thickness travel), a 5- or 10-MHz transducer was used. To penetrate the 0.125″ thick part (0.5″ of material thickness travel), a 10-MHz transducer was used. The transducers contained 16 element arrays.

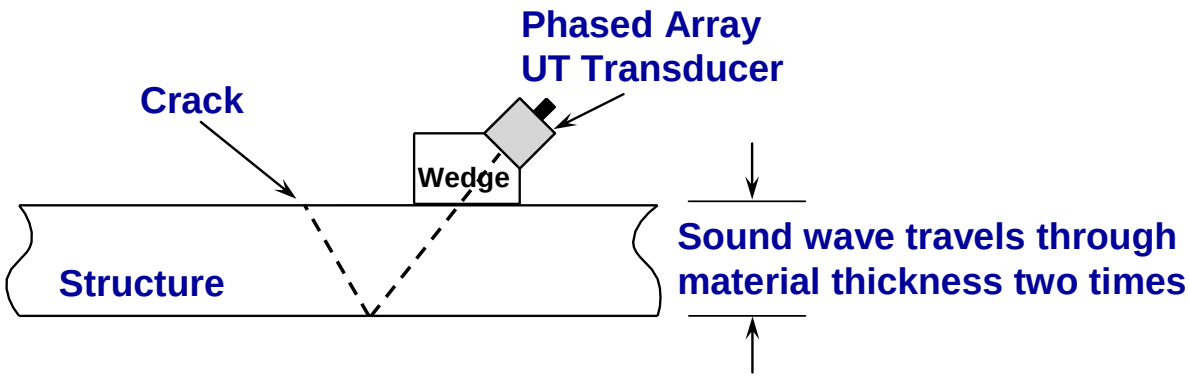


Figure 61. Wave Travel Through the Inspected Part

4.4.1 Phased Array UT Inspection Method.

Phased array UT equipment (Olympus® OmniScan®) was selected for this inspection so a two-dimensional sectoral scan could be produced in real time. Figure 62 shows the phased array device along with the first set of specimens that were used to evaluate this NDI method. The specimens contained crack-like notches in the center of the dogbone region. By using phased array transducers, it was possible to produce real-time, C-scan images in the form of sector views. Figure 63 shows a typical A-scan and sectoral scan data that were produced during the phased array UT inspections of the propeller specimens.

Figure 62. OmniScan UT Inspection Unit and Propeller Crack Test Specimens

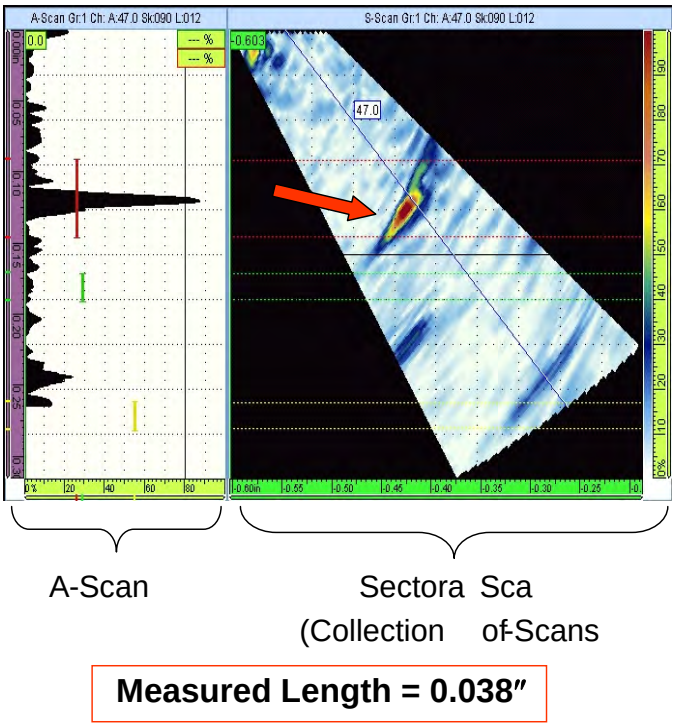


Figure 63. Sample Signal From Phased Array UT Inspection

UT measurements were taken by placing an indexing line, forming a measuring ruler on the monitor, at each end of the crack image, as shown in figures 63 and 64. The dark red color represents the actual crack; lighter colors are simply a ringing effect. Therefore, the rulers were placed at the far ends of the dark red image. Each ruler gives its own location, making the crack length the difference between the two numbers. In the case of the crack imaged in figure 64, the crack length is 0.270″ − 0.237″ = 0.033″.

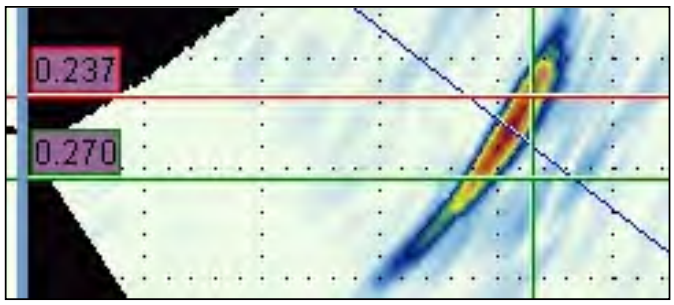


Figure 64. Sample UT Detection of a 0.033″ Length Crack

4.4.2 Dogbone Semicircular Laser Notch/Crack Specimens for Fatigue Property Assessment and NDI Evaluation.

To complete the fracture property assessment described in this report, a number of fatigue dogbone specimens were produced with laser notches that acted as crack initiation sites. Figure 65 shows one of these test specimens. The PD method was used to track the crack growth during fatigue testing of all specimens. During the initial NDI evaluation, some of these specimens were inspected prior to crack runout. Figure 65 compares the results from the PD and phased array UT measurements and shows the sectoral scan, which clearly images the 0.414″ long crack.

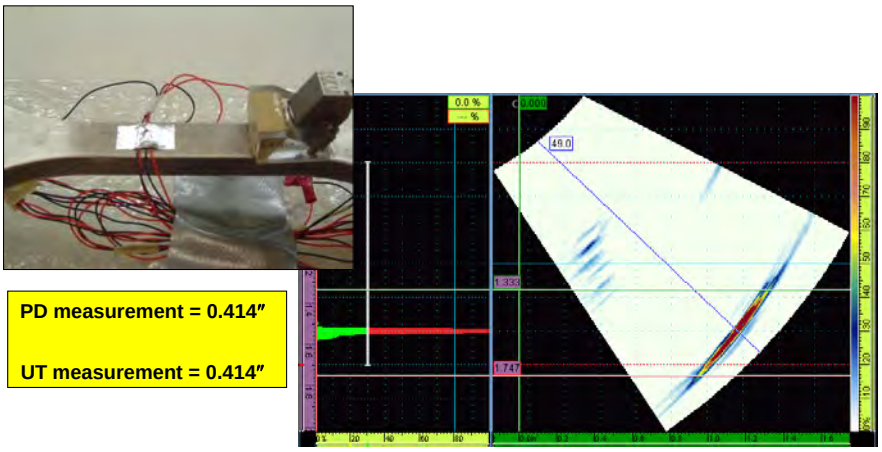


Figure 65. Dogbone Specimen With Center Crack, PD Leads and UT Array Probe, and Sectoral Scan From UT Phased Array Inspection Showing Crack Detection

After obtaining these promising results, a more quantitative evaluation of the overall performance of the phased array, shear wave inspection method was pursued. A series of plates

with small, carefully controlled notch cracks was produced using the process shown in figure 55. None of the cracks were visually evident and all inspections were conducted in a blind fashion where the inspector had no knowledge of the crack profile in the panels. Several calibration cracks were inspected to optimize the use of the sectoral scan images to determine actual crack length. Additional calibration tests determined that a gain of 39 dB provides the best image to assign the crack tips in the sectoral scan. Table 3 summarizes the initial results for crack length prediction using phased array UT and shows refined length predictions following feedback to the inspector that allowed him to better use his image. It is worth noting that the crack length predictions are all within 5% of the actual length.

Table 3. Results for Test Panel 286E Summarizing Crack Detection and Length Estimation

| Blind Inspection—Crack Length Predictions | | | |
|---|---|---|---|
| Indication | No Learning Calibration (in.) | Some Learning Feedback at * (in.) | Actual Crack Lengths (in.) |
| 1 | 0.083 | 0.091 | 0.094 |
| 2 | 0.088 | 0.079* | 0.080 |
| 3 | 0.108 | 0.103 | 0.102 |
| 4 | 0.082 | 0.073* | 0.070 |

*These indicate results that were obtained after the inspector received training by inspecting some cracked panels, and then feedback was provided on the crack flaw profiles.

Figures 66 and 67 show another series of phased array UT images that differentiate cracked from uncracked sites and the ability to determine crack lengths from the sectoral view.

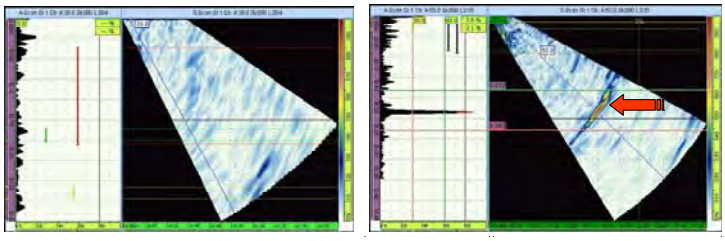

Figure 66. Comparison of Flawed and Unflawed Signals From Phase Array UT Inspection Method

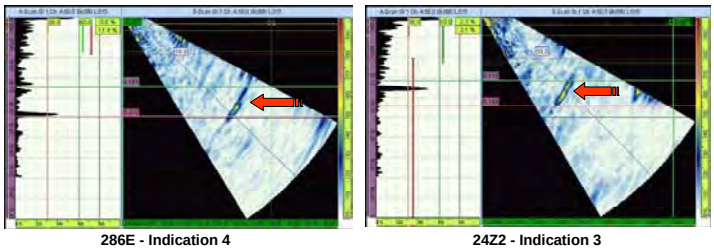


Figure 67. Sample Phase Array UT Indications Demonstrating Crack Length Estimation Using Sectoral Views

Figures 68-71, along with tables 4 and 5, provide the results from the blind flaw detection study. They summarize the ability of phased array UT to detect ultrasmall cracks, determine their exact location, and predict their length. The results for the nine blind test specimens, depicted in figure 68, show that only 2 of the 20 cracks were missed. For the most part, crack length predictions were all within 5% to 10%. In addition, the comparison of predicted crack locations versus actual crack locations revealed that the phased array UT method was able to determine crack locations to within 0.005″ to 0.010″ of accuracy. Figures 70 and 71 compare results for inspections conducted at two different frequencies. For both 10- and 12-MHz inspections, all cracks were found in both specimens with the exception of one of the shorter cracks in specimen 58K9 (figure 71). The predicted crack lengths were quite similar, but the crack length predictions from the 10-MHz inspections were slightly better. Thus, 10 MHz was deemed the optimum frequency for these inspections and was the frequency used for the results cited here.

| Specimen | Hit | Miss | Final Length | Length Predicted |
|---|---|---|---|---|
| 2H10 | X | | 0.051 | 0.046 |
| 374D | X | | 0.037 | 0.025 |
| 55Z2 | X | | 0.116 | 0.122 |
| | X | | 0.021 | 0.027 |
| 58K9 | X | | 0.067 | 0.046 |
| | X | | 0.054 | 0.056 |
| | X | | 0.056 | 0.047 |
| 58M3 | X | | 0.018 | 0.190 |
| | X | | 0.018 | 0.190 |
| 2U58 | X | | 0.078 | 0.086 |
| | X | | 0.110 | 0.113 |
| | X | | 0.089 | 0.090 |
| | X | | 0.067 | 0.070 |
| 40U2 | X | | 0.080 | 0.079 |
| 481S | X | | 0.071 | 0.067 |
| | X | | 0.086 | 0.104 |
| | | X | 0.024 | N/A |
| | X | | 0.104 | 0.101 |
| 4A47 | | X | 0.082 | N/A |
| | X | | 0.034 | 0.046 |

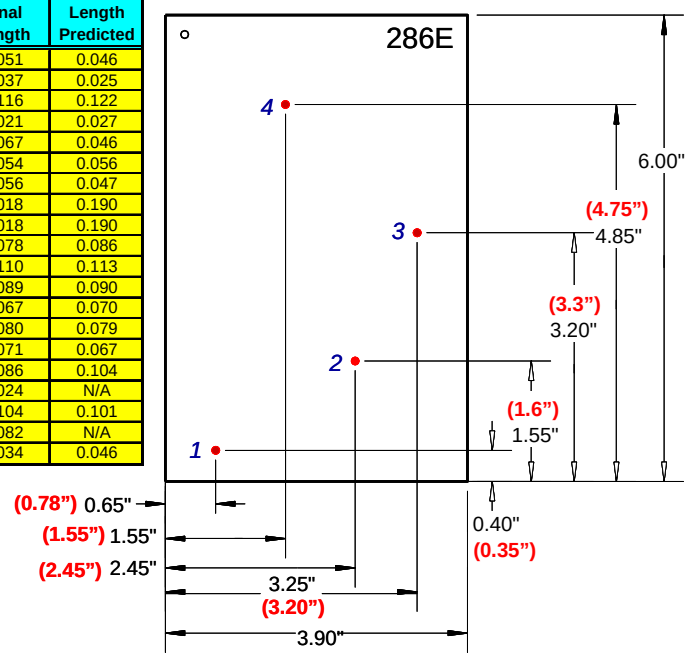


Figure 68. Crack Detection Summary for Sample Panel
(Predicted crack locations in black and actual locations in red.)

Table 4. Results for Test Panel 24Z2 Summarizing Crack Detection and Length Estimation

| Indication | Blind Inspection—Crack Length Predictions (No learning calibration) (in.) | Actual Crack Length (in.) |
|---|---|---|
| 1 | 0.043 | 0.051 |
| 2 | 0.061 | 0.036 |
| 3 | 0.048 | 0.044 |
| 4 | 0.078 | 0.064 and 0.046 (two cracks next to each other) |

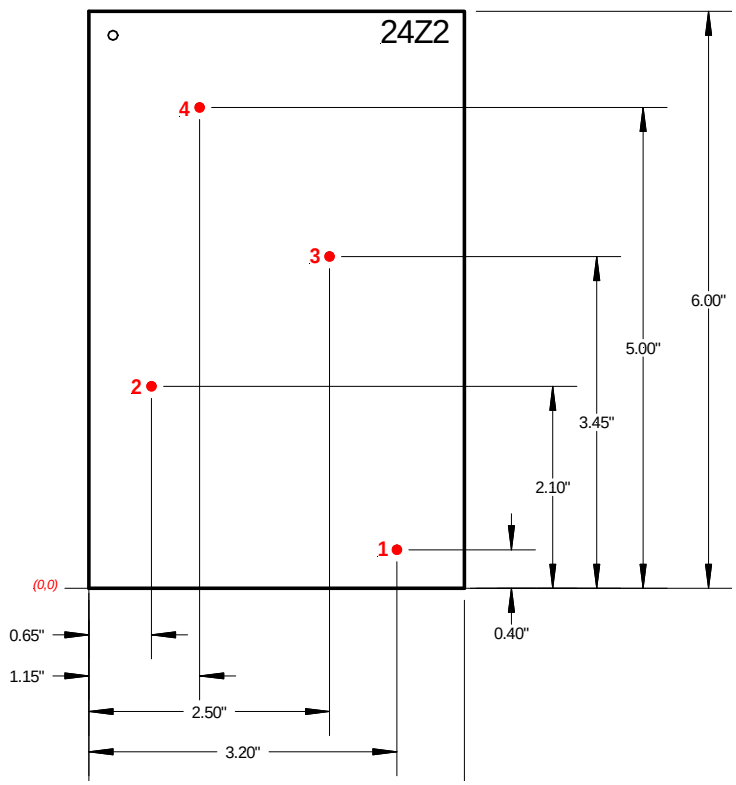


Figure 69. Crack Locations Identified With Phased Array UT Were Correct in Specimen 24Z2

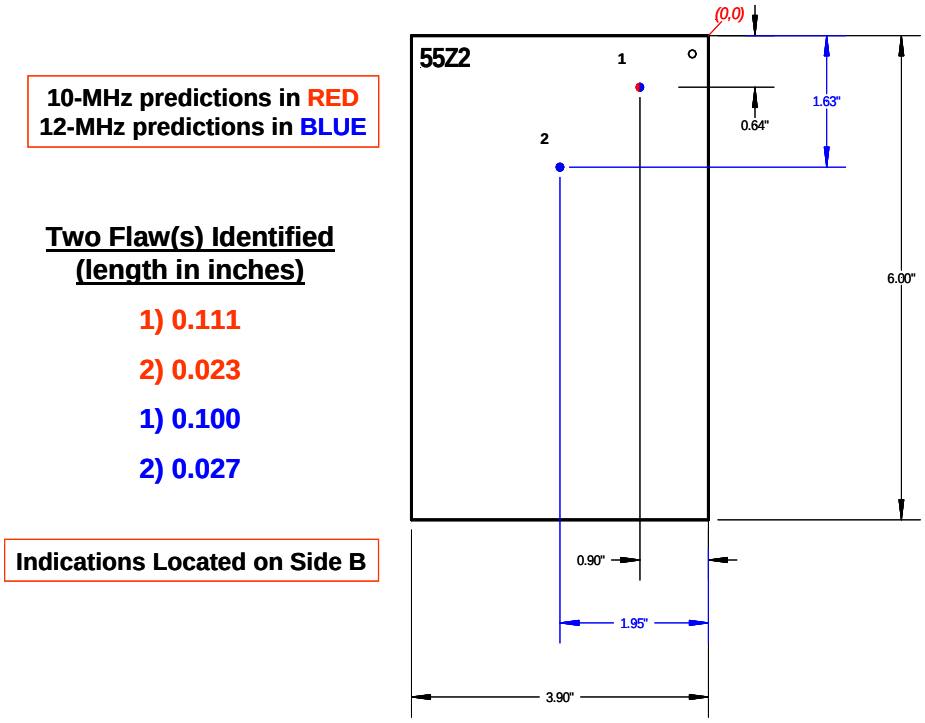


Figure 70. Crack Detection Summary for Blind Flaw Detection Study Using Phased Array UT Method Specimen 55Z2 (Crack detection and length estimated at two inspection frequencies.)

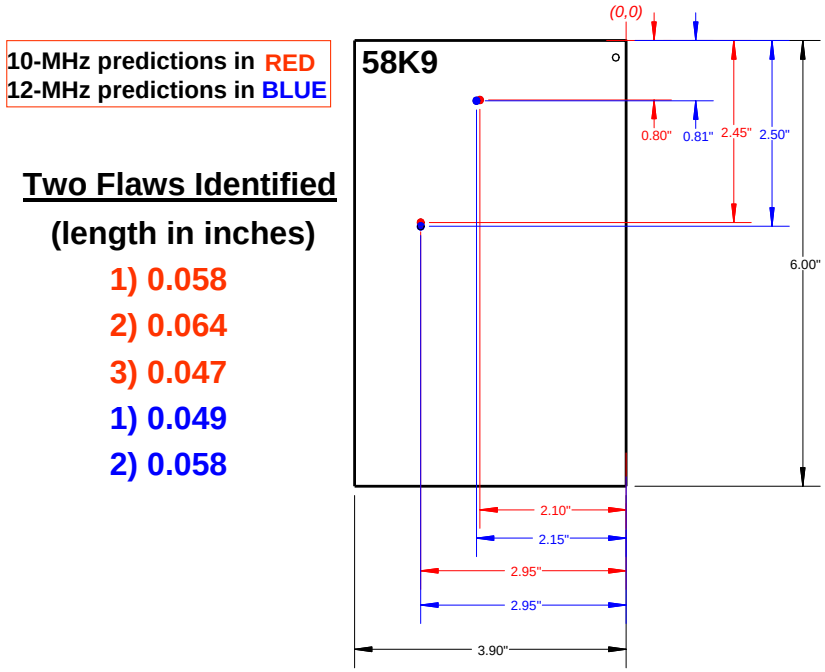


Figure 71. Crack Detection Summary for Blind Flaw Detection Study Using Phased Array UT Method Specimen 58K9 (Crack detection and length estimated at two inspection frequencies.)

Table 5 provides some additional comparisons between actual and predicted crack length and locations produced by the phased array UT inspection method. Once again, the X and Y coordinates for the crack are within approximately 0.005″ of the actual coordinates, while predicted crack lengths are, for the most part, within 5% to 10% of the actual lengths. Table 6 summarizes the overall crack detection results, which were used to produce the estimate for POD. There were only a few misses within all the test specimens, and the only miss in the longer crack regime (>0.050″) was associated with a crack close to a free edge and the associated signal variations that accompany such an edge crack. Additional calibrations for this special case condition should eliminate these missed calls. Overall, 94% of the cracks were detected. Figure 72 shows that this corresponds to a 90% POD level of 0.025″ (with 95% confidence).

Table 5. Sample Phased Array UT Inspection Results Showing Ability to Accurately Locate Cracks

| Exact Location | | | | | Phased Array UT Predictions | | |
|---|---|---|---|---|---|---|---|
| Specimen | Side | X (in.) | Y (in.) | L (in.) | L (in.) | X (in.) | Y (in.) |
| 89H3 | B | 2.12 | 1.00 | 0.033 | 0.037 | 2.15 | 0.90 |
| | | 0.85 | 2.50 | 0.050 | 0.054 | 0.85 | 2.32 |
| | | 2.12 | 3.54 | 0.072 | 0.072 | 2.15 | 3.45 |
| | | 0.85 | 5.20 | 0.082 | 0.076 | 5.12 | 0.85 |
| 03G8 | B | 0.88 | 4.02 | 0.022 | 0.031 | 0.80 | 4.10 |
| | | 2.86 | 5.60 | 0.035 | 0.040 | 2.90 | 5.55 |
| 160D | A | 1.33 | 0.75 | 0.061 | 0.062 | 1.30 | 0.72 |
| | | 2.79 | 1.75 | 0.030 | 0.029 | 2.85 | 1.79 |
| 03D3 | B | 3.25 | 0.92 | 0.101 | 0.103 | 3.30 | 0.97 |
| | | 3.15 | 3.45 | 0.080 | 0.078 | 3.20 | 3.60 |
| | | 1.12 | 5.45 | 0.060 | 0.064 | 1.20 | 5.40 |
| 1P59 | A | 2.78 | 1.00 | N-F | 0.013 | 2.75 | 0.98 |
| | | 3.28 | 2.60 | 0.014 | 0.018 | 3035 | 2.55 |
| | | 0.65 | 3.70 | 0.038 | 0.025 | 0.70 | 3.80 |
| | | 1.90 | 5.20 | 0.075 | 0.080 | 1.80 | 5.30 |

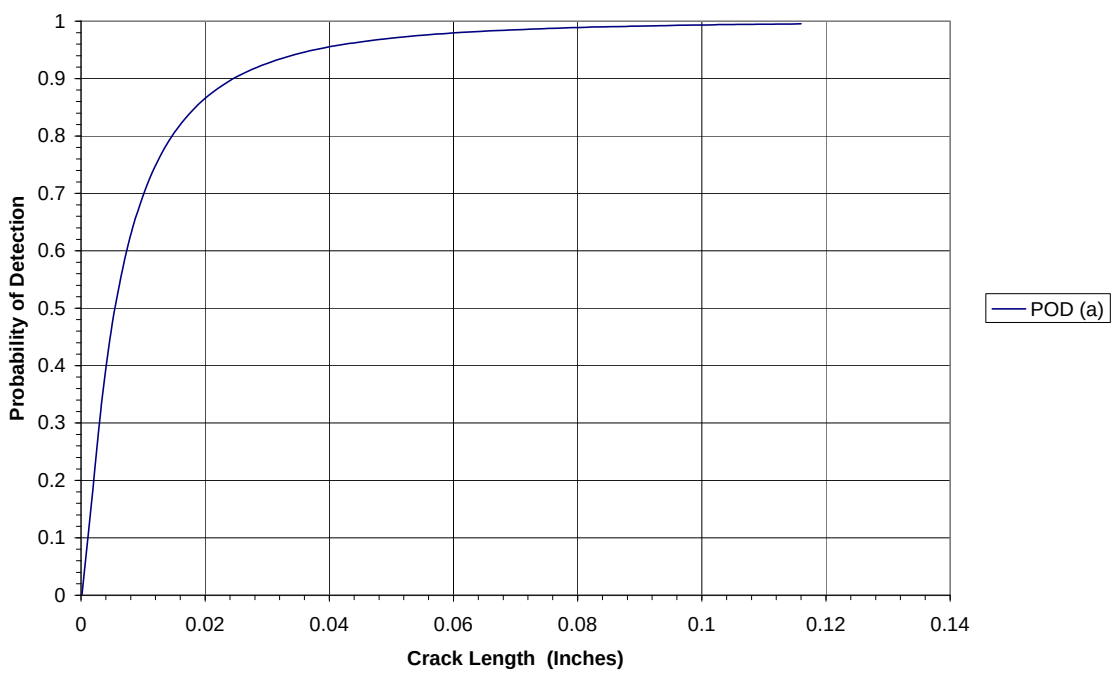


Figure 72. The POD Curve Showing Performance of Phased Array UT for Detection of Small Subsurface Cracks (90% POD occurs at 0.025″.)

Table 6. The POD Inspection Results Summary for Crack Detection and Length Estimation

| Specimen | Hit | Miss | Final Length (in.) | Length Predicted (in.) |
|---|---|---|---|---|
| 2H10 | X | | 0.051 | 0.046 |
| 374D | X | | 0.037 | 0.025 |
| 55Z2 | X | | 0.116 | 0.122 |
| | X | | 0.021 | 0.027 |
| 58K9 | X | | 0.067 | 0.046 |
| | X | | 0.054 | 0.056 |
| | X | | 0.056 | 0.047 |
| 58M3 | X | | 0.018 | 0.019 |
| | X | | 0.018 | 0.019 |
| 2U58 | X | | 0.078 | 0.086 |
| | X | | 0.110 | 0.113 |
| | X | | 0.089 | 0.090 |
| | X | | 0.067 | 0.070 |
| 40U2 | X | | 0.080 | 0.079 |
| 481S | X | | 0.071 | 0.067 |
| | X | | 0.086 | 0.104 |
| | | X | 0.024 | N/A |
| | X | | 0.104 | 0.101 |
| 4A47 | | X | 0.082 | N/A |
| | X | | 0.034 | 0.046 |
| 6912 | X | | 0.068 | 0.069 |
| | X | | 0.033 | 0.025 |
| 6186 | X | | 0.054 | 0.053 |
| 87U7 | X | | 0.027 | 0.025 |
| | X | | 0.033 | 0.033 |
| 883A | X | | 0.073 | 0.073 |
| | X | | 0.114 | 0.111 |
| | X | | 0.058 | 0.046 |
| | X | | 0.082 | 0.08 |
| | | X | 0.042 | N/A |
| 89H3 | X | | 0.033 | 0.037 |
| | X | | 0.050 | 0.054 |
| | X | | 0.072 | 0.072 |
| | X | | 0.082 | 0.076 |
| 03G8 | X | | 0.022 | 0.031 |
| | X | | 0.035 | 0.040 |
| 160D | X | | 0.061 | 0.062 |
| | X | | 0.030 | 0.029 |
| 03D3 | X | | 0.101 | 0.103 |
| | X | | 0.080 | 0.078 |
| | X | | 0.060 | 0.064 |
| 1P59 | X | | 0.012 | 0.013 |
| | X | | 0.014 | 0.018 |
| | X | | 0.038 | 0.025 |
| | X | | 0.075 | 0.080 |

Miss associated with edge effects

4.4.3 Detection of Corrosion Pits Using Phased Array UT.

The crack detection study described in section 4.4.2 quantified the performance of phased array UT inspections to detect and measure ultrasmall cracks in steel and aluminum structures. Laser notches were used to produce the cracks because they were able to properly simulate the profile associated with corrosion pits. Corrosion pits are a primary concern for propeller inspections because the pits act as crack nucleation sites, and the time to grow a crack from nucleation to critical length can be very short due to the rapid accumulation of fatigue cycles in propeller operation. To complete this study into NDI for corrosion pits, specialized test specimens were prepared with controlled, chemically induced corrosion pits. Figure 73 shows the representative geometry for the corrosion pits that should be found with NDI.

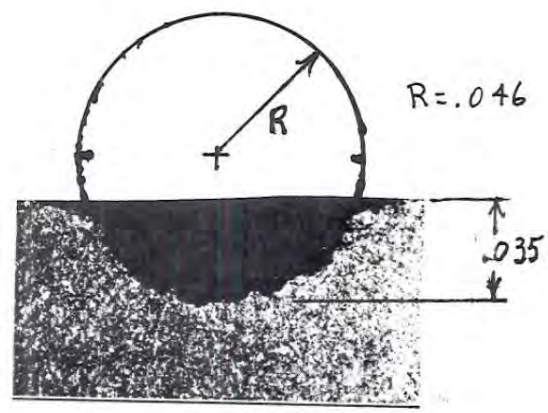


Figure 73. Spherical Geometry of Corrosion Pit in D6AC Material

Figures 74 and 75 show two specimens containing chemically induced corrosion pits. The pit diameter corresponds to the crack length and the pit depth, as shown in figure 73, is always less than the plate thickness. Thus, it is desirable to detect the pits/cracks before they penetrate through the thickness of the plate.

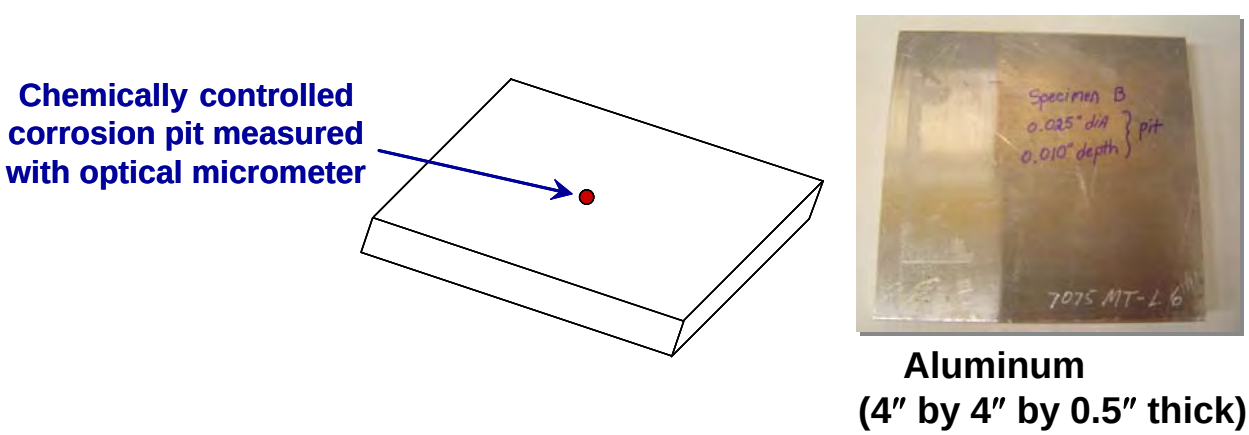


Figure 74. Test Specimen With Center Corrosion Pit

| Specimen | Pit Depth (in.) | Pit Diameter (in.) |
|---|---|---|
| B | 0.010 | 0.025 |
| C | 0.018 | 0.040 |
| D | 0.022 | 0.065 |

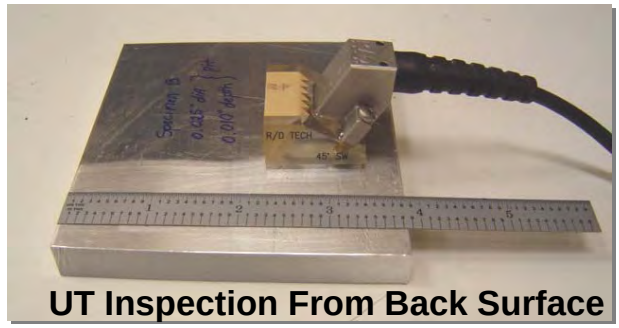


Figure 75. Set of Different Corrosion Pits Produced in the Test Specimens

Figures 76 and 77 show sample results from the phased array UT inspections of the corrosion pit plates. The difference between the reference cursor (red horizontal line) and data cursor (green horizontal line) equals the corrosion diameter. Cursors are placed at each far end of the red indication. All corrosion pits were clearly imaged and the predicted diameters were within 0.002″ of the actual lengths. Note that this indicates a sensitivity to image discontinuities with cross-sectional areas as small as 0.0009 inch$^2$.

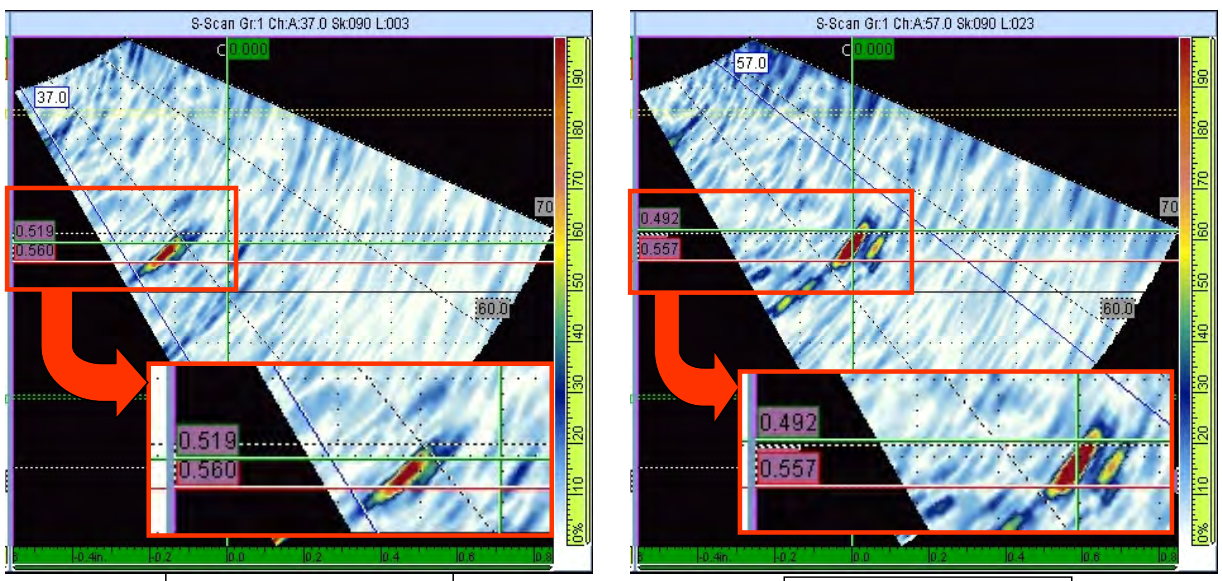


**Specimen C**

**Estimated Corrosion Diameter:**
**(0.560″ − 0.519″) = 0.041″**
**Actual Corrosion Diameter = 0.0405″**

**Specimen D**

**Estimated Corrosion Diameter:**
**(0.557″ − 0.492″) = 0.065″**
**Actual Corrosion Diameter = 0.0653″**

Figure 76. Phased Array UT Sectoral Scan Data Showing Accurate Imaging of Small Corrosion Pits

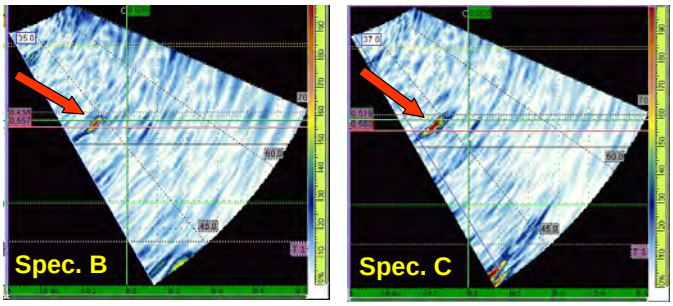


| Specime | Actual Corrosion Data | Estimated Corrosion Diameter (in.) |
|---|---|---|
| B | 0.025 | 0.027 |
| C | 0.040 | 0.041 |
| D | 0.065 | 0.065 |

Figure 77. Phased Array UT Sectoral Scans Showing Typical Signals Used to Detect and Estimate the Size of Corrosion Pits

4.4.4 Small Crack Detection Using EC.

The EC inspection method was deployed to study the performance of this traditional crack detection inspection method. There were two primary concerns related to the application of EC inspections to these ultrasmall cracks. (1) To detect the near-surface cracks of this size, it is necessary to use a high-frequency probe with a very small diameter (~0.10″ diameter), which makes covering large areas difficult. (2) The surface roughness from shot peening creates difficulties for the EC by producing noise in the signals, making interpretation difficult. Probe "liftoff" or other deployment wobbles (irregularities) associated with moving the EC probe over a rough surface, produces noise in the signals or may even produce crack-like signals. As a result, the application of EC is limited to unpeened surfaces, and the results shown here are for smooth, unpeened surfaces. Figure 78 shows the EC device and the two sample signals produced when the EC probe is moved over the crack sites. The large loops are in contrast to flat, horizontal signals, which would be produced by uncracked sites. Figures 79 and 80 show additional EC signals for cracks as small as 0.036″. Signal-to-noise ratios of greater than 3 were obtained for cracks down to 0.064″ in length; however, the signals stemming from cracks less than 0.060″ did not provide strong indications of a crack, and it would be difficult to distinguish these crack signals from the noise associated with uncracked regions. The signals in figures 78 through 80 demonstrate that the EC method can detect these types of cracks in propeller blades, but the POD level would not be as good as the one produced by the phased array UT method.

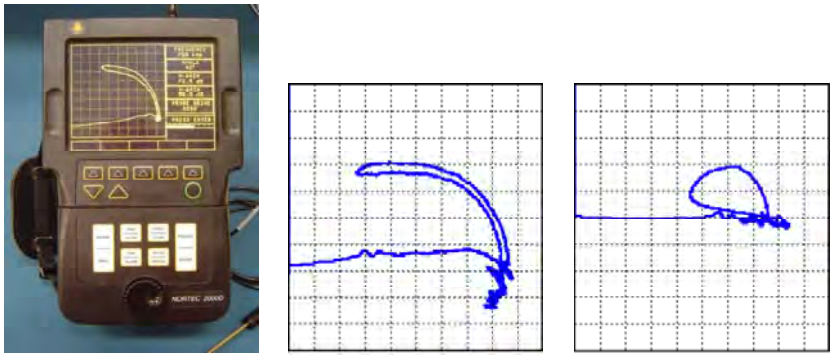

Figure 78. The EC Device and Sample EC Signals Produced by Cracked Sites

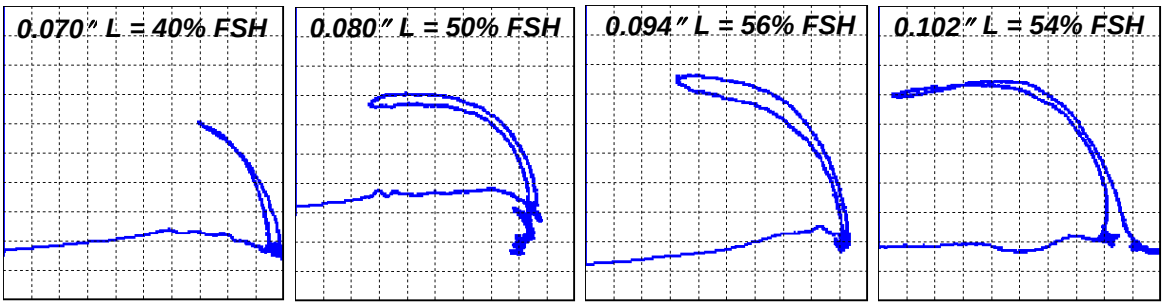


Figure 79. The EC Signals From Four Cracks in Specimen 286E

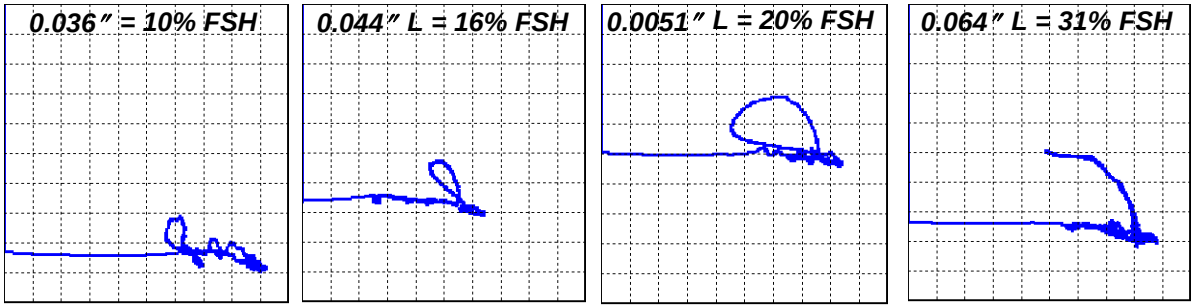


Figure 80. The EC Signals From Four Cracks in Specimen 24Z2

Tables 7 and 8 compare crack length predictions from the EC inspections with the actual crack lengths. It can be observed that the EC predictions are 2 to 3 of the actual crack length. In addition, it was not possible to differentiate closely spaced cracks (see the 4th flaw in table 8); therefore, two adjacent cracks appeared as one long crack. These results also indicate less sensitivity with EC than with the UT method.

Table 7. The EC Results From Panel 286E

| Indication | Blind Inspection—Crack Length Predictions (No learning calibration) (in.) | Actual Crack Lengths (in.) |
|---|---|---|
| 1 | 0.230 | 0.094 |
| 2 | 0.175 | 0.080 |
| 3 | 0.230 | 0.102 |
| 4 | 0.160 | 0.070 |

Table 8. The EC Results From Panel 24Z2

| Indication | Blind Inspection—Crack Length Predictions (No learning calibration) (in.) | Actual Crack Lengths (in.) |
|---|---|---|
| 1 | 0.150 | 0.051 |
| 2 | 0.100 | 0.036 |
| 3 | 0.090 | 0.044 |
| 4 | 0.190 | 0.064 and 0.046 (two cracks next to each other) |

## 4.5 CONCLUSIONS FROM NDI STUDY.

This NDI effort focused on producing inspection methods to reliably detect uniquely shaped cracks, or corrosion pits which act as crack nucleation sites, that are as small as 0.015″ deep by 0.025″ wide. The load spectrum and operating environment for propellers often produce cracks that do not pierce the inspection surface (burrowing cracks). Phased array UT shows sufficient sensitivity to detect these small cracks and corrosion pits before they reach critical size. Realistic test specimens were used to determine that phased array UT has a 90% POD level at 0.025″ without producing false calls. This inspection method works well for both peened and unpeened surfaces. Additional tests to study geometry and edge effects should be conducted to complete the final performance assessment and further refine flaw detection in these regions.

## 5. SUMMARY.

Historically, propeller blades have been designed using a stress-life or S-N approach with an emphasis on the infinite-life regime. This safe-life design approach assumes that a “no cracks” requirement is in place. The propeller blade spectrum loading is established and the key operating condition (1P takeoff at 90% gross weight) is used to size the blade, so that stresses are kept below the modified Goodman diagram for $10^8$ cycles. The design is then checked with the full spectrum stresses using Miner’s Rule to show that cycle-ratio summation is less than 0.5. Equation 1 gives the general form of Miner’s Rule.

$$\sum_i \frac{n_i}{N_i} = D \tag{1}$$

where $n_i$ is the number of cycles at stress level $\sigma_i$, $N_i$ is the number of cycles to failure at stress level $\sigma_i$, and $D$ is the accumulated damage (when $D = 1$, failure occurs).

In the DT design approach, a crack is assumed to exist in the most critical location and orientation. The size of the crack is the length of the crack assumed to be equal to the largest crack that can be reliably found during inspection. The life is determined using a fracture mechanics analysis based on the number of cycles necessary to grow the crack to failure. For the HS propeller CGDT assessment, the key operating condition stresses for the HS Model 568F

blade tulip and hub were kept below the crack propagation threshold for a 0.015-inch-deep surface crack.

The 0.015-inch-deep LGCLF flaws exceeded the depth of cold work in the shot-peened D6AC material (~10 mil), as demonstrated by the residual stress measurements. The LGCLF flaws act like fatigue cracks in D6AC material. HCF $R$ = 0.1 runouts for peened and unpeened D6AC were 43 and 33 ksi, respectively. HCF $R$ = 0.7 runouts for peened and unpeened D6AC were 66 and 58, respectively. Using the runout data, modified Goodman diagrams were generated through fracture mechanics and Kitigawa-El Haddad [12 and 13] equations from NASGRO V5. Resulting curves are lower than existing allowables used to design the propeller hardware. However, debits in fatigue strength for 0.015-inch-deep LGCLF flaws at $R$ = 0.1 were found to be higher than debits for single corrosion pits up to ~0.045-inch deep for peened and unpeened D6AC [7] and higher than trench-like corrosion at 0.011 inch, for unpeened D6AC [8].

As a secondary task, for the material in question (D6AC forging, ultimate tensile strength = 160-180 ksi), a fracture mechanics model was generated based on surface crack testing for threshold and on Royce Forman *da/dN* testing with C(T) specimens [14]. The fracture model also included the shot-peening residual stress profile through the thickness. The fracture model was first verified with constant-amplitude loading and then used to run the life calculation with full-spectrum loads. The design life for the redesigned tulip was determined to be over 100 years.

The redesigned HS Model 568F propeller blade featured an increased outside diameter in the tulip fillet region while retaining the original fillet radius (refer to figure 1). The HS Model 568F blade modification resulted in a weight increase of 0.52 lb per blade, or 3.12 lb for six blades. Because the change in blade weight was due to the increase of tulip wall thickness in the circular section of the blade, there was no change in the twisting moment, as the additional weight was evenly distributed along the blade circumference. Therefore, there was no change in actuator loads resulting from the modified blade design. As a result, the weights of the propeller actuator, oil transfer tube, propeller control module, main pump, and auxiliary pump and motor subassemblies were unchanged. The hub geometry modifications were confined to four regions: the dome hole, between the arms, the ball-loading hole, and the moment axis fillet (figure 2). The redesign of the HS Model 568F hub geometry resulted in a total weight increase of 1.3 lb.

## 6. CONCLUSIONS AND RECOMMENDATIONS.

Using the modified Goodman diagrams for 0.015-inch-deep laser-generated crack-like features (LGCLF) flaw is considered conservative, based on the known corrosion threats to propeller hardware. Shot peening has been demonstrated to be effective in raising the damage tolerance (DT) threshold for these 0.015-inch-deep LGCLF flaws. Using crack growth DT as the basis for propeller structural design is more conservative than existing allowables used to design the propeller components. The increase in weight due to the redesign of the Hamilton Sunstrand (HS) Model 568F hub and blades based on the crack growth damage tolerance allowables was 4.32 lb.

Previous HS studies that involved testing specimens with corrosion pits have shown less of a structural debit than using LGCLF flaws, particularly for unpeened D6AC. It is, therefore, recommended to continue evaluating the effect of corrosion pits on high-strength steels, such as D6AC, 6 and make the data available.

## 7. REFERENCES.


1. Smith, S.L., "Study Proposal for Applying Damage Tolerance to Propeller Systems," internal report Hamilton Sunstrand MM-05-36, 2005-12-21.

2. Forth, S.C., James, M., and Johnston, W., "Development and Validation of Advanced Test Methods to Generate Fatigue Crack Growth and Threshold Data for Use in Damage Tolerance Analyses," FAA report DOT/FAA/AR-04/22, February 2008.

3. Forth, S.C., James, M., Johnston, W., and Newman, J.C., "Anomalous Fatigue Crack Growth Phenomena in High-Strength Steel," *Proceedings International Congress on Fatigue*, Italy, 2007.

4. Forth, S.C., James, M., and Johnston, W., "Fatigue Crack Growth Thresholds in D6AC Steel," *European Conference on Fracture (ECF-15)*, Stockholm, Sweden, 2004.

5. Nardi, A. and Smith, S.L., "Laser Generated Crack-Like Features Developed for Assessment of Fatigue Threshold Behavior," *Journal of ASTM International*, Vol. 5, No. 7, paper ID JAI101557, July 2008.

6. Swin, C., Bakuckas, J.G., and Forman, R., "Characterization of Fatigue Crack Threshold in High-Cycle Fatigue Applications," *Proceedings of the 11th Joint NASA/FAA/DoD Conference on Aging Aircraft*, Austin, Texas, April 2008.

7. Smith, S.L., "Effect of Pitting on Fatigue Strength of D6AC Tulip Steel," internal report Hamilton Sunstrand MM-01-33, 2001-12-14.

8. Smith, S.L., "Additional Specimen Fatigue Tests for D6AC Corrosion," internal report Hamilton Sunstrand MM-02-11, 2002-03-11.

9. Newman, J.C. Jr., "Analyses of Fatigue Crack Growth Databases for use in a Damage Tolerance Approach for Aircraft Propellers and Rotorcraft," FAA report DOT/FAA/AR-07/49, November 2007.

10. Roach, D., Delong, W., and Nguyen, C., "Detection of Micro-Subsurface Defects in Peened Surfaces to Support the Adoption of Damage Tolerance Methods in Propeller Designs," *Air Transport Association Nondestructive Testing Forum*, August 2007.

11. Roach, D. and W. DeLong, "Alternative Methods to Improve the Inspection of Skin-to-Substructure Bond Lines in Main Rotor Blades," *Air Transport Association Nondestructive Testing Forum*, September 2008.

12. Kitigawa, H. and Takahashi, S., "Applicability of Fracture Mechanics to Very Small Cracks or the Cracks in Early Stages," *Proceedings of the Second International Conference on Mechanical Behavior of Materials*, Boston, Massachusetts, August 1976.

13. El Haddad, M.H., Topper, T.H., and Smith, K.N., "Prediction of Non-Propagating Cracks," *Engineering Fracture Mechanics*, 1979.

14. Forman, R., Garcia, D., and Shivakumar V., "NASA JSC Materials Testing & Analysis Activities for NASGRO," June 2, 2009.

APPENDIX A—MATERIAL PROPERTIES USED FOR FRACTURE MECHANICS ANALYSIS

| NASGRO Properties | Surface Crack for D6AC |
|---|---|
| Ultimate tensile strength, UTS | 179 ksi |
| Tensile yield strength, YS | 150 ksi |
| Effective fracture toughness for part-through (surface/corner) crack, $K_{Ie}$ | 112 ksi |
| Plane strain fracture toughness (mode I)m$K_{Ic}$ | 90 ksi |
| Fit parameters, $A_k$ | 0.5 |
| Fit parameters, $B_k$ | 0.25 |
| Crack growth rate constant, $C$ | 6E-9 |
| Exponents in NASGRO, $n$ | 2.5 |
| Exponents in NASGRO, $p$ | 0.5 |
| Exponents in NASGRO, $q$ | 0.5 |
| $DK1$ | 2.65 |
| Fit parameter for threshold, $C_{th}$+ | 1.2 |
| Fit parameter for threshold, $C_{th}$- | 0.1 |
| Alpha | 2.5 |
| Stress relieved, SR | 0.3 |
| Intrinsic crack length, $a_0$ | .001426 |

Note: Values highlighted in blue are from the surface crack tension tests of unpeened D6AC for setting threshold [A-1]. The other values come from (National Aeronautics and Space Administration) testing D6AC [A-2].

REFERENCES.

A-1. Smith, S.L., "Modified Goodman Diagram for D6AC With 15 mil Radius Laser Generated Crack," internal report Hamilton Sunstrand MM-09-19, 2009-4-15.

A-2. Forman, R., Garcia, D., and Shivakumar V., "NASA JSC Materials Testing & Analysis Activities for NASGRO," June 2, 2009.